
**Crossing the Glass Transition During
Volcanic Eruptions: A Matter of Time
Scale and Magma Rheology**

Dominique Richard



München 2015

**Crossing the Glass Transition During
Volcanic Eruptions: A Matter of Time
Scale and Magma Rheology**

Dominique Richard

Dissertation
an der Fakultät für Geowissenschaften
der Ludwig-Maximilians-Universität
München

Vorgelegt von
Dominique Richard
aus Cap-de-la-Madeleine

München, den 26.02.2015

Erstgutachter: Prof. Donald Bruce Dingwell

Zweitgutachter: Prof. James Kelly Russell

Tag der mündlichen Prüfung: 16.07.2015

Table of Contents

| | |
|---|-----|
| Abstract | vii |
| 1. Introduction | 1 |
| 2. Outgassing: Influence on Speed of Magma Fragmentation | 3 |
| 2.1 Introduction | 3 |
| 2.2 Sample Material | 6 |
| 2.3 Methodology | 6 |
| 2.3.1 Apparatus | 6 |
| 2.3.2 Types of Experiments | 11 |
| 2.4 Experimental Results | 12 |
| 2.4.1 Fragmentation Threshold | 12 |
| 2.4.2 Permeability | 13 |
| 2.4.3 Fragmentation Speed | 16 |
| 2.4.4 Outgassing during Fragmentation Events | 20 |
| 2.4.5 Effect of Outgassing on Fragmentation Speed | 21 |
| 2.5 Implications for the Fragmentation Process | 23 |
| 2.5.1 Outgassing – Speeding Up or Slowing Down Fragmentation? | 23 |
| 2.5.2 Gas Flow Dynamics Considerations | 26 |
| 2.5.3 Fragmentation of Altered Dome Material | 29 |
| 2.6 Concluding Remarks | 30 |
| 3. The Emplacement and Cooling of a Peralkaline Spatter-Fed Rheomorphic Deposit from Pantelleria | 31 |
| 3.1 Introduction | 31 |
| 3.2 Background | 33 |
| 3.2.1 Glass | 33 |
| 3.2.2 Glass Transition | 33 |
| 3.2.3 Structural Relaxation | 34 |
| 3.2.4 Enthalpy Relaxation Geospeedometry | 38 |
| 3.3 Methodology | 40 |
| 3.3.1 Sample Characterization | 40 |
| 3.3.2 Geospeedometry | 41 |
| 3.3.3 Accuracy Testing on DGG Standard Glass | 42 |
| 3.3.4 Thermal Annealing Experiments | 42 |
| 3.3.5 Measuring Natural Glasses from Pantelleria | 43 |
| 3.4 Geological Setting | 43 |
| 3.5 The Tramontana Spatter-Fed Rheomorphic Deposit | 45 |
| 3.6 Results | 49 |
| 3.6.1 Groundmass Glass and Bulk Composition | 49 |
| 3.6.2 Mineral Phases and Textures | 49 |

| | | |
|-------|--|-----|
| 3.6.3 | Sample Appearance and Composition before and after DSC Measurements..... | 56 |
| 3.6.4 | Accuracy of Cooling Rate Estimates..... | 57 |
| 3.6.5 | Influence of Thermal Annealing on Cooling Rate Estimates..... | 58 |
| 3.6.6 | Calorimetry of Pantellerites | 59 |
| 3.6.7 | Modeling Parameters and Cooling Rates | 63 |
| 3.7 | Discussion..... | 66 |
| 3.7.1 | Range of Peak Glass Transition Temperatures..... | 66 |
| 3.7.2 | Interpreting the Cooling Rate Profiles | 68 |
| 3.7.3 | Emplacement of the Tramontana Spatter-Fed Rheomorphic Flow | 68 |
| 4. | The Nature and Emplacement of a Phonolitic Glassy Volcaniclastic Deposit within the Guajara Formation, Tenerife..... | 73 |
| 4.1 | Introduction | 73 |
| 4.2 | Terminology | 75 |
| 4.3 | Geological Setting | 75 |
| 4.4 | Sampling Site and Material | 77 |
| 4.5 | Methodology..... | 82 |
| 4.5.1 | Sample Characterization..... | 82 |
| 4.5.2 | Geospeedometry | 83 |
| 4.6 | Results | 83 |
| 4.6.1 | Microscopic Textures | 83 |
| 4.6.2 | Composition..... | 86 |
| 4.6.3 | Heat Capacity Curves | 87 |
| 4.6.4 | Modeling Parameters and Cooling Rates of Phonolites..... | 89 |
| 4.7 | Discussion | 93 |
| 4.7.1 | Significance of Multiple Heat Capacity Peaks | 93 |
| 4.7.2 | Main Components of the Deposit..... | 95 |
| 4.7.3 | Emplacement..... | 96 |
| 5. | Outlook..... | 98 |
| | Bibliography | 101 |
| | Acknowledgements | 110 |

Abstract

Predicting the occurrence and the evolving nature of volcanic eruptions remains an outstanding challenge. The complexity of volcanic systems requires the use of many different approaches to gain a more profound understanding of the interplay of parameters such as magma temperature, composition, volatile content, cooling rate and viscosity as they interactively control the rheology of magma. This study focusses on three different scenarios in which the glass transition, a kinetic boundary distinguishing between solid-like and liquid-like behavior of melt in response to applied stresses, is crossed. (1) Bubbly magma fragments due to rapid decompression. The yield strength of the magma is overcome and the magma behaves in a brittle manner. Here, the influence of permeable gas flow, inside porous and permeable rocks, on the speed at which magma fragmentation occurs was investigated experimentally. (2) Spatter from a lava fountain agglutinates and coalesces upon landing. A spatter-fed flow forms, progressively thickens and lengthens, and results in a complex accumulation of glassy layers mingled with scoria, which grades into a lava-like section at the front of the flow. Because it is likely that individual layers forming the spatter-fed flow remain in the glass transition interval for extended periods of time, the effect of thermal annealing on glasses was tested. Conditions conducive to thermal annealing during emplacement are discussed. (3) A pyroclastic deposit is emplaced in a hot and viscous state via fall or flow processes and consists of devitrified material and obsidian. The eruptive scenario is unclear; here the cooling history as well as microscopic and macroscopic textures help constraining the nature of the deposit's components and identify the last few processes by which this deposit was emplaced.

Permeable flow of volatiles through the porous and permeable network of a bubbly magma may influence the speed of magma fragmentation. Experiments were performed to reproduce the fragmentation of magma using a shock tube apparatus at room temperature and natural pyroclastic material with a connected porosity ranging from 15% to 78%. For each sample series, the initial pressure required to initiate magma fragmentation was determined. Furthermore, sample permeability was measured and the samples were classified into: (a) dome/conduit wall rocks and (b) pumice/scoria. Results confirm that substantial outgassing during fragmentation leads to higher fragmentation thresholds. In addition, experimental fragmentation speeds are unexpectedly significantly higher than the modeled fragmentation speeds for high-permeability dome/conduit wall rocks, but lower for high-permeability pumices. Low-porosity, low-permeability, altered dome/conduit wall rocks fragment at significantly higher speeds than expected. Because fragmentation threshold and fragmentation

speed are among the determining parameters for the initiation, sustainment and cessation of an eruption, outgassing should be considered in the modeling of magma fragmentation dynamics.

The spatter-fed rheomorphic deposit from Cala di Tramontana, on the island of Pantelleria, Sicily, resulted from the mildly explosive eruption of pantelleritic magma as a lava fountain. This peralkaline rhyolitic magma has exceptionally low viscosities due to its high alkali, halogen and iron contents. Microscopic textural, geochemical and thermal analyses have helped setting better constraints on the cooling history and emplacement of this ca. 7 m thick deposit. Peak glass transition temperatures from the glassy layers are very low and range from 512 to 571 °C for a heating rate of 10 K min⁻¹. Cooling rate estimates are obtained from the modeling of heat capacity curves using the enthalpy relaxation geospeedometry method, which follows the Tool-Narayanaswamy-Moynihan (TNM) method. Cooling rates range from 10⁻¹ to ca. 10⁻⁷ K min⁻¹ and are dispersed inconsistently throughout the flow deposit. For the first time, the effect of thermal annealing on cooling rate estimates has been tested. Thermal annealing experiments on remelted pantelleritic glasses from the same flow reveal that cooling rate estimates can be reduced by up to 3 log units when the investigated glasses are maintained at 450 °C for 1 day prior to the modeling with the TNM method. The individual layers most likely remained at temperatures high enough to cause thermal annealing by which additional relaxation of the glasses could occur. Results support an emplacement model in which several hot-melt layers were emplaced gradually in a complex aggradation process and provided heat to underlying layers to allow for thermal annealing within the glass transition interval. Caution is necessary when interpreting cooling rate estimates.

The phonolitic glassy base of a sequence of pyroclastic deposits from the top of the Guajara Formation along the Las Cañadas caldera, Tenerife, in the Canary Islands, exhibits unusual textures that sparked our interest. The ca. 3 m thick volcanic deposit is mostly composed of obsidian with light-green material dispersed in the obsidian. A cooling rate profile from the base up to about the middle of the deposit suggests higher cooling rates at the base (10⁻³ K s⁻¹) than in the middle of the deposit (10⁻⁶ K s⁻¹). The textural analyses reveal that the green phase is composed of welded and devitrified ash and geochemical data indicate that the major element composition of the obsidian and the green phase is identical within the accuracy of the measurements. An additional convincing piece of evidence consists of fragments of the green phase that detached and moved a short distance from their probable original location. Based on this analysis, it is likely that a pyroclastic flow was emplaced, followed by partial devitrification during cooling as the melt, now obsidian, was still viscous.

À mes trois rayons de soleil Mathilda, Kilian et Béatrice,
et mon adoré Michael, pour leur amour et soutien inconditionnels.

“Do what you feel in your heart to be right – for you’ll be criticized anyway.”

Eleanor Roosevelt

“Whatever your mind can conceive and believe it can achieve.”

Napoleon Hill

1

Introduction

Volcanic eruptions represent one of the greatest natural hazards on Earth. Predicting eruptions and evaluating their associated hazard is a great challenge. However, we do know that some volcanoes tend to erupt more quietly and produce lava flows, while others tend to erupt more violently and produce devastating pyroclastic density currents. An infamous example is the catastrophic explosive volcanic eruption of Mont Pelée, in the Caribbean Islands, during which a nuée ardente destroyed the village of Saint-Pierre and caused over 30 000 casualties in 1902. There are of course many advantages to living in the proximity of volcanoes, such as fertile soils and tourism, which partly explain high population densities near volcanoes. Eruption forecasting and the elaboration of probable eruption scenarios with their associated pyroclastic fall or flow deposits for any given volcano are crucial to hazard mitigation in the proximity of volcanoes, but these tasks can only be reliably achieved if eruptive and flow processes are well understood.

Peralkaline volcanic centers, such as Teide, in the Canary Islands, and Pantelleria, in Italy, have been recognized for the eruption of particularly low-viscosity magmas, with a high-silica and

high-halogen content relative to their calc-alkaline homologues. Eruptive styles associated with peralkaline volcanism are not well understood and therefore, it can be a great challenge to determine the conditions that led to the formation of the peralkaline deposits that we observe today. Volcanoes occurring at convergent plate boundaries, such as Krakatau, Indonesia and Colima, Mexico, are associated with highly explosive volcanic eruptions of more calc-alkaline compositions. A better understanding of the processes that occur inside the volcanic conduit could help explaining, for example, the magnitude and frequency of such eruptions.

All magmas contain volatile phases, when still deep inside the Earth's crust. As magma moves closer to the Earth's surface, gases exsolve from the melt, seep through magma and rock, and emanate at the surface of the Earth. However, some gases remain dissolved in the melt, which makes its way toward the Earth's surface. Once in a volcanic conduit, pressure decreases greatly and volatiles may start to exsolve, forming bubbles. If magma is sufficiently viscous, gases will stay trapped. These bubbles may grow and even coalesce, forming a permeable network. The crossing of the glass transition and the resulting fragmentation of this porous and permeable magma will occur if a threshold pressure is reached, or if the deformation rate of the magma is sufficiently high. Chapter 2 focuses on the fragmentation of porous permeable magma as a function of pressure applied to the magma. If magma degassing occurs, such that the amount of dissolved volatiles is too low to produce efficient magma fragmentation, magma erupts effusively. However, we could argue that most volcanic eruptions occur due to the presence of exsolved volatiles in the melt. If degassing of the magma is complete and volatiles have left the volcanic system altogether even before magma has reached the surface, magma will likely not erupt, unless it comes in contact with external water, which is outside the scope of this study. In Chapter 3, the effect of thermal annealing on cooling rate estimates is for the first time investigated experimentally. Thermal annealing affected the unique cooling history of a peralkaline rhyolitic spatter-fed rheomorphic deposit and the complexity in the emplacement of spatter-fed flows is demonstrated. In chapter 4, the glassy, partly green and devitrified, base of a sequence of pyroclastic welded deposits is investigated. The nature of a green phase dispersed in obsidian is elucidated and leads to very intriguing emplacement questions. Macroscopic and microscopic textures and the cooling history of the obsidian offer new important clues to attempt to identify the processes that led to final deposition and challenge the prior interpretation of this deposit being a fallout deposit.

The study presented in Chapter 2 has been published in a scientific peer-reviewed journal:

Richard, D., Scheu, B., Mueller, S. P., Spieler, O., and Dingwell, D. B., 2013, Outgassing: Influence on speed of magma fragmentation: *Journal of Geophysical Research-Solid Earth*, v. 118, no. 3, p. 862-877.

2

Outgassing: Influence on Speed of Magma Fragmentation

2.1 Introduction

The fragmentation of highly viscous bubbly magma lies at the heart of explosive eruption dynamics because it is the ultimate process by which magma breaks up into fragments to form a gas-pyroclast mixture from a volcanic conduit or lava dome. Therefore, parameters controlling fragmentation also control transitions between effusive and explosive eruption regimes. The brittle failure of magma may occur due to (1) the rapid decompression of a bubbly magma by dome collapse or landslide and the overcoming of the tensile strength of the melt (Dingwell, 1996); (2) high magma acceleration in the volcanic conduit causing an increase in

strain rate (Papale, 1999); (3) the vesiculation of magma until a critical bubble-to-melt volume ratio is reached, followed by a disruption causing bubbles to burst (Sparks, 1978); or, (4) the contact of magma with external water producing phreatomagmatic eruptions. In order to better understand the fragmentation process triggered by sudden decompression events, shock tube experiments have been performed on natural porous volcanic rocks (e.g., (Alidibirov and Dingwell, 1996b; Scheu et al., 2008; Scheu et al., 2006; Spieler et al., 2004b).

The term “fragmentation” refers commonly to *magma* fragmentation, the magma being a three-phase medium consisting of melt, crystals, and volatiles, with a given porosity and permeability. As mentioned above, there are several processes proposed for magma fragmentation, but our study focuses on the fragmentation of highly viscous bubbly magma by rapid decompression where bubble nucleation and growth are not considered (Dingwell, 1996). This fragmentation process occurs so rapidly that the magma behaves in a brittle way, just as a solid (Alidibirov, 1994). Ichihara and Rubin (2010) have explored magma brittleness in detail and their study suggests that for the short time scales of our experiments, highly viscous magma ($\geq 10^9$ Pa s) would behave in a brittle manner. Therefore, it is relevant to investigate controlling parameters for this type of magma fragmentation process such as fragmentation speed and permeability, using volcanic rocks at room temperature (Mueller et al., 2005; Mueller et al., 2008; Scheu et al., 2008; Scheu et al., 2006).

In the fragmentation of highly viscous bubbly magma, the initial pressure (P) required to initiate and sustain fragmentation (*fragmentation threshold*) is mainly controlled by the fractional connected porosity (Φ). This initial pressure corresponds to the pressure of the compressed gas inside the bubbles contained in the magma. The energy stored in the compressed gas per unit volume of magma for initial pressures much greater than atmospheric pressure represents the main energy source for the fragmentation process, and is expressed by Alidibirov (1994) as:

$$E \approx \frac{P\Phi}{\gamma - 1} \quad (1)$$

where γ is the specific heat capacity ratio for magma and gas (Woods, 1995). We use $\gamma=1.67$ because we assume a “reversible” adiabatic fragmentation process, meaning that there is no heat transfer between the pyroclasts and the expanding gas. Therefore a state of thermal disequilibrium prevails. In other words, we assume that the fragmentation process is isentropic (no change in entropy). The time scale for gas expansion as the fragmentation front passes is very short relative to the heat transfer time scale between pyroclast and gas (Koyaguchi et al., 2008), which justifies the assumption of isentropic conditions. Based on Equation 1, high-porosity magma requires a lower initial pressure to fragment because more energy is available for fragmentation.

Fragmentation criteria have been defined empirically (Spieler et al., 2004b) and theoretically (Alidibirov and Dingwell, 1996b; Fowler et al., 2010; Koyaguchi et al., 2008; McBirney and Murase, 1970; Spieler et al., 2004b; Zhang, 1999). Mueller et al. (2008) found an empirical relationship relating permeability, a measure of how easily a fluid can flow through porous media, to the energy required to fragment dome rocks and explosive activity products at threshold overpressures. The fragmentation process itself is thought to consist of bubbles bursting layer by layer before bubble expansion can occur (Alidibirov and Dingwell, 1996b; Alidibirov and Dingwell, 2000; McBirney and Murase, 1970; Scheu et al., 2006). In addition, initial pressure and connected porosity have been shown experimentally to be the main controlling parameters on the speed at which the fragmentation surface propagates through highly viscous bubbly magma (dubbed the *fragmentation speed*) (Scheu et al., 2006; Spieler et al., 2004a).

Spieler et al. (2004b) postulated, however, that high permeability resulted in higher fragmentation thresholds, based on experimental results on Campi Flegrei samples of 82 % and 85 % connected porosity. Mueller et al. (2005) have shown that permeability is highly variable even within rocks of similar porosity and suggested that, above a critical permeability value (k) of 10^{-12} m^2 , the fragmentation threshold of magma is higher. Numerical models have considered the effect of gas loss to volcanic conduit walls (e.g., Jaupart and Allègre, 1991; Melnik and Sparks, 2005; Woods and Koyaguchi, 1994), but these models account for permeability only as a parameter conducive to effusive volcanism. Burgisser and Gardner (2004) have investigated experimentally and empirically the role of magma ascent rate, bubble growth and coalescence in the transition between explosive and effusive eruptive regimes, where escape of gas from the magma prevents fragmentation. Klug and Cashman (1996) and Rust and Cashman (2011) have discussed in detail the development of permeability, its effect on the conditions leading to magma fragmentation, and the resulting pyroclast size distribution, but, as in Burgisser and Gardner (2004), not the effect of permeability on the actual fragmentation process for fragmentation threshold or speed.

In this study, we revisit the influence of permeable gas flow on the fragmentation threshold, but focus our interest on the influence of permeable gas flow on fragmentation speed. We refer to permeable gas flow/gas loss observed within the timescale of magma fragmentation as *outgassing*. We expect that outgassing due to high permeability hinders the buildup of overpressure in highly viscous bubbly magma during rapid decompression and reduces the energy available for fragmentation. The overpressure is the pressure difference between the pressure in the gas phase and the pressure in the solid phase or magma once decompression begins (Fowler et al., 2010). We perform shock tube experiments on natural volcanic rock samples of dome/conduit wall rocks and pumice/scoria over a wide range of connected porosity and permeability and detect significant outgassing of samples. The model of Koyaguchi et al. (2008) is used to calculate fragmentation speeds in order to compare with our experimental fragmentation speeds and investigate the effect of outgassing on magma fragmentation speed.

2.2 Sample Material

Pumice, scoria and mostly blocks from pre-existing lava domes or possibly volcanic conduit walls were collected in volcanoclastic deposits from Lipari, Aeolian Islands, Italy and from volcanoes along the Ring of Fire: Colima, Mexico; Augustine, Alaska, USA; Bezymianny, Russia; Krakatau and Kelut, Java, Indonesia (Table 2.1). Field samples were large enough to drill at least 5 cylinders that were 60 mm high and of 25 mm diameter. The connected porosity of the cylindrical samples was measured with a Helium Pycnometer (Accupyc 1330, Micromeritics) and spans a wide range from 15 to 78% (Table 2.1). We will refer to each sample set by the name of the sample set and we sometimes add the sample's average connected porosity for clarity. The samples collected were as fresh as possible, with little to no alteration and a groundmass containing glass (Figure 2.1). Groundmass compositions range from rhyolite through basaltic andesite. Colima-C6 is one exception where the sample had a slightly reddish tint and its groundmass consisted of feldspar microlites, oxides and < 1% glass. Plagioclase phenocrysts had altered rims and amphibole phenocrysts showed corona textures. It is also worth noting that this sample contained fine-grained enclaves up to 1 cm in size. Colima-D2 and Bezymianny-D2 show pronounced tortuous elongated voids, possibly as a result of shear within a dome or conduit wall.

The experimental cylinders were usually drilled in the elongation direction of the fabric formed by vesicles, crystals and/or compositional banding. However, for Colima-C6 and Krakatau-D4, the cylinders were drilled perpendicular to the observed fabric due to the shape of the samples. Bezymianny-C3 I and Bezymianny-C3 II were drilled from the same block, but the former sample set was drilled perpendicular to the fabric, and the latter, parallel to the fabric. The orientation of the drilled samples relative to the rock fabric can have an effect on the permeability of the samples during experiments due to permeability anisotropy.

2.3 Methodology

2.3.1 Apparatus

A shock-tube apparatus is used to perform fragmentation experiments by rapid decompression at room temperature and pressures up to 30 MPa (Figure 2.2) (Alidibirov and Dingwell, 1996a, b; Scheu et al., 2006; Spieler et al., 2004a; Spieler et al., 2004b). The experimental setup consists of a steel autoclave fixed to the bottom of a tank (height=3 m, diameter=0.4 m), the latter of which operates at atmospheric conditions. The sample cylinders are glued with Crystal Bond glue into a steel sample holder and tightly inserted in the autoclave. The autoclave and the tank are separated by a series of copper or aluminum diaphragms that rupture for specific

Table 2.1 Description of the samples collected: provenance, bulk and glass composition, average connected porosity, isolated porosity, formation factor, electrical tortuosity and permeability. ¹ values result from measurements performed by R. Leonhardt. ² values from Muller et al (2008). *k* values from this study were calculated based on pressure decay curves recorded during permeable gas flow experiments at low applied pressures between 1.5 and 4 MPa, without gas volume below the sample.

| Volcano | Sample provenance | Bulk and glass composition | Average connected porosity (fraction void space Φ) | Isolated porosity | Formation factor (F) ¹ | Electrical tortuosity ¹ (F Φ) [Φ] | Permeability ¹ (m ²) | Permeability ² (m ²) [Φ] |
|-----------------------------|--|---|--|-------------------|-----------------------------------|---|---|---|
| Colima, Mexico | 1999 block-and-ash flow deposits in San Antonio valley | andesitic, <<1% visible glass | 0.156 | 0 | - | - | - | 1.51e-13 [0.1427] |
| | | andesitic, rhyolitic groundmass | 0.230 | 0.1 | 24.70 | 4.1 [0.16489] | 5.2636e-12 | 2.21e-12 [0.1896] 9.56e-13 [0.1825] 2.38e-12 [0.2164] |
| | 1913 lahar in Cordoban valley | andecitic | 0.625 (P3) | 1.5 | - | - | - | 8.54e-12 [0.6469] |
| | | | 0.625 (P4) | 2.6 | - | - | - | 1.36e-12 [0.6212] |
| Augustine, Aleutian Islands | 1986 pyroclastic flow deposit | andesitic, rhyolitic groundmass | 0.480 | 6.2 | - | - | - | 1.93e-12 [0.4768] |
| Bezymianny, Kamchatka | 1956 pyroclastic flow deposit from directed blast | andesitic, rhyolitic groundmass | 0.382 | 3.5 | 25.35 (I) | 8.5[0.33534] | 8.29961e-13 | 2.88e-13 [0.3804] |
| | | | 0.387 | 3.5 | 24.80 (II) | 8.4[0.33807] | 1.25788e-12 | 6.15e-13 [0.3852] |
| | 2000 block-and-ash flow deposit | andesitic, rhyolitic groundmass | 0.456 | 0.05 | 5.40 | 2.2[0.40067] | >9.86923e-12 | 9.24e-12 [0.4542] |
| Anak Krakatau, Indonesia | 1999 pyroclastic deposit from Strombolian eruption | basaltic-andesite, andesitic groundmass | 0.447 | 0 | - | - | - | 6.57e-14 [0.4145] |
| Kelut, Indonesia | 1990 pyroclastic flow deposit from subplinian eruption | basaltic-andesite, dacitic groundmass | 0.562 | - | - | - | - | - |
| Lipari, Aeolian Islands | Pumice from 500-600 AD Monte Pilato eruption | rhyolitic, rhyolitic groundmass | 0.762 | 3.6 | - | - | - | 4.85e-13 [0.7582] 5.21e-13 [0.7659] |

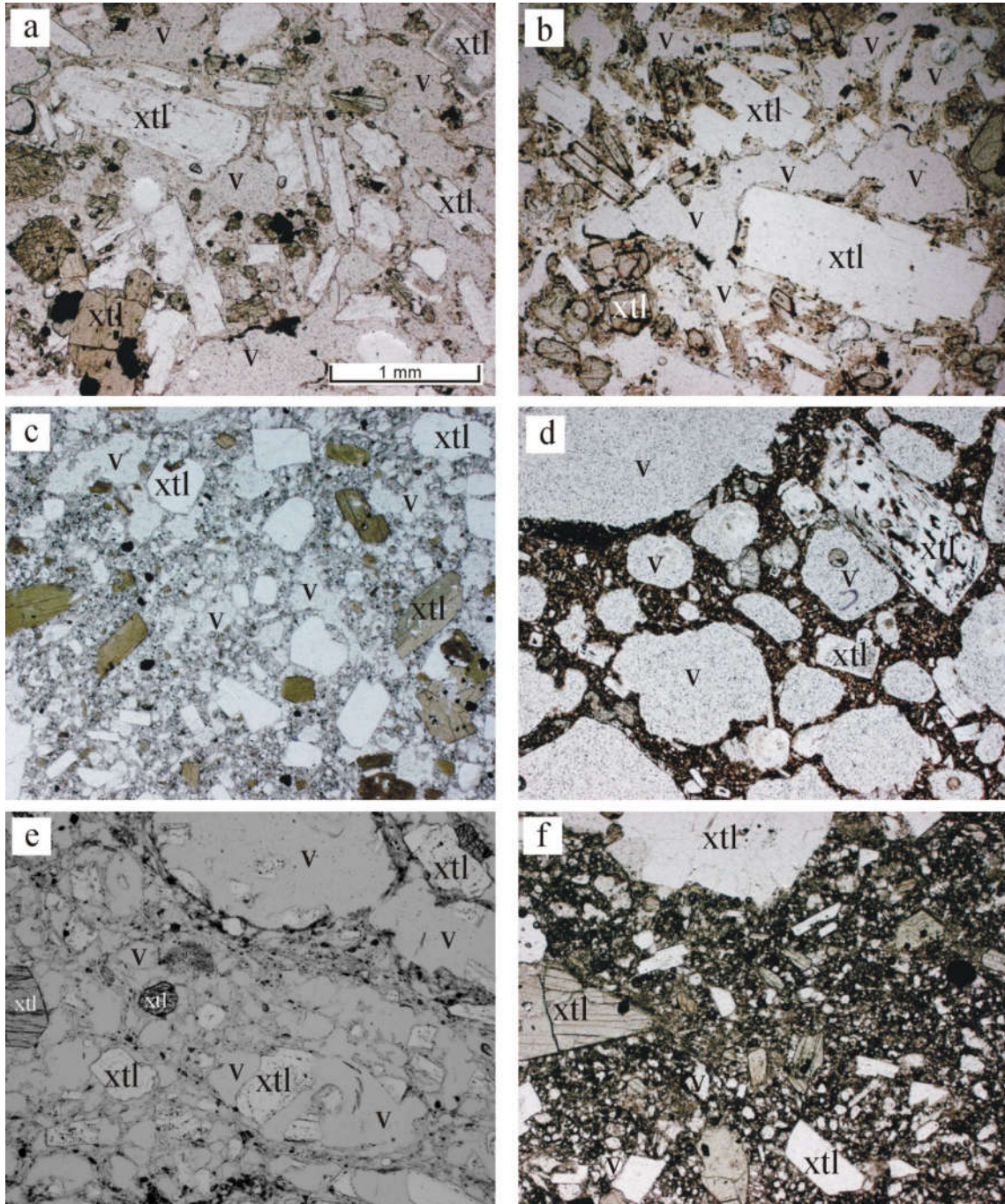


Figure 2.1 Thin section pictures in plane light and 2.5x magnification (a) Bezymianny-D2 (45.6%), (b) Colima-D2 (23.0%), (c) Bezymianny-C3 (38.2% and 38.7%), (d) Krakatau-D4 (44.7%), (e) Kelut-C15 (56.2%), (f) Augustine-P1 (48.0%), (g) Colima-P3 (62.5%), (h) Colima-P4 (62.5%), (i) Lipari-F (76.2%), (j) Colima-C6 (15.6%). The Kelut-C15 (56.2%) thin section picture was converted to a grey-scale picture because the original picture had a yellowish-green tone due to its impregnation for fluorescence microscopy.

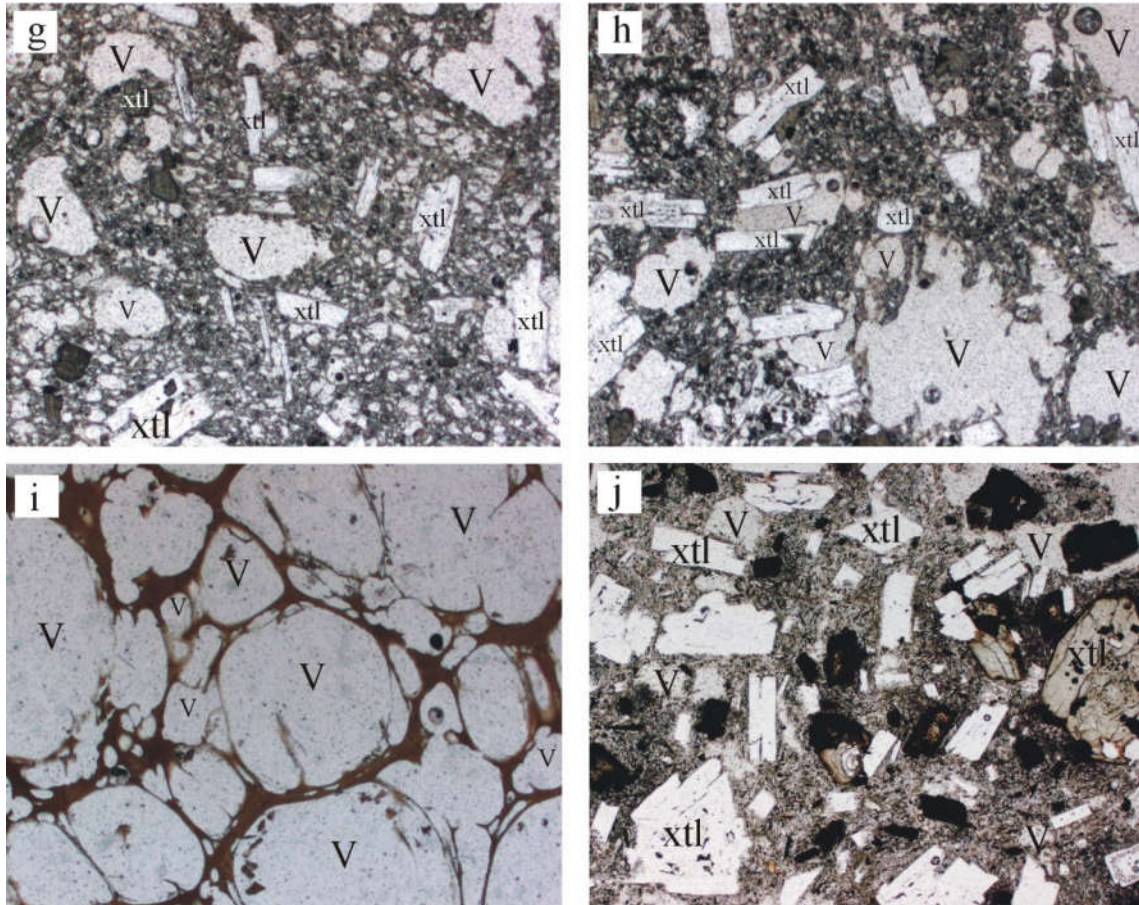


Figure 2.1 (continued)

initial pressures. The autoclave is slowly pressurized with argon gas to the desired initial pressure; in this study, the maximum initial pressure is 30 MPa. Following the sudden rupture of the diaphragms, a shock wave propagates into the air of the large tank, the argon gas expands up into the large tank, the autoclave decompresses rapidly, and a rarefaction wave is generated. A fragmentation front (or surface), defined as the boundary between the intact porous rock and the gas-pyroclast mixture, travels down the sample cylinder for $P > P_{th}$. As long as the overpressure, defined as the pressure difference between the pressure in the gas phase and the pressure in the solid phase, is higher than the tensile strength of the solid phase, fragmentation continues. Two dynamic pressure transducers track the pressure release at the top and at the bottom of the sample cylinder. The sudden pressure drop at the top of the sample cylinder is considered as the start of the fragmentation process for $P > P_{th}$, and the sudden pressure drop at the bottom of the sample cylinder, as the end of the fragmentation process. The very short delay between the start of decompression of the autoclave and the start of fragmentation is neglected. We are also aware that, once the fragmentation front has reached the bottom of the sample cylinder, the fragmentation process may continue as intra-block fragmentation of individual fragments can occur as long as the fragments are in a decompressive regime (McGuinness et al., 2012).

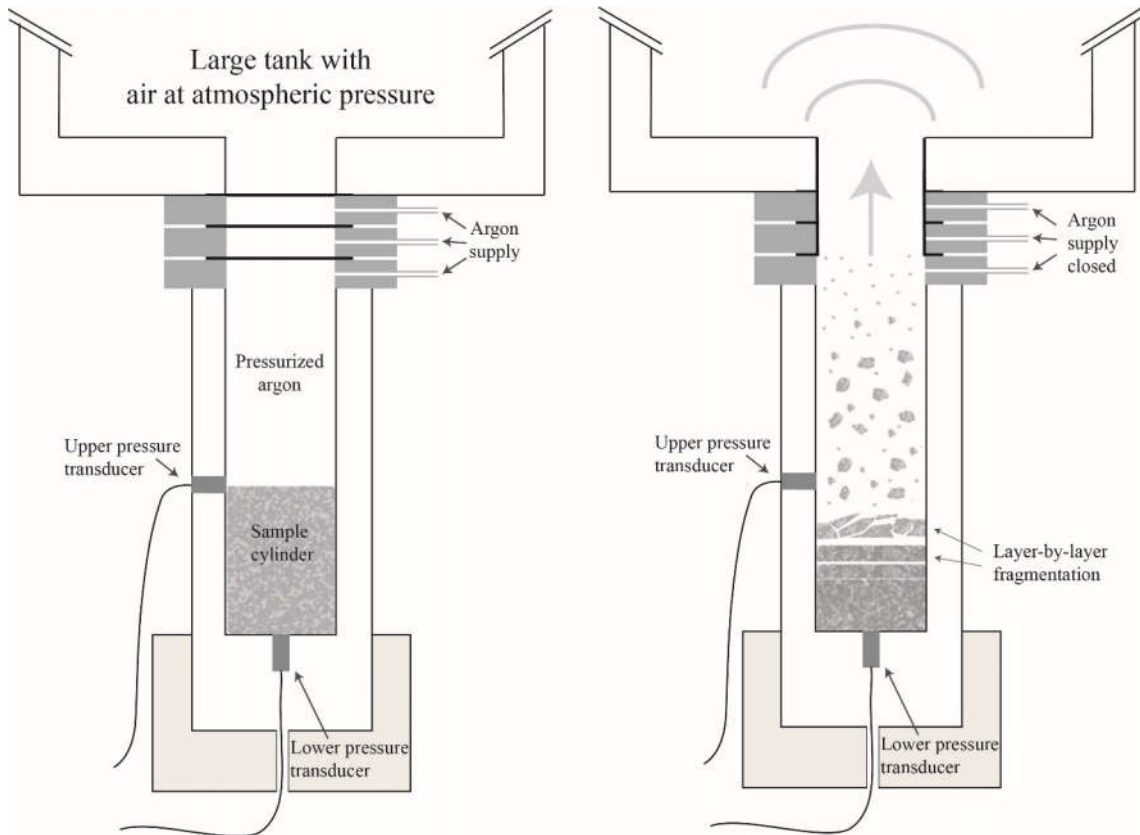


Figure 2.2 Simplified schematic diagram of the setup used for the permeability, fragmentation threshold and fragmentation speed experiments. (a) State of the setup before each experiment as the autoclave and sample cylinder of porous rock get pressurized. A system of 2 to 3 diaphragms in the top part of the autoclave allows a controlled step-by-step pressurization in order to closely achieve the desired initial pressure. (b) A sudden increase in pressure in the chamber between the top 2 diaphragms results in the quasi-simultaneous rupture of all diaphragms. A shock wave propagates into the air in the large tank and a rarefaction wave travels down the porous rock, resulting in the decompression of the autoclave. If $P < P_{th}$, gas filtrates through the sample cylinder without any fragmentation, and if $P \geq P_{th}$, a layer-by-layer fragmentation occurs and the rock fragments get ejected out of the autoclave into the large tank. The 2 pressure transducers track the pressure evolution at the top and bottom of the sample cylinder during an experiment.

2.3.2 Types of Experiments

The shock tube apparatus allows us to (1) determine the fragmentation threshold of each sample set, (2) estimate permeability for most sample cylinders used in fragmentation experiments, and (3) measure the fragmentation speed for initial pressures greater than the fragmentation threshold. All experiments are performed at room temperature.

First, a series of experiments is performed for each sample set in order to obtain a fragmentation threshold. The fragmentation threshold was previously defined as the initial pressure at which a sample completely fragments (Spieler et al., 2004b) and was set to a fragmentation speed value of 0 m/s. However, it is possible to calculate a fragmentation speed when the sample completely fragments, not to mention that the fragmentation threshold is likely to be at a pressure value slightly lower than the pressure at which a sample completely fragmented during an experiment. For this reason, we follow the modified fragmentation threshold definition used in Scheu et al. (2006) and Alatorre-Ibargüengoitia et al. (2011). The fragmentation threshold is a pressure range that includes both fragmentation initiation and complete fragmentation. The initiation of fragmentation represents the breaking away of the top few millimeters of the sample cylinder and the complete fragmentation means that the whole sample cylinder fragments, indicating that the initial pressure was sufficient to sustain the fragmentation process. Partial fragmentation occurs when the fragmentation process cannot be sustained for the whole length of the sample cylinder, and part of the sample cylinder remains intact and glued inside the sample holder. For each sample set, we average the initial pressure where fragmentation initiation is observed and the initial pressure at which complete fragmentation occurs. Threshold values for a given sample set are averaged.

Before each fragmentation experiment, we estimate permeability by measuring the pressure decay at the top and bottom of sample cylinders for initial pressures of 2 MPa for samples with >40% connected porosity, and 4 MPa for samples with <40% connected porosity. We use the same experimental apparatus for permeability measurements as for fragmentation experiments. Therefore, we ensure highest reliability of the data as each sample remains glued in the same sample holder for all measurements and experiments performed on any given sample. In our measurements, a steady (or quasi-steady) state of the gas flow cannot be achieved due the absence of a compressed gas volume below the sample cylinder in the fragmentation apparatus. For this reason, we use a modified version of the original code (Mueller et al., 2005) that accounts for the shorter time scale of our experiments and the fact that a steady gas flow through our samples cannot be achieved. The code includes a modified non-linear correction coefficient. Each permeability measurement results in two pressure decay curves that are subsequently modeled with this modified code. Our permeability values are similar to the values from Mueller et al. (2005), again attesting to the reliability of our method.

Multiple experiments with initial pressures up to 30 MPa produce a fragmentation speed profile for each sample set to demonstrate the relationship between initial pressure, connected porosity, fragmentation threshold and speed of fragmentation. The number of experiments for each sample set is limited by the number of sample cylinders available. The fragmentation speed is calculated by dividing the cylinder length by the time interval, representing the time between the pressure drop of upper and lower pressure transducers. Estimating the permeability of all sample cylinders before speed experiments has not been done in previous studies. This simple permeability test allows us to interpret our results with respect to permeability.

2.4 Experimental Results

2.4.1 Fragmentation Threshold

Most fragmentation thresholds from this study (Figure 2.3, Table 2.2) fit well the trend from previously measured data at room temperature (Mueller et al., 2008; Scheu et al., 2006). The fragmentation threshold relation was calculated based on the fragmentation threshold criterion of Koyaguchi et al. (2008) for the no-bubble-expansion case. The model is based on the Griffith theory for crack propagation through elastic media and involves the propagation of a crack from the inner bubble wall to the outer bubble wall, considering the tensile strength of the solid phase and tangential stress at the outer bubble wall. The criterion is defined as:

$$P_{th} = \frac{2S(1-\Phi)}{3\Phi\sqrt{\left(\Phi^{-1/3}-1\right)}} \quad (2)$$

S is the effective tensile strength (Table 2.3) and was obtained from the least-squares analysis of the best fit for the above relationship between fragmentation threshold and connected porosity (Koyaguchi et al., 2008). Their analysis used data from room temperature experiments on samples from Mt. Unzen, Japan (Scheu et al., 2006) and Soufrière Hills, Montserrat (Kennedy et al., 2005; Scheu, 2005). Colima-D2, Bezymianny-D2 and Colima-P3 plot significantly above the trend, whereas the rest of the data follows the trend more closely. Note that the threshold value for Lipari-F was determined by Mueller et al. (2008). Based on data from this study (Table 2.2), fragmentation initiation occurs at initial pressures between 5 and 10% below P_{th} , but even up to ca. 35% below P_{th} for dome/conduit wall rocks with $k \geq 10^{-11}$ m². Moreover, the spread in fragmentation threshold values is wide for Colima-D2 and Bezymianny-D2 in comparison to the other sample series: up to 4.2 MPa above and 2.3 MPa below the average fragmentation threshold.

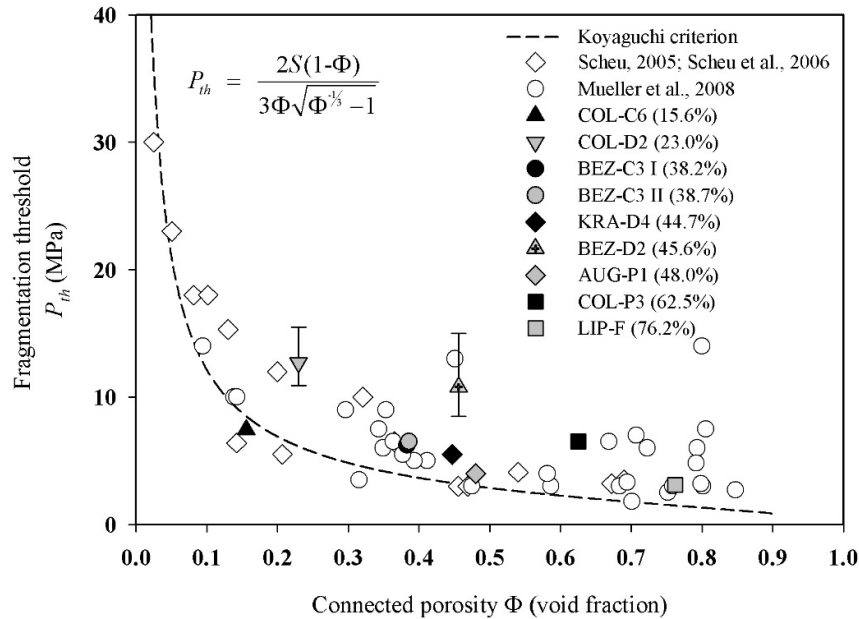


Figure 2.3 Fragmentation thresholds derived from experiments at room temperature plotted along with the Koyaguchi fragmentation criterion (Koyaguchi et al., 2008). Each sample set from this study is represented by a symbol in black or grey.

2.4.2 Permeability

Our permeability data (Figure 2.4) are plotted along with data from Mueller et al. (2005) on a graph differentiating effusive (dome/conduit wall rocks) from explosive (pumice/scoria) activity products. Our data fall within these two classification fields, which justifies the separation of our data into two subsets: (1) dome/conduit wall rocks and (2) pumice/scoria. The Colima-D2 k -value is an average of 4 k -values, representing a subgroup of the 12 fragmented sample cylinders. Colima-D2 k -values are estimated for 8 of the 12 fragmented sample cylinders because, although a permeability test had not been performed prior to these fragmentation experiments, we consider these experiments worth including in our study. We find justified to attribute a minimum k -value of 10^{-12} m^2 to these cylinders based on the fact that the k -values for the other 4 fragmented sample cylinders as well as for 3 additional sample cylinders (Table 2.1) are all above 10^{-12} m^2 .

Table 2.2 Fragmentation threshold values for all sample series investigated for their fragmentation speed. The threshold values for Colima-P4 and Kelut-R5 are missing due to the small number of sample cylinders. However, because Colima-P4 has a high permeability, and the same origin and connected porosity as Colima-P3, its threshold value should lie close to Colima-P3's threshold value. + and – represent the wide spread in threshold values for the two high-*k* dome/conduit wall rocks sample series. An uncertainty of 0.5 MPa is comprised within the symbols of Figure 2.3. The average % represents the pressure range in which fragmentation initiation (P_{FI}) occurs relative to the fragmentation threshold. Calculations were made for each threshold experiment and all % were then averaged for one sample series.

| Sample series | Φ (void fraction) | P_{th} (MPa) | + | – | Average $(P_{th}-P_{FI})/P_{th}$ % |
|------------------|---------------------------|-------------------|-----|-----|--|
| Colima C6 | 0.156 | 7.5 | | | 6 |
| Colima D2 | 0.230 | 12.7 | 2.8 | 1.8 | 5 |
| Bezymianny C3 I | 0.382 | 6.3 | | | 8 |
| Bezymianny C3 II | 0.387 | 6.5 | | | 8 |
| Krakatau D4 | 0.447 | 5.3 | | | 10 |
| Bezymianny D2 | 0.456 | 10.8 | 4.2 | 2.3 | 34 |
| Augustine P1 | 0.480 | 4.0 | | | 7 |
| Kelut C15 | 0.562 | >3.0 | | | x |
| Colima P3 | 0.625 | 6.5 | | | 7 |
| Colima P4 | 0.625 | x | | | x |
| Lipari F | 0.762 | 3.0 | | | 5 |

Table 2.3 Parameters used in the calculations of fragmentation speeds based on the Koyaguchi et al. (2008) model.

| Parameter | Value |
|--|---------------------|
| Density of solid phase (kg m^{-3}) | 2500 |
| Temperature (K) | 300 |
| Specific gas constant ($\text{J kg}^{-1} \text{K}^{-1}$) | 208 |
| Ratio specific heats for gas phase | 5/3 |
| Effective tensile strength (Pa) | 2.180×10^6 |

Permeability measurements had previously been performed on 1 to 3 samples per sample set by Mueller et al. (2008) (Table 2.1). These experiments were done using a shock-tube-like apparatus, where a volume of compressed gas below the pressurized sample flowed through

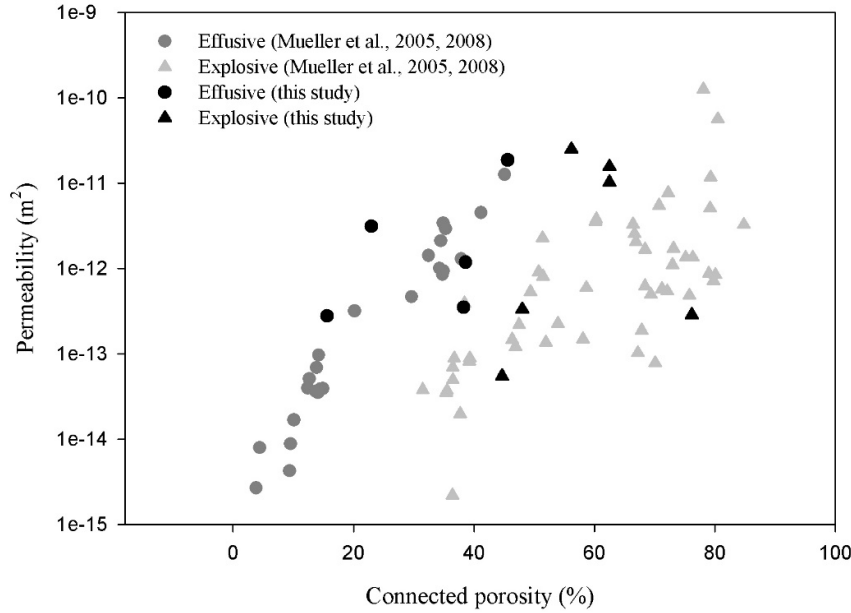


Figure 2.4 Permeability data from this study (black symbols) plot well within the two fields defined by data from dome/conduit wall rocks and pumice/scoria (Mueller et al., 2005 and 2008).

the sample when decompression occurred, as described by Mueller et al. (2008). The permeability values obtained in our study are consistent with permeability values obtained by Mueller et al. (2008), except for Augustine-P1, where our values are consistently about one order of magnitude lower, possibly due to some degree of heterogeneity in the sample. Permeability values are again verified by measurements performed on the exact same samples as Muller et al. (2008), with a similar setup except for the shorter autoclave and absence of a gas volume below the sample. In addition, permeability measurements performed by R. Leonhardt, now at the Conrad Observatory in Vienna, on 5 of our samples with a steady-state permeameter confirm our permeability values.

In an attempt to explain the scatter in fragmentation thresholds (Figure 2.3), we plot, as in Mueller et al. (2008), the fragmentation threshold energy density (E_{th}) as a function of permeability (Figure 2.5). The power law best fit from Mueller et al. (2008) as well as the E_{th} values were adjusted by a factor of $(\gamma-1)^{-1}$ to account for the assumption of adiabatic conditions instead of isothermal conditions. We use equation (1) to define the fragmentation threshold energy density:

$$E_{th} \approx \frac{P_{th} \Phi}{\gamma - 1} \quad (3)$$

$\gamma=1.67$ because our experiments are performed using Argon gas and we assume adiabatic conditions. Kelut-C15 is omitted from the graph because the sample cylinder was only partially fragmented during the threshold experiment at 3 MPa. The threshold experiment could not be repeated due to the limited number of cylinders. Indeed, the scatter from Figure 2.3 is significantly reduced (Figure 2.5) and our results support the conclusion from Mueller et al. (2008) that the fragmentation initiation of high permeability rocks requires more energy (E_{th}) than that of low-permeability rocks (Figure 2.5). Consequently, this means that, for a given connected porosity, the fragmentation threshold (P_{th}) of high-permeability rocks is increased (Equation 3) relative to that of low-permeability rocks. The fragmentation thresholds of Colima-D2, Bezymianny-D2 and Colima-P3 attest to this observation (Figure 2.3).

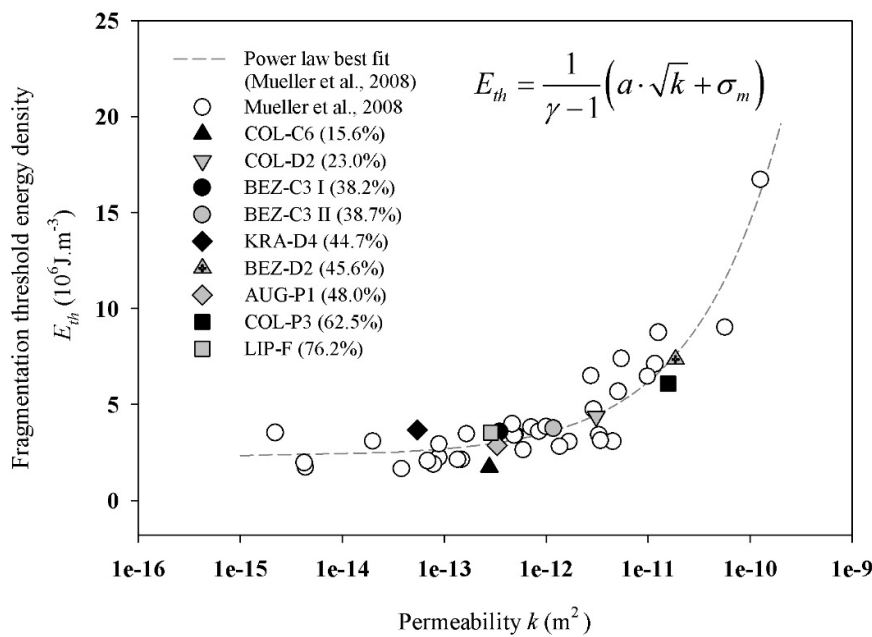


Figure 2.5 Fragmentation threshold energy density plotted as a function of permeability. The power law best fit equation from Mueller et al. (2008) was adjusted by a factor of $(\gamma-1)^{-1}$ to account for adiabatic conditions instead of isothermal conditions during the fragmentation process. The scatter of the fragmentation thresholds plotted in Figure 2.3 is significantly reduced.

2.4.3 Fragmentation Speed

Three representative fragmentation speed profiles are illustrated on Figure 2.6 in order to give the reader a sense of how initial pressure and connected porosity affect the fragmentation speed. Profiles demonstrate the non-linear, logarithmic relation between initial pressure and fragmentation speed (Scheu et al., 2006). Experimental fragmentation speeds are calculated for experiments where the pressure decay curves clearly indicate a sharp decrease of the initial

pressure at the bottom of the sample (Figure 2.7). We compare our experimental fragmentation speeds (X) with fragmentation speeds computed using the model by Koyaguchi et al. (2008). The fragmentation criterion appropriate for $P \geq P_{th}$ is defined as:

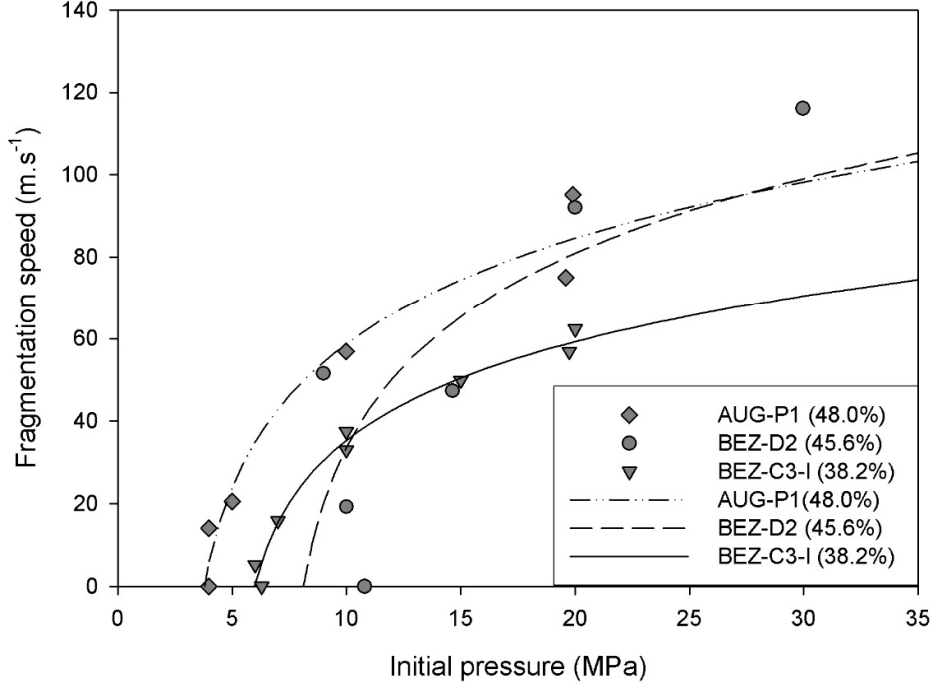


Figure 2.6 Fragmentation speed profiles for 3 sample sets. Speed increases with higher connected porosity and higher initial pressure, but the relationship is non-linear. Note how the Bezymianny-D2 trend crosses the other trends.

$$\frac{3\Delta p_f}{2(1-\Phi)} - P - \frac{\Delta p_f}{2} = \frac{S}{\sqrt{\Phi^{-1/3} - 1}} \quad (4)$$

where Δp_f is the gas overpressure in the sample at the fragmentation front and P is the initial pressure. Equation 3 is the simplified form of Equation 4 because at the fragmentation threshold for the no-bubble-expansion case, $\Delta p_f = P_g = P_{th}$, where P_g is the gas pressure. Further, a relationship between overpressure and fragmentation speed, modified from Koyaguchi and Mitani (2005a), was derived for the adiabatic no-bubble-expansion case (Koyaguchi et al., 2008). The relationship assumes (Koyaguchi and Mitani, 2005b; Koyaguchi et al., 2008) (a) the fragmentation front travels at a constant speed, (b) the fragmentation front is a discontinuous boundary between bubbly magma and gas-pyroclast mixture across which mass, momentum and energy are conserved, (c) the dynamics of the gas-pyroclast mixture follow the shock tube

theory for inviscid fluid, (d) gas expansion occurs under isentropic conditions. This relationship is defined as:

$$\frac{\Delta_{Pf}}{P} = 1 - (\gamma + 1) \left(\frac{U}{a} \right)^{2\gamma/\gamma+1} + \gamma \left(\frac{U}{a} \right)^2 \quad (5)$$

We combined Equations 4 and 5 in order to obtain the calculated fragmentation speeds (U). γ is the ratio of specific heats for the gas phase. a is the sound speed in the gas-pyroclast mixture and is defined as $a = P_g \sqrt{\gamma} / \rho \sqrt{n R_g T}$ where P_g is the gas pressure, equal to the initial pressure P in the no-bubble-expansion case, ρ is the density of the gas-pyroclast mixture, n is the gas mass fraction, R_g is the gas constant and T is the gas temperature. For the details of the conservation laws across the fragmentation front, we refer to Koyaguchi and Mitani (2005b). The fragmentation criterion was developed and tested using fragmentation threshold and fragmentation speed data obtained from experiments performed in the same conditions as experiments from the present study.

Our calculations consider the parameters of each experiment, such as connected porosity, cylinder length, cylinder radius and initial pressure, and a few other constant parameters (Table 2.3), as to produce the most realistic fragmentation speed values possible. The complete set of experimental fragmentation speed data from this study is plotted against the calculated, or “expected”, fragmentation speeds (Figure 2.8). Although a large part of the data fits the model, several experimental fragmentation speeds lie significantly below and above calculated fragmentation speeds. This scatter confirms our suspicion that fragmentation speed does not only depend on initial pressure and connected porosity, and opens the door to other potential parameters, such as outgassing.

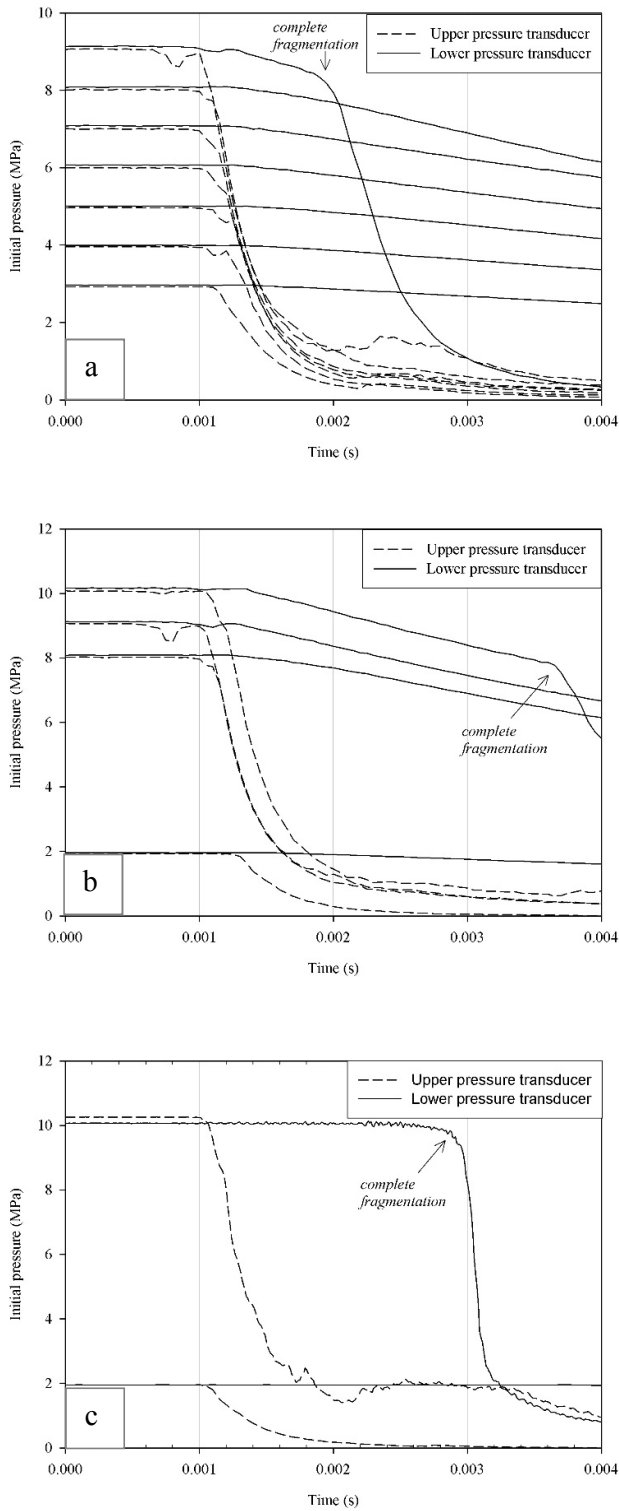


Figure 2.7 Raw pressure decay curves obtained for each permeability and fragmentation experiment. (a) Fragmentation threshold experiments on a Bezymianny-D2 sample cylinder showing pressure loss as recorded by the lower pressure transducer. The kink in the top lower pressure transducer curve corresponds to the complete fragmentation of the sample. Fragmentation lasts ~ 1 ms and outgassing is observed during that very short time frame. (b) Extreme case of outgassing during fragmentation experiments on a sample cylinder from Bezymianny-D2. The sharp kink in the top lower pressure transducer curve corresponds to the complete fragmentation of the cylinder. Fragmentation lasts ~ 2.6 ms, which results in a very low fragmentation speed. (c) Fragmentation speed and permeability test experiments on a Krakatau-D4 sample cylinder showing very little pressure loss.

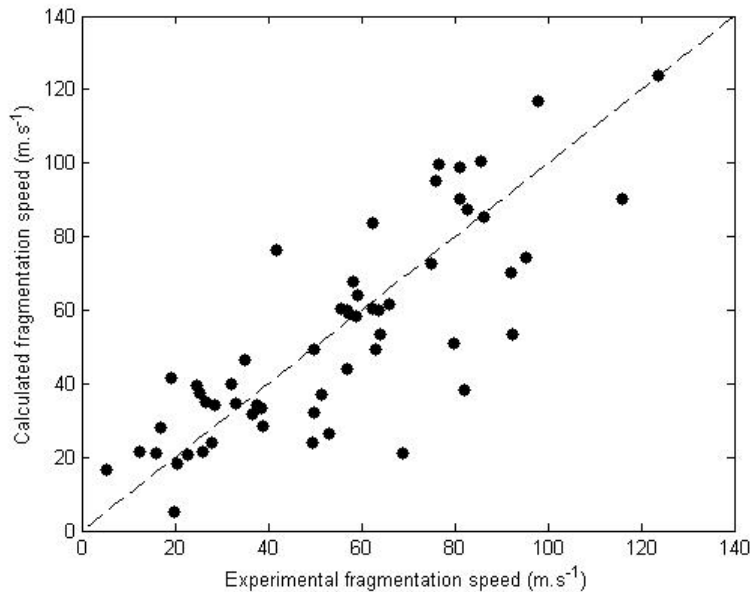


Figure 2.8 Calculated fragmentation speeds (Koyaguchi et al., 2008) plotted against experimental fragmentation speed data from this study. The dashed line represents a 1:1 correlation.

2.4.4 Outgassing during Fragmentation Events

Experiments performed in order to test the fragmentation threshold reveal that outgassing can occur within the time scale of the fragmentation experiments. Initial pressure reduction due to outgassing can be recorded by the lower pressure transducer at the bottom of sample cylinders during fragmentation speed experiments and that, within the time scale of fragmentation of ca. 1-3 ms (Figure 2.7). This pressure loss is observed especially during the Bezymianny-D2 and Colima-D2 experiments. These sample series have $k > \sim 10^{-12} \text{ m}^2$, which is the permeability defined by Mueller et al. (2008) to have a significant effect on fragmentation. Figure 2.7 shows examples of the end-member cases using the contrasting Bezymianny-D2 and Krakatau-D4 sample sets. The pressure loss is directly associated to gas loss and is defined as the difference between the initial pressure P , recorded by both the upper and lower pressure transducers, and the pressure recorded by the lower pressure transducer before it rapidly decays as the fragmentation front reaches the bottom of the sample cylinder. In absence of gas loss, the initial pressure recorded by the lower pressure transducer stays constant until the abrupt pressure drop. The pressure loss that occurs just before the abrupt pressure drop is associated with the passing of the fragmentation front at the bottom of the sample cylinder and is neglected here. This late-stage pressure loss represents gas loss at the scale of the fragmentation layer, which is observed in all of our fragmentation experiments. During the fragmentation of Bezymianny-D2 with $\Phi=45.4\%$, $k=1.1 \times 10^{-11} \text{ m}^2$ and $P=9 \text{ MPa}$, a pressure loss of 0.7 MPa is measured (Figure 2.7a). Some experiments at low initial pressures (usually $<10 \text{ MPa}$) show a high and constant rate in

pressure loss (Figure 2.7b), reducing significantly the energy available for fragmentation. During the fragmentation of Bezymianny-D2 with $\Phi=45.8\%$, $k=2.0 \times 10^{-11} \text{ m}^2$ and $P=10 \text{ MPa}$, a pressure loss of 2.35 MPa is measured. On the other hand, some experiments show very little to no loss of initial pressure. During the fragmentation of Krakatau-D4 with $\Phi=44.2\%$, $k=5.5 \times 10^{-14} \text{ m}^2$ and $P=10 \text{ MPa}$, no significant pressure loss is measured (Figure 2.7c).

2.4.5 Effect of Outgassing on Fragmentation Speed

Each sample cylinder is identified as either having low or high permeability, with 10^{-12} m^2 being the cut-off permeability. The fragmentation speed data are divided into 2 subsets: (a) dome/conduit wall rocks, with average connected porosity 15.6-45.6% (Figure 2.9a), and (b) pumice/scoria, with average connected porosity 44.7-76.2% (Figure 2.9b). For each subset, black symbols correspond to low-permeability samples, and white symbols, to high-permeability samples. We suspected these two subsets to show differing behaviors. Figure 2.9 compares experimental fragmentation speeds (X) with calculated fragmentation speeds (U) for all fragmentation speed experiments in the form of ratios (X/U) and allows us to interpret these ratios relative to the P/P_{th} ratios. Because connected porosity does not appear on Figure 2.9, a direct comparison between sample sets would be inaccurate. The main purpose of this figure is to determine whether we detect an influence of permeability on fragmentation speed, and if so, whether there is a positive or negative correlation. As one might intuitively expect, the model reproduces well the low permeability data and X/U ratios for highly permeable pumice are mostly below the $X/U=1$ line (Figure 2.9). The relatively small scatter for the low- k data points represents both a “natural” deviation resulting from the use of natural samples, and the accuracy of the model for low permeability samples. On the other hand, the scatter is significantly larger for the high permeability data, with experimental fragmentation speeds up to twice as high as calculated fragmentation speeds (Figure 2.9a). As a general trend, highly permeable dome/conduit wall rocks are associated with X/U ratios >1 . However, in experiments where $P \approx P_{th}$, we obtain several fragmentation speeds below the $X/U=1$ line. Colima-C6 experiments exhibit unusual fragmentation behavior. This sample set produces fragmentation speeds up to four times higher than expected, even though its permeability is relatively low (ca. 10^{-13} m^2). These findings support the hypothesis that high permeability, and possibly an additional factor in the case of Colima-C6 discussed in a later section, influence fragmentation speed, adding a degree of difficulty in the prediction of fragmentation speeds.

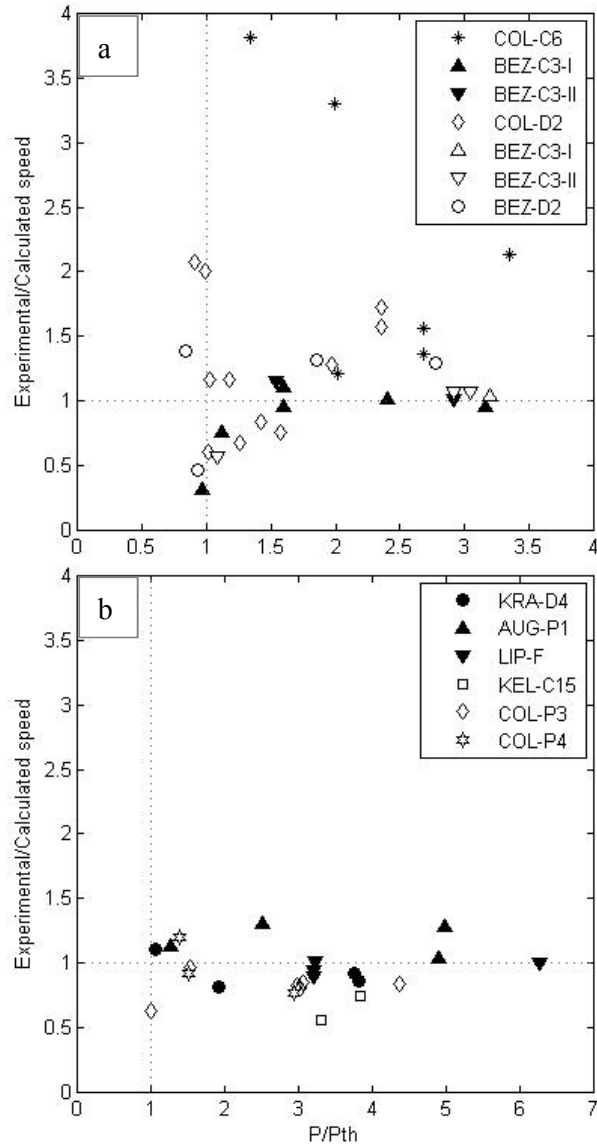


Figure 2.9 Experimental to calculated fragmentation speed ratios (X/U) as a function of initial pressure normalized to the fragmentation threshold of each sample set (P/P_{th}). Data were divided into (a) dome/conduit wall rocks and (b) pumice/scoria, and all sample sets are identified. Black symbols stand for low permeability and white symbols, for high permeability. P_{th} was estimated to 5 MPa for Kelut-C15 and to 6.5 MPa for Colima-P4. The vertical dashed line represents $P=P_{th}$ and the horizontal dashed line, a 1:1 correlation between experimental and calculated fragmentation speeds ($X/U=1$). In both (a) and (b), the low-permeability data (black), except for Colima-C6, lie mostly along the $X/U=1$ line. However, as a general trend, the high-permeability data in (a) lie mostly below the $X/U=1$ line near $P/P_{th}=1$, and above the $X/U=1$ line for higher P/P_{th} values. Experiments near $P/P_{th}=1$ can be influenced by high pressure loss and fragmentation threshold variability. Colima-C6 exhibits unexpected fragmentation behavior.

2.5 Implications for the Fragmentation Process

Our results support previous studies by showing that connected porosity is the dominant parameter controlling the fragmentation of highly viscous magma. However, Bezymianny-D2, Colima-D2, and Colima-P3 represent such examples where connected porosity alone cannot explain the fragmentation threshold. All three sample sets prove to be highly permeable. Regardless of high or low permeability, pressure loss begins with the start of decompression. For low-permeability samples, pressure loss is negligible and can hardly be measured with the pressure drop curves (Figure 2.7c). For samples with permeability above a cut-off permeability of 10^{-12} m², pressure loss is substantial enough (Figure 2.7a and b) to rapidly reduce the initial pressure and to hinder fragmentation initiation. In such cases, higher initial pressures are required to initiate and achieve complete fragmentation. Therefore, it is reasonable to state that high permeability affects magma fragmentation dynamics and results in higher fragmentation thresholds.

2.5.1 Outgassing - Speeding Up or Slowing Down Fragmentation?

As shown above, gas escape through highly permeable rocks, to which we also refer as *outgassing*, can occur within the time scale of fragmentation (ca. 1-3 ms), or even faster, and thereby affect the fragmentation process. We now analyze the effect of outgassing on the fragmentation speed. At first glance, there is scatter on either side of the 1:1 correlation dashed line, and no obvious trend can be observed (Figure 2.8). However, the separation of the samples into the two subsets (a) dome/conduit wall rocks and (b) pumice/scoria reveals two distinct trends (Figures 2.9 and 2.10). Figure 2.9 allows us to interpret our fragmentation speed data with respect to initial pressure, which is normalized to the fragmentation threshold of each sample set. When comparing our experimental fragmentation speeds with the calculated fragmentation speeds, we can say that high permeability influences the speed of fragmentation of porous volcanic rocks, but its effect varies depending on the rock type:

(1) dome/conduit wall rocks

Outgassing in highly-permeable dome/conduit wall rocks correlates with increased fragmentation speeds (Figure 9a). However, at $P/P_{th} \sim 1$, we observe a large variability in the X/U ratios. Explanations for the high ratios are that (a) P/P_{th} is in some cases higher than that plotted on Figure 2.9 due to the variability in fragmentation thresholds within a sample set (Table 2.2) or (b) the sample cylinders contained inhomogeneities such as large cavities or fractures which weakened the sample cylinder. In contrast, several low X/U ratios suggest that high permeability may often correlate with reduced fragmentation speeds when the initial pressure is too close to the fragmentation threshold ($P/P_{th} \sim 1$) and that pressure loss is substantial, as shown on Figure 2.7b. Fragmentation speeds for two low- k dome/conduit wall rock sample cylinders are also below the $X/U=1$ line. The lowest X/U ratio

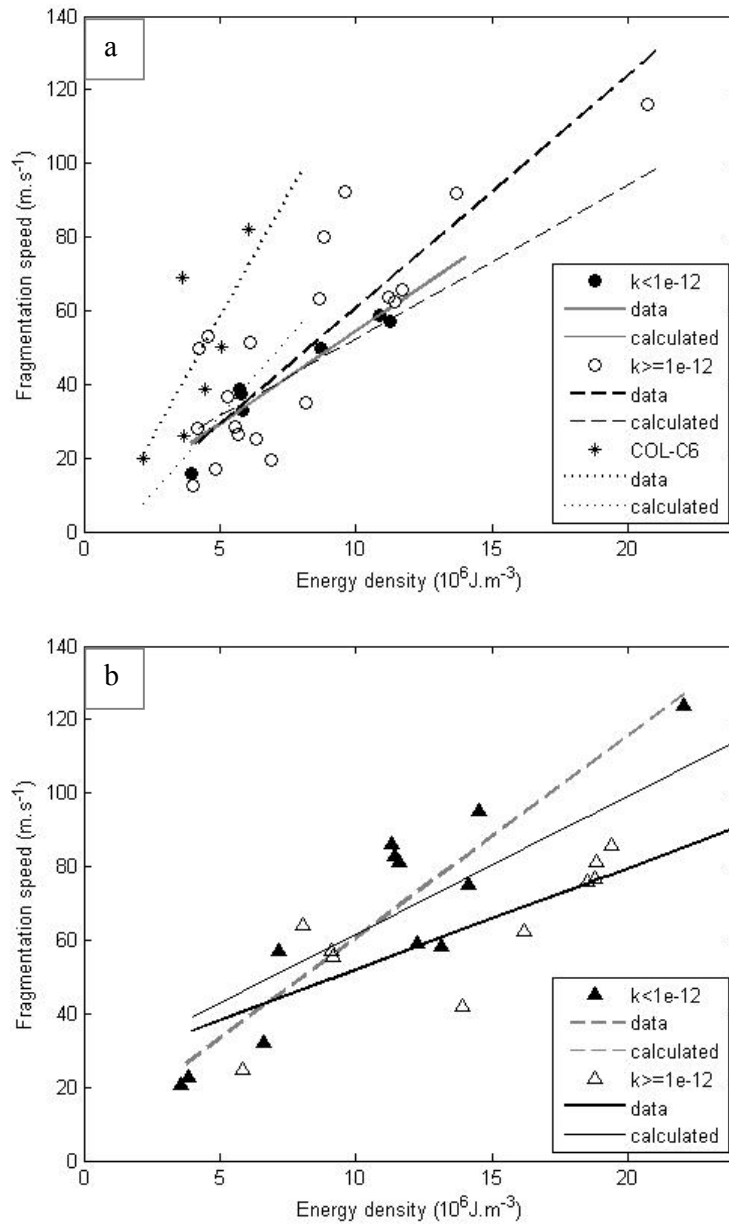


Figure 2.10 Experimental fragmentation speed data plotted against fragmentation energy density data. Black symbols stand for low permeability and white symbols, for high permeability. Comparing the effect of permeability on fragmentation speed between sample sets is easier due to the consideration of both P and Φ in the energy density calculation. In addition, linear fits to calculated fragmentation speeds (Koyaguchi et al., 2008) are plotted together with the linear fits to the experimental fragmentation speeds. Results are divided as in Figure 2.9 (a) dome/conduit wall rocks and (b) pumice/scoria. COL-C6 and high- k dome/conduit wall rocks fragment at higher speeds than expected and high- k pumice, at lower speeds than expected. Linear fits of experimental and calculated fragmentation speeds of the low- k data overlap.

corresponds to an experiment where the initial pressure probably equaled the threshold value for this specific sample cylinder and the fragmentation speed was for this reason very low. The second X/U ratio corresponds to a sample cylinder that went through repeated experiments to evaluate its fragmentation threshold. Repeated experiments at P close to P_{th} could in some instances create small fractures and increase the permeability. However, as a general trend, low- k dome/conduit wall rocks behave as predicted, high- k dome/conduit wall rocks fragment at higher speeds than would be expected, and it remains a challenge to predict the fragmentation speed for high- k dome/conduit wall rocks around initial pressures close to the fragmentation threshold.

(2) pumice/scoria

Outgassing in highly-permeable pumice results in reduced fragmentation speeds for the complete range of initial pressures tested in this study, except for one data point that lies above the $X/U=1$ line (Figure 2.9b, white star). The fragmentation behavior of this rock type is more predictable.

We did consider the possible effect of isolated porosity on the fragmentation process in that it could slightly reduce the strength of the sample. However we could not detect any influence in our experiments. The low percentage of isolated porosity compared to the connected porosity (Table 2.1) most likely explains this lack of influence of the isolated porosity on the fragmentation process.

High- k dome/conduit wall rocks behave differently from high- k pumice when fragmented under high pressures. Based on our evidence, we suggest that outgassing slows down the fragmentation process in the case of highly-permeable pumice, but speeds up the fragmentation process in the case of highly-permeable dome/conduit wall rocks at least for initial pressures well above threshold.

Linear trends fitting fragmentation energy density data to fragmentation speeds allow us to describe empirically these differing fragmentation behaviors and support our interpretations for these two subsets (Figure 2.10, Table 2.4). Fragmentation speeds for initial pressures below the fragmentation threshold are not included in the comparison of the calculated and experimental linear fits to avoid skewing the fit. The linear fits to the Colima-C6 (15.6%) (Figure 2.10a) and pumice ($k > 10^{-12} \text{ m}^2$) (Figure 2.10b) data clearly stand out. The linear fit to the dome/conduit wall rocks ($k > 10^{-12} \text{ m}^2$) data lies significantly away from calculated fragmentation speeds (Figure 2.10a). Both the low- k pumice/scoria and dome/conduit wall rocks behave as defined by the Koyaguchi et al. (2008) model. As a side note, the experimental fragmentation speeds for Bezymianny-C3 I and Bezymianny-C3 II are comparable despite the fact that the two sample series were drilled perpendicularly to each other. This is most likely because the permeability values for both sample series lie mostly below 10^{-12} m^2 .

Table 2.4 Parameters m and b for the linear fits to energy density data. m represents the slope, b , the y-intercept.

| Sample groups | m | b |
|-----------------------------------|-------|-------|
| low- k dome/conduit wall rocks | 7.53 | 4.12 |
| low- k pumice/scoria | 8.22 | 6.07 |
| high- k dome/conduit wall rocks | 9.49 | -2.48 |
| high- k pumice | 4.15 | 24.35 |
| Colima-C6 | 19.87 | -7.79 |

2.5.2 Gas Flow Dynamics Considerations

To quantify the importance of outgassing during fragmentation speed experiments, we estimate the magnitude of pressure loss, following the method described in the results section for Figure 2.7. Interestingly, high- k dome/conduit wall rocks experience a higher gas pressure loss than the high- k pumices for any given permeability above $k \sim 10^{-12} \text{ m}^2$ (Figure 2.11).

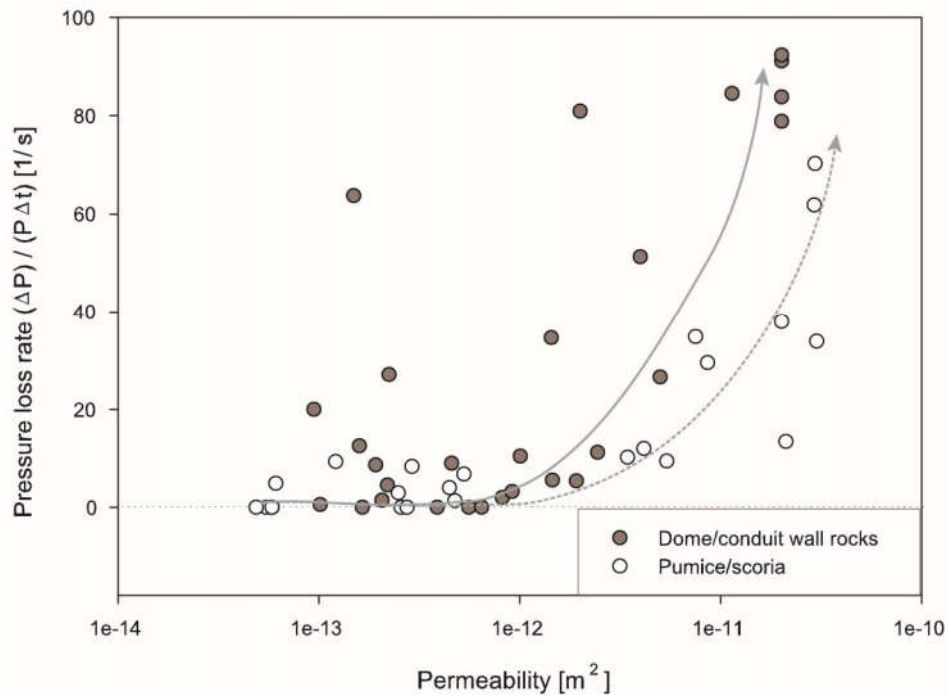


Figure 2.11 Gas pressure loss rate during fragmentation speed experiments is significantly greater for the dome/conduit wall rocks than for the pumice/scoria. The solid line refers to the dome/conduit wall rocks, and the dashed line, to the pumice/scoria. These schematic trends show that, for the dome/conduit wall rocks, the onset of significant gas pressure loss, at $k \sim 10^{-12} \text{ m}^2$, occurs before that of the pumice/scoria. The vertical scatter in the dome/conduit wall rocks data may suggest an increase in the permeability during the fragmentation of some sample cylinders.

Permeability is influenced by textural properties, such as bubble size, bubble aperture size, bubble shape, bubble size distributions, tortuosity of the pathways and/or the presence of crystals (e.g. Carman, 1956; Dullien, 1992; Kozeny, 1927; Saar and Manga, 1999; Wright et al., 2009). The high- k dome/conduit wall rocks have a bubble network that can be approximated by the capillary tube (e.g., Carman, 1956; Kozeny, 1927) and/or fracture flow model (e.g., Lamb, 1945; Langlois, 1964). Bezymianny-D2 and Colima-D2 represent low-tortuosity examples where bubbles have most likely partly collapsed due to shear deformation within a conduit or a dome, and where permeability has increased also due to the shear deformation (D'Oriano et al., 2005; Saar and Manga, 1999; Wright et al., 2009). On the other hand, the high- k pumices have a bubble network that can be better approximated by the fully-penetrable-sphere percolation theory model (e.g. Saar and Manga, 1999; Sahimi, 1994). Colima-P3, Colima-P4 and Kelut-C15 have experienced bubble expansion and coalescence, but little shear deformation. Their bubble network is more tortuous than the bubble network from dome/conduit wall rocks. The length and curvature of paths followed by the gas during outgassing must differ substantially for the two types of bubble networks. We therefore suggest that differences in bubble network textures between high permeability effusive (dome/conduit wall rocks) and high permeability explosive (pumice) volcanic rocks could be linked to differences in fragmentation speed.

The flow of fluid through porous media can be characterized based on the relative influence of viscous (friction along walls) and inertial forces (such as turbulence) acting upon this flow. A flow dominated by viscous forces can be described by Darcy's Law which predicts the fluid flow rate for a given pressure gradient, dynamic fluid viscosity, permeability, sample length and cross-sectional area. The fluid flow rate varies proportionally to changes in pressure gradient, which is valid for very low Reynolds numbers. For very large Reynolds numbers and Forchheimer numbers greater than 1, inertial forces become dominant over viscous forces, and the flow is non-Darcian (turbulent) (Ruth and Ma, 1992). In a non-Darcian flow, flow rates vary non-linearly to changes in pressure gradient (Bear, 1972; Forchheimer, 1901). The Forchheimer number considers both the flow velocity and the structure of the porous network and is therefore an accurate means to distinguish Darcian from non-Darcian flow (Ruth and Ma, 1992).

We propose that the observed differences in bubble network textures (or structure) play a significant role in the efficiency of outgassing at high initial pressures above P_{th} . Degruyter et al. (2012) have shown, using a numerical model, that variations in the textural properties of magma have an important effect on outgassing dynamics in the context of eruptive style transitions. We suggest that textural variations could explain differences in fragmentation speed between high- k dome/conduit wall rocks and high- k pumice. When our high-permeability rocks are submitted to high pressure fragmentation experiments where $P > P_{th}$, we can assume that gas flow rates, as in permeability measurements from Rust and Cashman (2004), correlate non-linearly with pressure gradients due to the large inertial effects. We could also expect that the effect would be similar for dome/conduit wall rocks and pumices. Yet, highly-permeable

dome/conduit wall rocks outgas more quickly than highly-permeable pumice (Figure 2.11). We argue that gas flow rates through the highly-permeable pumice decrease more significantly with high pressure gradients than through the highly-permeable dome/conduit wall rocks because of greater tortuosity of the flow paths and/or other textural differences such as bubble aperture size.

Both the velocity of the gas, which is directly related to the pressure gradient, *and* the bubble network texture (or structure) determine whether a flow behaves in a Darcian or non-Darcian manner (Bear, 1972; Rust and Cashman, 2004; Ruth and Ma, 1992). Gas flow through tortuous paths is associated with increased inertial effects, leads to non-Darcian flow, and dissipates energy viscously (Ruth and Ma, 1992). Moreover, gas flow velocity is a determinant parameter in the generation of turbulence, an inertial effect that occurs at Forchheimer numbers greater than 1. Highly-permeable dome/conduit wall rocks have a bubble network that can be compared to a straight tube model, and highly-permeable pumice, to a bent tube model. It has been shown that turbulence occurs in the straight tube model for much higher Reynolds numbers and gas flow velocities than in the bent tube model (Ruth and Ma, 1992). Gas flow disturbances most certainly occur in highly-permeable dome/conduit wall rocks, only to a lesser extent. Rust and Cashman (2004) found experimentally that both viscous and inertial effects increased resistance to the gas flow in the case of helical pore samples in comparison to straight tube samples. These observations support that at high pressure gradients, gas flow rates increase, but the rate of increase most likely differs for the two bubble network textures, which would explain the observed differences in gas pressure loss rates between dome/conduit wall rocks and pumice/scoria (Figure 2.11).

The positive correlation between pressure loss rates and fragmentation speeds in the case of high- k dome/conduit wall rocks has been established. We suggest that very rapid gas escape in high- k dome/conduit wall rocks could possibly contribute to, and accelerate, the layer-by-layer fragmentation process. Following is our reasoning for such a statement. Gas flowing at subsonic speeds decelerates when it reaches a larger cross-sectional area and gas flowing at supersonic speeds accelerates when it reaches a larger cross-sectional area (Liepmann and Roshko, 1957, p.52). In the case of high- k dome/conduit wall rocks, the gas flow has the potential to reach supersonic speeds inside the sample cylinder, and when the cross-sectional area suddenly increases at the top of the sample cylinder, the gas flow rate could further increase. As a consequence, fragmented material gets moved away from the sample cylinder at a higher velocity and the overpressure inside the sample cylinder rebuilds more quickly (Fowler et al., 2010, Figure 2.4). This explanation could also apply in the case where the gas flows at subsonic speeds, because gas flow rates would nevertheless be higher than for high- k pumice. An additional effect of outgassing on the fragmentation process is that it can reduce the suction (described in Fowler et al., 2010) that acts upon a fragmented layer as the created and expanding void has to be filled and the fragmented layer moves away from the sample cylinder. Whether the gas flow reaches supersonic speeds or not, the fact remains that (a) the experimental

fragmentation speeds and pressure loss rates in the high- k dome/conduit wall rocks are higher than in the high- k pumice and (b) more efficient outgassing in high- k dome/conduit wall rocks than in high- k pumice could have a significant suction reduction effect, allowing us to suggest that higher gas flow rates accelerate the fragmentation process.

2.5.3 Fragmentation of Altered Dome Material

Interestingly, low connected porosity and low permeability of Colima-C6 cannot explain why fragmentation speeds are high for relatively low energy inputs and clearly above the general trend (see Figure 2.10). Another parameter is required to explain higher fragmentation speeds. It is worth noting that its fragmentation threshold, although close to the fragmentation criterion, plots in the lower range of experimental threshold values for its connected porosity value (Figure 2.3). This andesitic sample has a groundmass that contains plagioclase microlites of no preferred orientation, oxides and very small amounts of glass (<1%). Edges from phenocrysts are diffuse due to the growth of microlites and chloritization of the groundmass, and represent evidence of possibly thermal and hydrothermal alteration. As mentioned before, this sample was extruded and most likely remained part of the dome for a relatively long time before tumbling down the volcano. Continuous viscous deformation within the dome may cause outgassing, explaining low permeability and reduced connected porosity. This sample does not represent fresh material, but an altered version of the fresh material (Colima-D2) with the glassy groundmass being almost fully crystallized. Alteration may influence the rock strength in at least two ways: (1) circulation of hydrothermal fluids through the fresh material could lead to the sealing of fractures due to crystallization, resulting in a strengthening of the rock, whereas (2) alteration of the groundmass and phenocrysts would result in a lower yield strength and significant weakening of the dome rocks, leading to a low fragmentation threshold. Accordingly, the effective tensile strength of the material's solid phase (S) in Equation 2 would have to be adjusted in order to adequately model the fragmentation of these altered rocks. For Colima-C6 only signs pointing to a weakening of the rock were found, such as alteration of the groundmass and phenocrysts. Thus S would have to be reduced to account for the weakened rock. As a result, more energy would be available for the fragmentation of the rock, which in turn would have an impact on the ejection velocity of the particles (Alatorre-Ibargüengoitia et al., 2011; Alatorre-Ibargüengoitia et al., 2010). Our observations are based on one sample set only, but represent nevertheless strong evidence for the more energetic fragmentation of weakened dome rocks.

We suggest that altered, almost fully-crystallized, low-permeability and low-porosity dome rocks may represent weak zones within the dome that could fragment at relatively high speeds for low initial pressures. Similarly to the fragmentation scenario described in Scheu et al. (2006), the fragmentation of weaker zones could in turn reduce the overburden and cause the

fragmentation of the more permeable dome rocks that require higher initial pressures. Further studies are required in order to support these findings.

2.6 Concluding Remarks

In summary, our experimental results support the results from Mueller et al. (2008) that permeability and porosity control the amount of energy available for fragmentation. The amount required is determined by the properties of the rock to be fragmented. Permeability higher than 10^{-12} m² results in higher fragmentation thresholds. In addition, outgassing during the fragmentation process significantly affects fragmentation speed. Highly-permeable dome/conduit wall rocks fragment with increased speeds whereas high-*k* pumices fragment with decreased speeds. Fragmentation speeds for initial pressures close to the fragmentation threshold are more difficult to predict in the case of highly-permeable dome/conduit wall rocks, but our results suggest that the speeds are mostly reduced. In order to explain our findings regarding the high-*k* experiments at high initial pressures, we suggest that inertial effects during outgassing affect the permeable gas flow rates within the bubbly magma, which in turn affects the pressure gradient at the scale of the fragmentation layer and the removal of the fragmented material. The result is the deceleration or acceleration of the fragmentation process depending on the bubble network texture of the rocks. The alteration of dome/conduit wall rocks may also lead to increased fragmentation speeds by reducing the amount of energy consumed by fragmentation. Our findings apply to the fragmentation of highly viscous bubbly magma (not considering bubble nucleation and growth) that occurs during rapid decompression events associated with dome collapses, landslides and Vulcanian eruptions.

The effect of outgassing on conduit flow dynamics has been included in many numerical models as a process conducive to effusive eruptions. One assumption was that outgassing is not significant within the time scale of the magma fragmentation process (Jaupart and Allègre, 1991; Melnik et al., 2005). Our results clearly show that this is not always the case. Significant outgassing can occur within time scales of a few milliseconds and should be taken into consideration when attempting to understand the migration of a fragmentation front through permeable magma in a volcanic conduit or lava dome. The amount of material that is erupted during a single eruptive event is in part controlled by the migration of this fragmentation front. The speed at which this front migrates will influence the duration and style of the eruption. Numerical and theoretical models may need to include outgassing and dome rock weakening to reproduce more closely observed explosive eruptions and forecast future eruptions.

3

The Emplacement and Cooling of a Peralkaline Spatter-Fed Rheomorphic Deposit from Pantelleria

3.1 Introduction

Estimating the time frame within which a lava flow or pyroclastic density current deposit cooled is potentially key in unraveling the emplacement story of a deposit. This is especially intriguing in the case of peralkaline melts, which have very low viscosities at eruption and can remain viscous for an extended period of time after eruption. The eruption of magma, this mixture of melt, crystals and volatiles, often leads to the formation of deposits containing variable amounts of glass. Cooling rates of natural glasses have been successfully estimated for occurrences in lavas (Gottsmann and Dingwell, 2001b; Gottsmann et al., 2004), spatter-fed rheomorphic lavas (Gottsmann and Dingwell, 2001a, 2002), a rheomorphic ignimbrite (Lavallée et al., 2015),

individual volcanic bombs (Wilding et al., 1996a) and tektites (Wilding et al., 1996b) using the Tool-Narayanaswamy-Moynihan (TNM) method (Moynihan et al., 1976a; Moynihan et al., 1974; Narayanaswamy, 1971; Tool, 1946) of enthalpic relaxation geospeedometry.

However, until now cooling rates obtained with the TNM method are modeled assuming linear cooling through the glass transition and to ambient conditions. This does not pay heed to the complexity of cooling trajectories in nature and does not account for near-isothermal conditions in the glass transition interval that can result in annealing and complication of the theory from which the cooling-rate estimates are derived. Processes occurring at the lower end of the glass transition can complicate the use of such methods. In fact, Gottsmann and Dingwell (2002) have suggested that some of their cooling rate estimates were most likely influenced by thermal annealing. Thermal annealing at the lower end of the glass transition may compromise the accuracy of modeled cooling rates and thus falsify the cooling record as recorded by the melt in the glass transition, by allowing additional structural relaxation of the glass. The time-temperature path of magma is a continuous process but is rarely reliably approximated by simple linear or other functional cooling. For example, complications arise when emplacement of a lava followed by overflow of a second lava on top creates a time-dependent temperature distribution that may be hard to unravel from a deposit. In this scenario, for example, the second lava flow would at least insulate if not reheat the first underlying lava. Preliminary analyses on pantelleritic glass from the 7.6 ka Cala di Tramontana rheomorphic spatter-fed deposit produced in part very low modeled cooling rates and hint at a significant effect of thermal annealing on the structure of the glasses.

This study characterizes the exceptionally structurally strong (Angell, 1985; Di Genova et al., 2014) pantelleritic melts and tests experimentally the effect of thermal annealing on remelted pantelleritic obsidian from the 7.6 ka Cala di Tramontana volcanic deposit, interpreted as a rheomorphic spatter-fed flow deposit (Stevenson and Wilson, 1997). We suggest that thermal annealing close to the onset of the glass transition allows for significant additional relaxation of the structure of glasses and thereby lowers the modeled cooling rates. Successful thermal expansion analyses (Stevenson and Wilson, 1997) showed that the glass is suitable for an enthalpy relaxation geospeedometry study. We explore, and attempt to quantify, the effect of thermal annealing on the structure of glasses below the peak glass transition temperature in order to better interpret modeled cooling rates. We then discuss the conditions that must prevail in order to produce an isothermal hold during the cooling process of deposits such as the Cala di Tramontana spatter-fed rheomorphic deposit.

3.2 Background

3.2.1 Glass

Glass is an amorphous solid material with a three-dimensional atomic structure which, unlike crystalline counterparts, lacks long range order (Figure 3.1). The main factors that control the formation of glass from a melt are: (1) composition, (2) temperature and (3) cooling history of the melt. The conditions conducive to glass formation are also the conditions that hinder crystallization, since a fully-crystallized magma does not contain any glass.

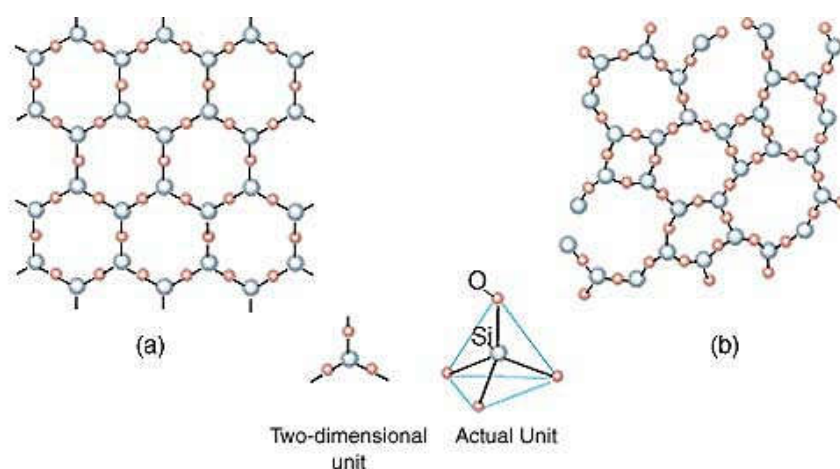


Figure 3.1 Schematic representation as plane view of (a) crystalline SiO₂ (quartz) and (b) SiO₂ glass. The tetrahedron shows the actual configuration of the silicon and oxygen atoms. Source: Tarbuck and Lutgens, (2011)

3.2.2 Glass Transition

The glass transition occurs only within a temperature window of ca. 100-150 °C, for most natural silicate melts at the Earth's surface, however, along the cooling path of a melt from eruption (up to ca. 1200 °C) to ambient temperature, it should not be overlooked as it has proved to be crucial to the understanding of many volcanic processes. The glass transition represents a kinetic boundary defined as a temperature interval between the liquid-like (dominantly viscous) and solid-like (dominantly elastic) behavior of a melt in response to applied stresses (Figure 3.2 and 3.3) (e.g. Dingwell and Webb, 1990). It is the boundary between flow and fracture, and arguably, between effusive and explosive eruption styles, between motion and deposition of a volcanic flow. The melt composition and volatile content have a strong influence on the temperature range where this transition occurs. For example, a calc-alkaline rhyolite may have a peak glass transition temperature ($T_{g_{peak}}$) of ca. 700 °C whereas a peralkaline rhyolite may

have a $T_{g_{peak}}$ of ca. 530 °C for a cooling and heating rate of ca. 10 K min⁻¹. Hess et al. (1995) documented this remarkable effect experimentally. In addition, the temperature at which a melt enters the glass transition is controlled by its cooling rate and/or by the strain rate in the melt. High cooling rates (e.g. 10⁵ K s⁻¹) result in a large amount of stored potential energy in the glass structure and an internal structure representative of much higher temperatures than the glass transition temperature obtained from the heat capacity (C_p) trace (e.g., Yue et al., 2002a). This has been evidenced by a deep trough in the heat capacity trace below the glass transition (e.g., Potuzak et al., 2008; Yue et al., 2002a). Depending on the rheological properties of the flowing magma, sufficiently high strain rates (Goto, 1999) can also lead to the glass transition. However, after the applied stress is removed, the magma may return to a liquid state via relaxation.

By heating a glass across the glass transition, an “enthalpy relaxation peak” forms in the C_p trace, which represents an endothermic process occurring in the glass. This peak is amplified if the glass experienced annealing at a temperature sufficiently high to allow a reorganization of the internal structure of the glass. Adams and Williamson (1920) were amongst the first scientists to study the process of annealing in glasses, as reported by Mysen and Richet (2005).

3.2.3 Structural Relaxation

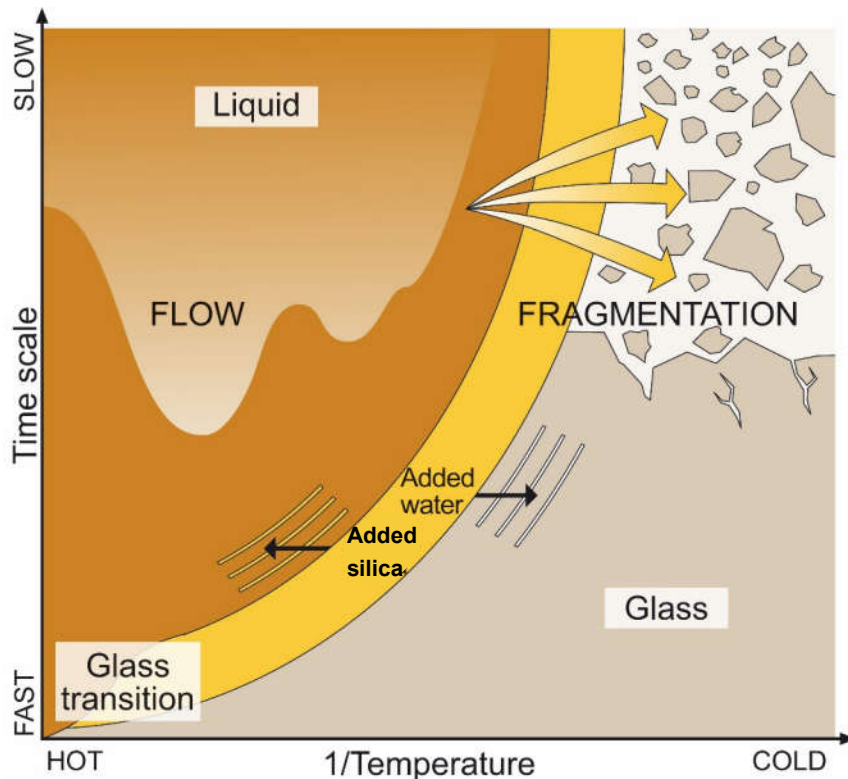


Figure 3.2 The glass transition between glass and liquid.

When entering the glass transition upon cooling, the melt's structural arrangement departs from equilibrium. The minimum time required for the melt to re-equilibrate is greater than the time available at a specific temperature due to the given cooling rate. At some value of temperature for a given cooling rate, the structure is no longer able to viscously rearrange and on continued cooling below this temperature, the material behaves as an elastic solid: a glass. The temperature at which this occurs depends on the composition of the glass, including the volatile content, the cooling rate at which the glass was formed and on any subsequent time spent close to $T_{g_{onset}}$ where time-dependent annealing can occur.

Any temperature change in a viscous liquid requires molecular processes and adjustments in the arrangement of the molecules to return to a metastable state of equilibrium in the liquid (Tool, 1946). The adjustments may be seen as occurring in at least two steps: (1) fast process by which the length of the molecular bonds changes (2) slow process by which the arrangement of the molecules is modified to reach a new equilibrium structure via a so-called α -relaxation. The time required for a melt to relax via α -relaxation (τ) may be approximated by Maxwell's law of linear viscoelasticity (Maxwell, 1867)

$$\tau = \frac{\eta_N}{G_\infty} \quad (1)$$

for a given Newtonian viscosity, η_N (Pa s), and shear (rigidity) modulus, G_∞ (Pa) at infinite high frequency. Dingwell and Webb (1990) have estimated G_∞ to be an approximately constant value of 10 GPa. When a melt cools at a given rate ($q = \Delta T/\Delta t$), the cooling can be seen as a series of temperature steps (ΔT) followed by isothermal segments of duration (Δt) (Figure 3.4).

Above the glass transition in the supercooled liquid region, the structure of the melt remains in equilibrium ($\Delta t > \tau$) and, using the analogy of the Maxwell model, the thermally induced stress is dissipated viscously in response to temperature changes. For the purpose of this study, we will focus on temperature-related disturbances of the melt. Decreases in temperature impose stress on the melt, to which the melt responds. A relatively fast response to return to equilibrium is vibrational and involves changing bond lengths. A relatively slow response relates to the rearrangement of the bonds and is thus configurational (Moynihan et al., 1996). Above the glass transition, the melt is able to relax and reorganize its structure to acquire a new equilibrium configuration. Once in the supercooled liquid field, the melt is in a metastable equilibrium. Once the melt reaches the glass transition and continues to cool down, the atoms forming the melt are progressively less capable of adjusting the bonds joining them ($\Delta t < \tau$) and relaxing in order to eliminate stress in the melt structure (Figure 3.4). This creates disequilibrium in the melt structure.

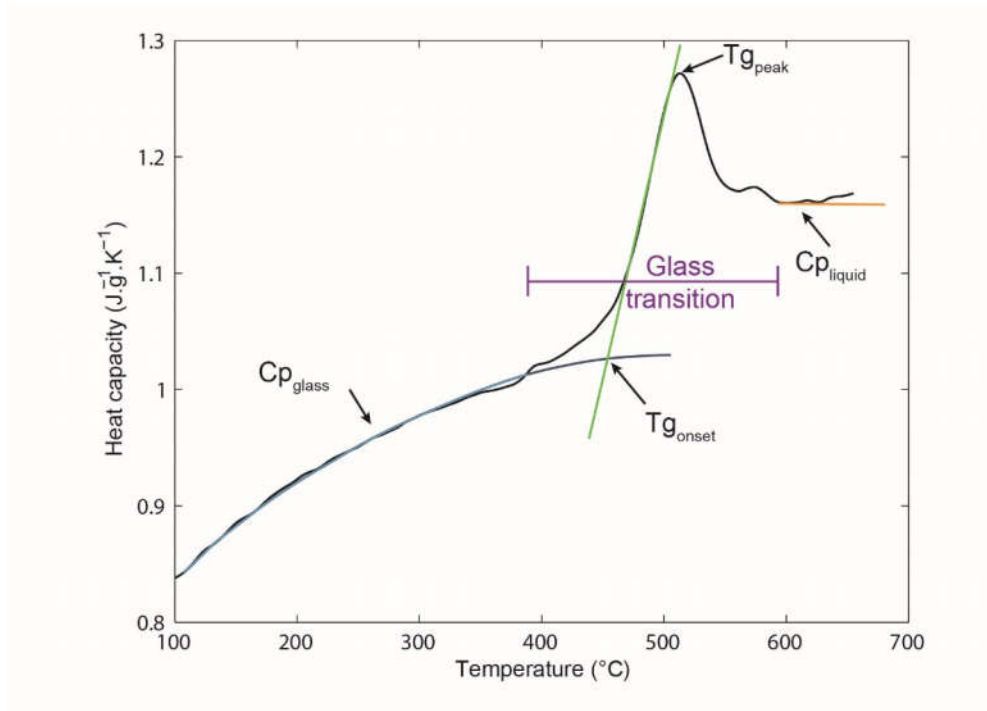


Figure 3.3 Description of a heat capacity curve resulting from the first heating of a natural glass, here TRM1B, in the differential scanning calorimeter (DSC). The glass transition temperature range is between the glassy state and the liquid state of the melt. The extrapolated $T_{g_{onset}}$ can be used to localise the glass transition instead of $T_{g_{peak}}$ and helps us to identify the onset of viscous behaviour for a given heating rate.

Although thermal equilibrium is reached relatively quickly after a temperature step, the rearrangement of the structure of the melt lags behind and does not reflect the actual temperature of the melt, but instead, a *fictive* or *equilibrium* temperature T_f (Tool, 1946), higher than the actual temperature T . This fictive temperature may have actually no physical meaning (Mauro et al., 2009) but the concept has nevertheless proved very useful in tracking the evolution of a physical property. Once the melt reaches a temperature where its structure can no longer relax ($\Delta t \ll \tau$), the melt becomes a glass, and could respond to stress in a brittle manner. The fictive temperature representing the lower end of the glass transition is the *limiting fictive temperature*, where the structure is frozen into the glass.

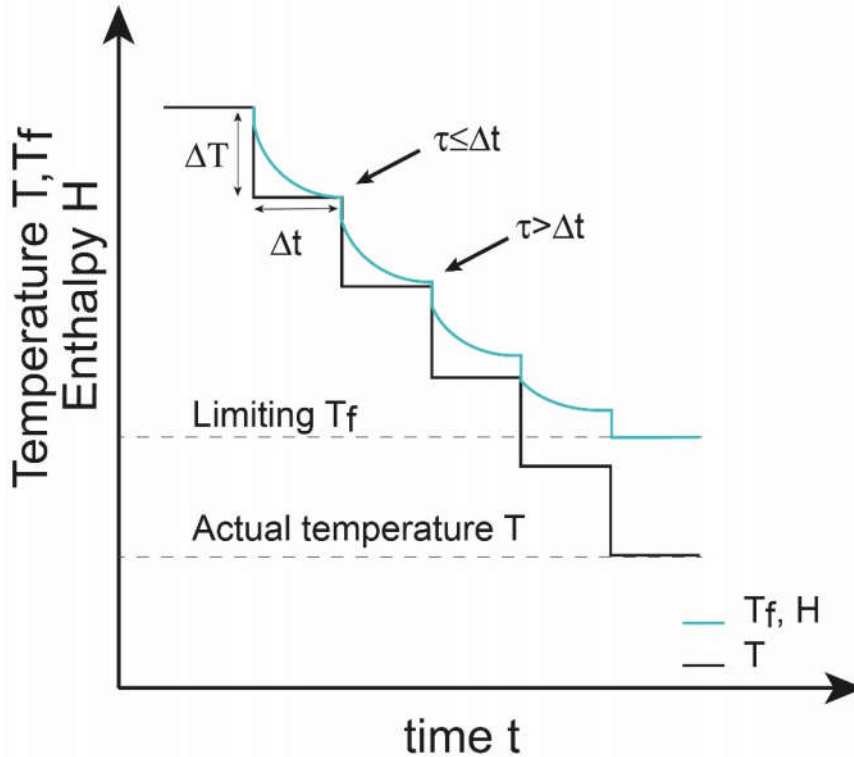


Figure 3.4 Schematic representation of the concept of fictive temperature during cooling of a melt through the glass transition. The actual temperature T decreases with ΔT steps. T_f and H decrease first to reach quickly thermal equilibrium and decrease more slowly as the molecular configuration adjusts to the temperature change. The structure readjustments start to lag behind when the relaxation time τ of the melt is greater than the time Δt given for relaxation between two ΔT steps. When T_f does not change anymore, limiting T_f has been reached and the melt structure is frozen into a glass (redrawn from Moynihan et al., 1996).

Macroscopic physical properties (p) of melts such as thermal expansivity, refractive index, electrical conductivity and heat capacity are influenced by the structural configuration of the melt. Therefore, by measuring changes in these properties, we indirectly measure changes in the melt's structural configuration. It is convenient to use the concept of fictive temperature to explore a phenomenological interpretation of changes in a structure-dependent physical property, and deduce what was the cooling rate of a glass as it crossed the glass transition. Structural relaxation upon heating of a glass depends in part on the cooling rate of the melt at which it passed through the glass transition, a phenomenon called the *memory effect* (Ritland, 1956). This effect refers to the theory that structural relaxation is characterized by a distribution, or spectrum, of relaxation times, as discussed in detail by Goldstein (1964), instead of one unique relaxation time at a given temperature for a given melt composition. In relaxation geospeedometry, the method of extracting the cooling rate at which the glass was first formed, the stretched exponential parameter β is used to describe the decay of the structural relaxation rate with temperature.

3.2.4 Enthalpy Relaxation Geospeedometry

Following eruption, magma follows a unique specific temperature-time path which depends on the evolving thermal properties of the magma and, changing external conditions and the ambient final conditions. Enthalpy relaxation geospeedometry enables us to constrain empirically the rate at which glass-containing deposits have cooled in nature, but only for the time that the melt crossed the glass transition. This method is based on the concept of fictive temperature, which is used to mirror the changing structural configuration of a melt with temperature and time (Figure 3.5). When a melt cools through the glass transition to form a glass, it retains a specific structure which depends partly on its previous cooling rate. By measuring changes in a physical property p such as C_p , the rate of change of relaxation enthalpy with temperature ($\Delta H/\Delta T$) at constant pressure, during reheating and cooling of a natural glass across the glass transition, we indirectly probe the glass or melt for its changing structure.

This method is best applied to peralkaline glasses for which the hysteresis upon reheating is most pronounced (Knoche et al., 1994) and ΔC_p , the C_p difference between $C_{p\text{liquid}}$ and $C_{p\text{glass}}$ at constant pressure, is larger (Di Genova et al., 2014). The C_p traces (at 1 bar pressure) have a clear, pronounced peak that is easily modeled, contrarily to calc-alkaline glasses. Pantelleritic melts have a very low viscosity for a given temperature relative to a rhyolite of the same silica content. Remarkably, at eruptive temperature, they share a viscosity range with eruptable basaltic melts, and yet they are very strong melts, a property which allows them to be such good glass formers contrary to basalts.

Following the TNM model, DeBolt et al. (1976) have adapted the equations to track the evolution of T_f across the glass transition in a recursive manner. T_f is calculated by adding the summation of m adjusted temperature increments to the starting temperature T_0 , which is well above the glass transition. As the melt crosses the glass transition, $\Delta t < \tau$ and the partially adjusted melt structure is representative of shorter T steps. The T_f calculations are performed until T is well below the glass transition and then again back up to T_0 , producing a continuum of T_f . Each T_f is dependent of the preceding sequence of added reduced T steps, and is calculated as follows (Debolt et al., 1976):

$$T_{f,m} = T_0 + \sum_{j=1}^m \Delta T_j \left[1 - \exp\left(-\sum_{k=j}^m \Delta T_k / q_k \tau_{0k}\right)^\beta \right] \quad (2).$$

$T_{f,m}$ is the fictive temperature after m temperature steps ΔT_j , and each ΔT_j represents $[T_j - (T_{f,j-1})]$, where j is one given step in the series of $T_{f,m}$ calculations from $j = 1$ to m . q_k is the experimental cooling or heating rate (K s^{-1}), depending on whether the calculations model the

cooling or heating treatment and τ_{0k} is the relaxation time. The expression contained in the parentheses of equation (2) is the structural relaxation function rewritten from the Kohlrausch-William-Watts (KWW) function (Williams and Watts, 1970)

$$p = p_0 \exp\left[-(t / \tau_{0k})^\beta\right] \quad (3).$$

This empirical expression allows us to quantify the deviation of T_f from T following a sudden ΔT_k , which is kept constant here at 1 K. β , a temperature-independent parameter when assuming that the thermorheological simplicity (Narayanaswamy, 1971) applies, represents the width of the distribution of relaxation times. Therefore, the relaxation time varies with temperature, but the distribution of the relaxation times across the glass transition stays constant. The shape of the distribution is defined by the exponent β . Equation (3) is non-exponential if $\beta \neq 1$. Equation 2 is used to calculate T_f in a continuous manner with temperature steps of 1 K during cooling and subsequent heating, tracking its rate of change ($\Delta T_f / \Delta T$) relative to the actual temperature T . $\Delta T_f / \Delta T$ can be directly compared to the rate of change of a number of physical properties with T and we can use this relationship to model the structural relaxation of glasses in the glass transition.

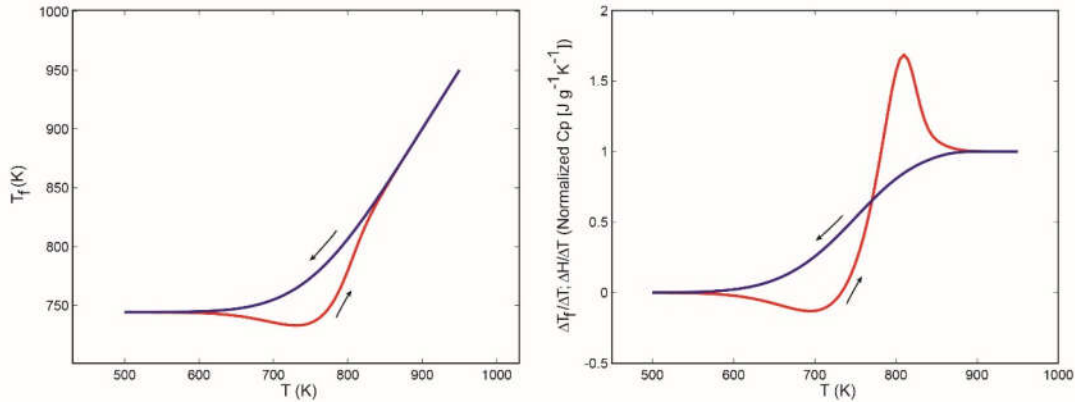


Figure 3.5 Evolution of the fictive temperature T_f relative to actual temperature T for sample TRM1B during cooling and subsequent heating at 10 K min^{-1} . Only the model curves are shown, not the data. (a) T_f decreases in a straightforward manner whereas it increases with a hysteresis (b) Rate of change of T_f , or of a physical property p such as enthalpy.

The relaxation time equation (Narayanaswamy, 1971)

$$\tau_{0k} = A \exp\left[\frac{x\Delta H}{RT_k} + \frac{(1-x)\Delta H}{RT_{f,k-1}}\right] \quad (3)$$

includes the parameter x for the relative influences of T and T_f (representative of the structure)

on the relaxation process. $x = 1$ implies a temperature-controlled relaxation time with little influence from the structure, represented by T_f . ΔH is the activation energy for the enthalpy relaxation, which was shown to closely match the activation energy for shear viscosity (Moynihan et al., 1996).

3.3 Methodology

The Tramontana glasses are first characterized. Three types of experiments are performed: (a) accuracy test with DGG standard glass; (b) thermal annealing of remelted glasses from Cala di Tramontana, and (c) cooling rate estimates of natural glasses from Cala di Tramontana.

3.3.1 Sample Characterization

All measurements are performed at the Ludwig-Maximilians-Universität München (LMU), Germany. Material from two cylinders (TRM1C and TRM5G) is observed under the optical microscope for textural analysis and phenocryst identification. Material from cylinders (TRM1C, TRM1E, TRM4C, TRM5I, TRM5G and TRM6G) and a hand sample (TRM7) is measured by electron microprobe analysis (EMPA) using a 15 keV accelerating voltage and 5 nA beam current for the chemical composition of the groundmass glass and phenocrysts. A defocused electron beam of 10 μm and a counting time of 10 s are used to perform the measurements in order to prevent volatilization of the mobile Na and K elements contained in the groundmass glass. Standards are albite (Na, Si), periclase (Mg), orthoclase (Al, K), apatite (P), vanadinite (Cl), wollastonite (Ca), Cr_2O_3 (Cr), Fe_2O_3 (Fe), anhydrite (S), and ilmenite (Ti, Mn). The bulk chemical composition in major and trace elements is analyzed with a PANalytical X-ray fluorescence (XRF) spectrometer on samples TRM4C and remelted TRM9. The water content is estimated by measuring mass loss during the heating of glass samples up to 1000 °C using a Netzsch ® STA 449C instrument, that combines differential scanning calorimetry with thermogravimetry. The water content was estimated for the samples TRM1E and TRM4C. The viscosity of the remelted TRM9 sample is measured with a concentric cylinder viscometer (full-scale torque of 7.2×10^{-2} N m). Hand sample TRM9 is melted at 1300 °C, stirred during 15 hours to homogenize the melt and eliminate bubbles and crystals, and quenched in water. The resulting glass is crushed and remelted for the viscosity measurements. The glass obtained from the viscosity measurements is drilled and used to perform geochemical analyses and enthalpy relaxation geospeedometry.

3.3.2 Geospeedometry

Determining the natural cooling rate of a volcanic glass requires several heating and cooling cycles to obtain parameters necessary to model the natural C_p curve following the phenomenological Tool-Narayanaswamy-Moynihan approach (Moynihan et al., 1976b; Narayanaswamy, 1971; Tool, 1946) and using the rewritten equations from DeBolt et al. (1976) and the procedure outlined in Wilding et al. (1995).

The measurement procedure consists of first reheating the glass through the glass transition at a known rate, typically 10 K min^{-1} , to obtain the natural C_p curve. Each sample is heated at least $20 \text{ }^\circ\text{C}$ above the glass transition into the supercooled liquid (Höhne, 2003), which we consider sufficient to erase the “memory” of the glass. The glass is then cooled and reheated repeatedly at matching rates, using different rates (5, 7, 10, 15 and/or 20 K min^{-1}). A faster cooling rate leads to a higher $T_{g_{peak}}$ and a slower cooling rate, to a lower $T_{g_{peak}}$. Heating rates greater than 20 K min^{-1} are not recommended because the sample temperature may not be able to keep up with the increasing temperature of the furnace and a large thermal lag may result. A small amount of glass, preferably as a disk, also helps to minimize the thermal lag, to improve contact with the crucible and to avoid temperature gradients within the sample.

We measure the heat flux, via the electrical response (μV) of a thermocouple in contact with a platinum crucible that contains the sample, through a glass sample with a differential scanning calorimeter (DSC) as the glass is heated across the glass transition. We then calculate the isobaric heat capacity ($\Delta H/\Delta T$). Subsequently, we perform several heating/cooling cycles at known cooling and heating rates to characterize the material, which enables us to model the cooling rate of the glass. One cooling/heating cycle consists of cooling the melt at a constant rate from the supercooled liquid, where the melt is in a metastable equilibrium and C_p is \sim constant, to well below the glass transition. The resulting glass gets reheated at a rate equal to the previous cooling rate to at least $20 \text{ }^\circ\text{C}$ above the glass transition into the supercooled liquid range. This procedure is repeated at least four times for various rates, typically 5 or 7, 10, 15 and 20 K min^{-1} . The resulting heat capacity curves represent the *calibration* curves used to determine parameters that characterize the glasses in order to model the natural curve.

Samples are in the form of chips or discs $<1 \text{ mm}$ thick. The quality and reproducibility of the measurements is optimized when the samples are in the form of thin polished discs to assure uniform contact with the crucible and little temperature gradients within the sample during heating and cooling treatments. Each sample is heated in a Netzsch $\text{\textcircled{R}}$ DSC 404C Pegasus calorimeter from LMU Munich, Germany, under a small and constant flux of high purity argon 5.0 to avoid oxidation of the samples during measurements. We use an Arrhenian fit to obtain activation energy ΔH and the pre-exponential constant A from the plots of $\ln(q)$ vs $1/T_{g_{peak}}$ (Moynihan et al., 1974), assuming a linear relationship for a relatively short temperature range

of $T_{g_{peak}}$. The 4 calibration curves are used to find averaged ΔH and A , as well as x and β parameters. $T_{g_{onset}}$ is obtained following the method of Moynihan (1995). Once parameters ΔH , A , x and β are known, the natural cooling rate is estimated for the heat capacity curve obtained upon the first heating.

3.3.3 Accuracy Testing on DGG Standard Glass

DSC measurements are performed on ca. 28 mg of chips of the DGG standard Na-Ca-silicate glass (Table 3.1) rather than discs because the material is already in the form of chips. Three DGG standard glass samples cooled at known rates of 0.15, 1.5 and 15 K min⁻¹ are first reheated at 10 K min⁻¹ and we continue with the enthalpy relaxation geospeedometry procedure outlined above as if the cooling rate was unknown. Each sample is subsequently cooled and heated at 20, 15, 10 and 7 K min⁻¹ under the same experimental conditions. We compare the resulting modeled cooling rate to the known cooling rate and estimate the accuracy.

Table 3.1 Chemical composition of glass standard DGG.

| Oxides | Amount (wt %) |
|--------------------------------|------------------|
| SiO ₂ | 71.72 |
| Al ₂ O ₃ | 1.23 |
| Fe ₂ O ₃ | 0.191 |
| TiO ₂ | 0.137 |
| SO ₃ | 0.436 |
| CaO | 6.73 |
| MgO | 4.18 |
| Na ₂ O | 14.95 |
| K ₂ O | 0.338 |

3.3.4 Thermal Annealing Experiments

Thermal annealing is a process by which residual thermal stresses in a material are reduced or even dissipated. Far below the glass transition, in the glassy state, this will not occur. However, if the material is kept at a sufficiently high temperature for a given amount of time during a controlled cooling treatment, partial structural relaxation can occur (Scherer, 1991). A glass forming in a volcanic environment may be submitted to thermal annealing. The structural configuration of the glass may change and no longer be representative of the cooling rate at which the glass (then still melt) cooled across the glass transition. This annealing process would therefore induce significant error in calculated cooling rates when using the T_f concept in the

modeling of the heat capacity curves. The influence of thermal annealing on cooling rate estimates is tested here by first heating TRM9 remelted and homogenized glass samples of ca. 28 mg in the form of large chips above the glass transition and then including an annealing event during cooling. During the cooling treatment at 10 K min^{-1} , the samples are submitted to various isothermal holds: (a) $450 \text{ }^{\circ}\text{C}$ for 1 hour, TRM9-M3; (b) $450 \text{ }^{\circ}\text{C}$ for 1 day, TRM9-M5; (c) $500 \text{ }^{\circ}\text{C}$ for 1 hour, TRM9-M2 and (d) $500 \text{ }^{\circ}\text{C}$ for 1 day, TRM9-M4. The cooling rate is determined in each case, as well as in the “no annealing” case, using the enthalpy relaxation geospeedometry procedure. The first heating that follows the cooling with annealing event is performed at 10 K min^{-1} and the subsequent heating and cooling treatments are 20, 15, 10, and 7 K min^{-1} .

3.3.5 Measuring Natural Glasses from Pantelleria

Natural pantelleritic glass samples from Pantelleria are measured with the DSC and the resulting heat capacity curves are modeled to estimate natural cooling rates. The first heating is performed at 10 K min^{-1} and the subsequent heating and cooling treatments are 20, 15, 10, and 5 or 7 K min^{-1} . The glass samples are between ca. 63 mg and 84 mg and in the form of polished discs of ca. 6 mm diameter cut with a diamond wire saw from 6 mm diameter cylinders that were drilled from larger cores drilled in glassy layers of the deposit.

3.4 Geological Setting

The volcanic island of Pantelleria, type locality for the lithology pantellerite, is located within the NW-SE trending Sicily Channel submerged continental rift system between Sicily, Italy and Tunisia, North Africa (Figure 3.6). Volcanism is associated with trans-tensional tectonics. The landscape of the Island of Pantelleria is dominated by a central elevated complex formed predominantly by a trapdoor uplifted block, Montagna Grande, and Montagna Gibebe, inside the youngest of two nested calderas (Civetta et al., 1988; Mahood and Hildreth, 1983). The 6.3 x 9 km La Vecchia caldera is 114 ka old (Mahood and Hildreth, 1986) (Figure 3.7). The 6 km-diameter Cinque Denti caldera (Mahood and Hildreth, 1983), also named the Monastero caldera (Cornette et al., 1983), is 45-50 ka old (Mahood and Hildreth, 1986) and its collapse is associated with the eruption of the Green Tuff (Orsi and Sheridan, 1984). The last ca. 50 ka have been divided into six silicic eruptive cycles and the plinian eruption of the Green Tuff

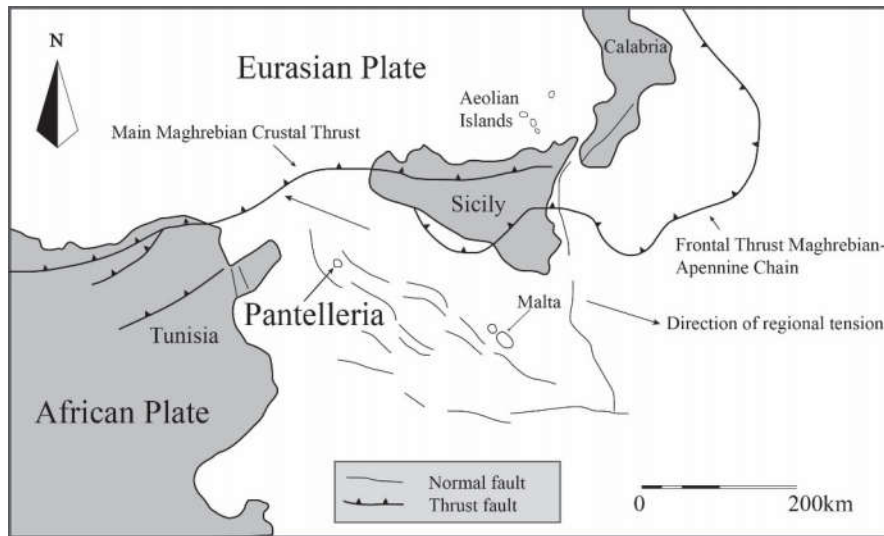


Figure 3.6 Tectonic setting of the island of Pantelleria, located within the Rift Zone of the Sicily Channel between Tunisia, Africa and Sicily, Italy. This region is characterized by tensional stresses oriented WNW-ESE, resulting in numerous normal faults and two major thrust faults. Map reproduced from Neave (2012) and based on Mahood and Hildreth (1986), Butler et al. (1992), Catalano et al. (2009).

represents the first cycle (Civetta et al., 1988). Most eruptions seem to have started predominantly explosively, most likely with a Strombolian eruptive style, to end effusively (Orsi et al., 1991). Based on ^{14}C dating of charcoal beneath a pumice fall deposit, a more precise dating method for young deposits than K-Ar dating, Mahood and Hildreth (1986) report an age of 3.03 ± 0.29 ka for the youngest deposit amongst the deposits that have been dated on Pantelleria.

Deposits are strongly peralkaline in composition, from pantellerite to trachyte, although minor alkali basalts are also found on the northwestern part of the island (Mahood and Hildreth, 1986). The name *pantellerite*, given by Förstner (1881, 1884), stands for silica-rich iron-rich strongly peralkaline obsidians and rhyolites. Despite high-silica content, strongly peralkaline magmas have low viscosities due to high Na and K content and potentially high eruptive temperatures. Temperatures between ca. 950 and 1025 °C (Carmichael, 1967; Wolff, 1980) have been suggested from Fe-Ti oxide geothermometry analyses based on the oxygen fugacity of the magnetite-ilmenite mineral assemblage. Nicholls and Carmichael (1969) suggest however much lower eruptive temperatures for pantellerites without Fe-Ti oxides. The typical phenocryst assemblage contained in iron-rich strongly peralkaline lavas from Pantelleria consists of anorthoclase, sodic clinopyroxene, aenigmatite, Fe-Ti oxides and quartz (Neave et al., 2012; White et al., 2005).

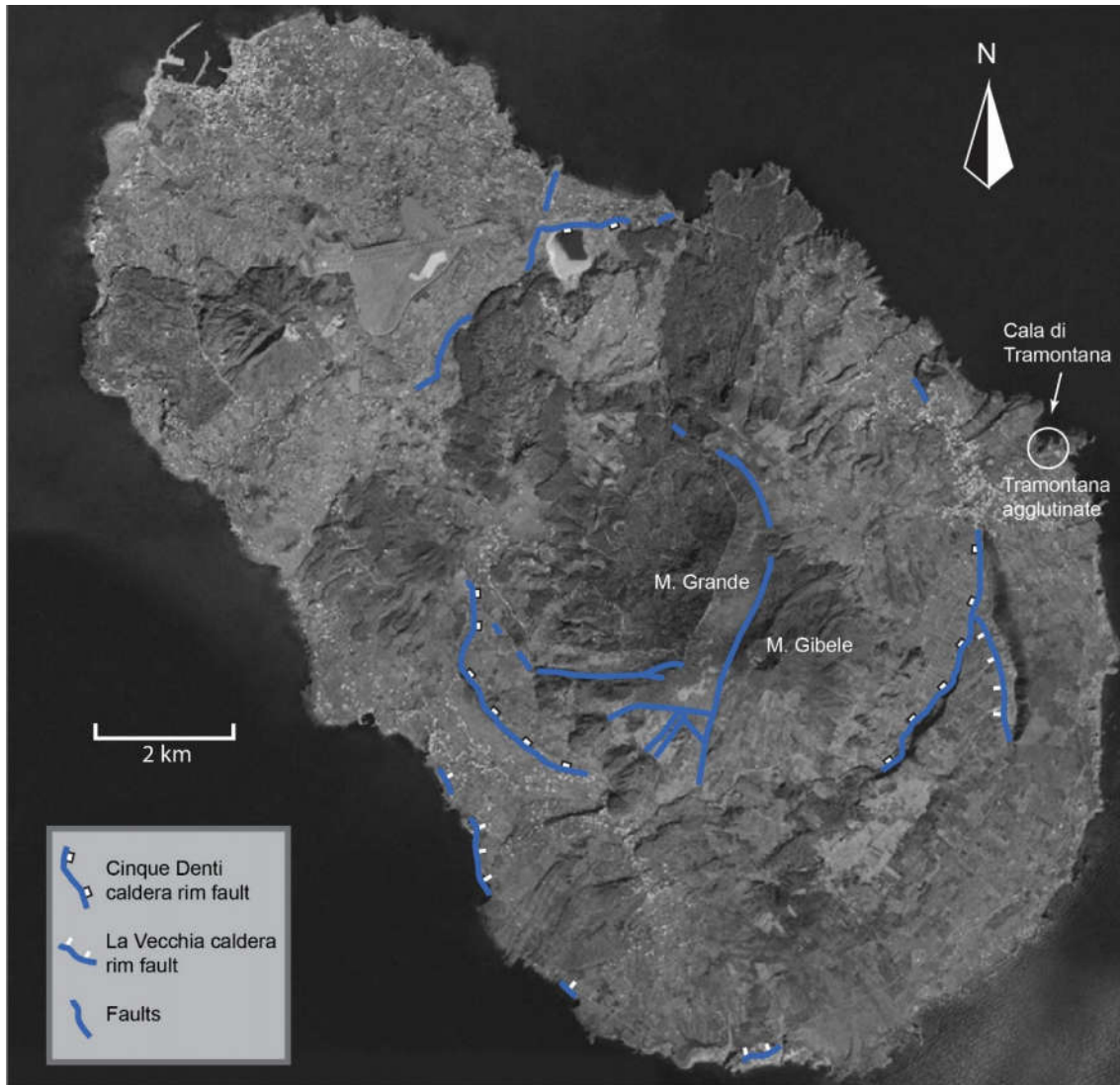


Figure 3.7 Aerial photo of Pantelleria with sketch of the Cinque Denti and La Vecchia caldera rim faults and additional faults. The Tramontana agglutinate is within the white circle and the Cala di Tramontana (Tramontana Bay) is identified with a white arrow. The Tramontana agglutinate is located next to and west of the Punta Tracino volcanoclastic deposit, which protrudes in the water.

3.5 The Tramontana Spatter-Fed Rheomorphic Deposit

This study focuses on the last erupted lobe of a pantelleritic eruptive sequence located along the coast of Cala di Tramontana, on the southeastern part of the island on the flank of the Cinque Denti-La Vecchia caldera complex. The ca. 6-7 m thick, 25-30 m wide and ca. 300 m long deposit on a 20° slope (Stevenson and Wilson, 1997) consists of multiple glassy layers of variable thickness sintered together and interfingered with reddish spatter clasts. The formation

of this deposit was the subject of a study by Stevenson and Wilson (1997) who suggested accumulation and welding of spatter from a fire-fountaining eruptive episode accompanied by rheomorphism for the mode of emplacement of the deposit. The inferred circular vent with a maximum radius of 5 m is a small hill with partly homogenized and glassy spatter deposits nearby. It is unambiguous that the deposit was originally formed by pyroclasts and was not coherent lava that flowed out of a large eruptive vent (Williams et al., 2014). A large section of the deposit consists of alternating scoria and glassy undulated and folded layers. The observable transition between scoria and glassy layers throughout a large section of the deposit supports the thesis that spatter agglutinated and flowed toward the sea. The glassy part of the deposit grades into an apparent coherent crystallized rhyolite lava flow at the front of the deposit by the water where flow ramps are visible and is estimated to represent ca. 60% of the flow (Stevenson and Wilson, 1997). The crystallized lava contains flow-oriented clinopyroxene, aenigmatite and feldspar crystals, and micromosaics of sanidine and quartz (Stevenson and Wilson, 1997). The age of the deposit is estimated at ca. 7.6 ka, an age determined by ^{14}C dating (Mahood and Hildreth, 1986) of charcoal found in a basal non-welded pumice fall unit at Punta Tracino, located directly next to the Cala di Tramontana agglutinate. Both are thought to have erupted relatively close in time due to the apparent absence of overlap of the two eruptive sequences (Stevenson and Wilson, 1997). We refer to the work of Stevenson and Wilson (1997) for a detailed description of the complete eruptive sequence comprising units 1 to 4, unit 4 being the agglutinate of interest in this study.

For the present study, 30 mm-diameter cylinders were drilled from six glassy flow layers accessible on the steep southeast side of unit 4 of the Cala di Tramontana eruptive sequence (Figure 3.8). The combination of glassy layers and scoria, the undulating and folding of glassy layers, and the short apparent length of each individual layer give the deposit an inhomogeneous and complex appearance. The six layers sampled are quite thin and have an approximate local thickness of 22 (TRM1), 25 (TRM3), 24 (TRM4), 25 (TRM5-bottom layer), 9 (TRM5-top layer 1), 17 (TRM5-top layer 2), and 18 to 26 (TRM6) cm. The two TRM5-top layers could in fact be one layer. We did not expect to obtain largely varying cooling rates in the interior of such thin layers, or intend to obtain a meaningful or realistic cooling profile for individual layers, given the complexity of each layer. We can expect at the most to obtain faster cooling rates from the bounding surfaces of the layers and slower cooling rates for the interior of the layers. Determining the top and bottom of the layers in the field was sometimes a challenge because

Figure 3.8 (next page) The Cala di Tramontana spatter-fed rheomorphic deposit. (a) Sampling sites 1, 3, 4, 5, 6, (b) Middle section of the deposit as seen in (a) showing the complex pattern of glassy layers and to the left is a section that has broken off from the deposit, (c) crystallized lava flow, (d) folded and fractured glassy layers mingled with reddish scoria, (e) close-up of a glassy layer, and (f) indication of shearing inside glassy, possibly folded, layer.



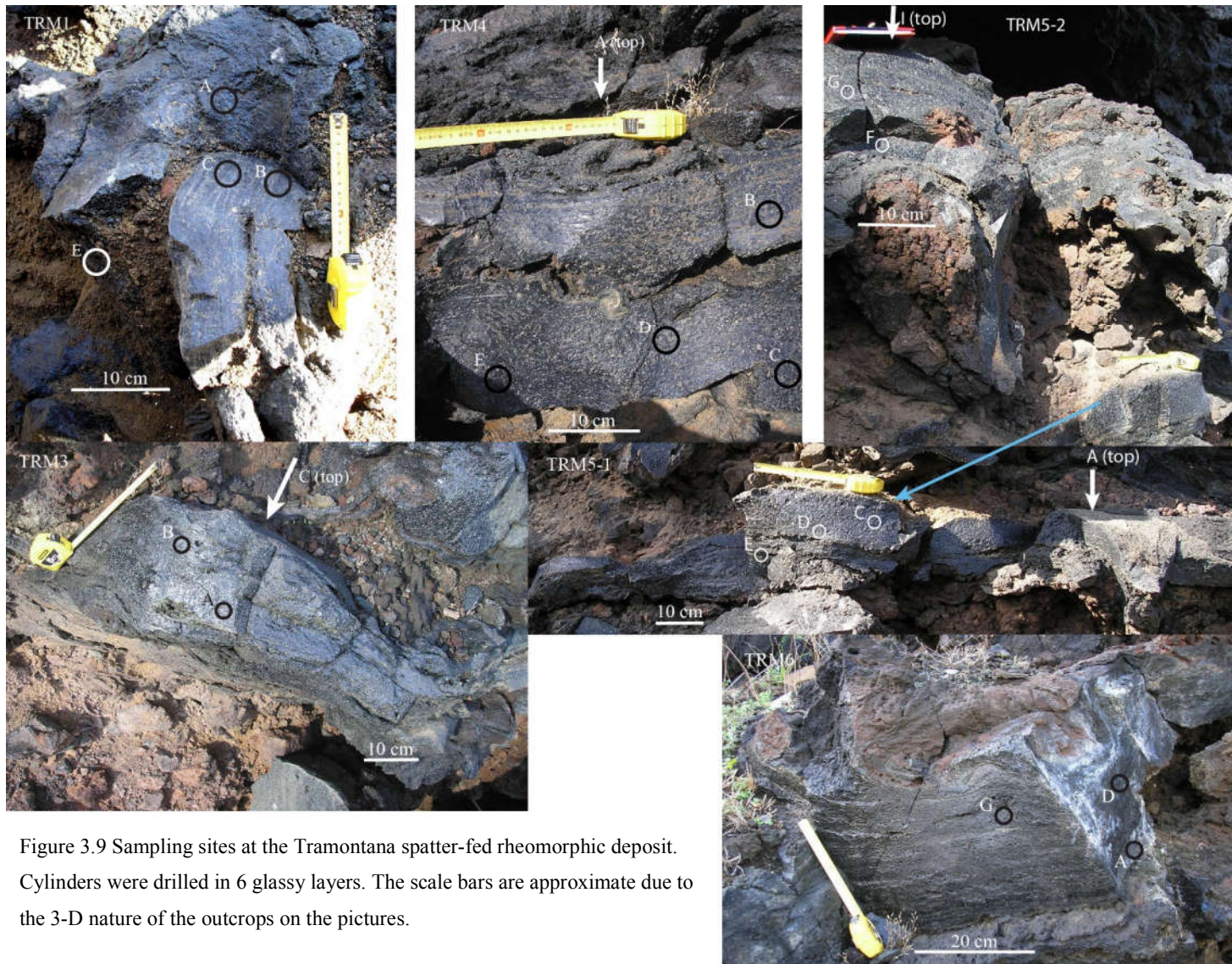


Figure 3.9 Sampling sites at the Tramontana spatter-fed rheomorphic deposit. Cylinders were drilled in 6 glassy layers. The scale bars are approximate due to the 3-D nature of the outcrops on the pictures.

some of the bounding surfaces were broken. We sampled the bounding surfaces when possible and throughout the layers to evaluate the homogeneity of the overall cooling and welding processes in the deposit.

3.6 Results

3.6.1 Groundmass Glass and Bulk Composition

The groundmass glass has a pantelleritic, or iron-rich peralkaline rhyolitic, composition with an average Alkalic Index ($\text{mol} [\text{Na}_2\text{O}+\text{K}_2\text{O}] / \text{mol} \text{Al}_2\text{O}_3$) of 2.15 for the average composition of the 6 samples analyzed (Table 3.2, Figure 3.10). However, looking at all measurements, we observe significant variations in the SiO_2 and Cl content. SiO_2 varies between 66.8 and 74.2 wt% and Cl varies between 0.54 and 1.16 wt%. Some of the highest Cl concentrations are found in glass inclusions inside anorthoclase phenocrysts (Figure 3.11e). The Cl content is overall high to very high relative to most rock compositions, in agreement with Lowenstern (1994).

The bulk composition of TRM4C and remelted TRM9 are also pantelleritic, with ca. 1% less SiO_2 and FeO total, and ca. 1% more Al_2O_3 in comparison to the average groundmass glass composition due to the phenocrysts. This confirms that we can apply the results of the thermal annealing experiments with remelted TRM9 to the glasses from the Tramontana deposit. Finally, our geochemical analyses confirm compositions published by Stevenson and Wilson (1997).

3.6.2 Mineral Phases and Textures

The glasses are mostly translucent microlite-poor glass but comprise also light to dark brown microlite-rich glass or fiamme, in which the proportion of acicular microlites, up to 40 μm in length, is much higher than in the microlite-poor glass. The fiamme are most likely scoria that have been incorporated in the glassy layers and have reached various degrees of welding. The fiamme are visible at the macroscopic scale as long light brown thin flow bands rather than as compacted and welded pyroclasts with still visible flaming endings, which is a common observation in rhyolitic welded and rheomorphic ignimbrites (Branney et al., 1992) and as such is indicative of the viscously deformable and high temperature nature of these deposits at deposition. All evidence of former pyroclasts has been obliterated. The microlite-rich glass shows in some cases a trachytic texture, and is found as irregular elongated regions that wrap around phenocrysts with undulated margins and flame-like endings (Figure 3.11b; 3.12a, e).

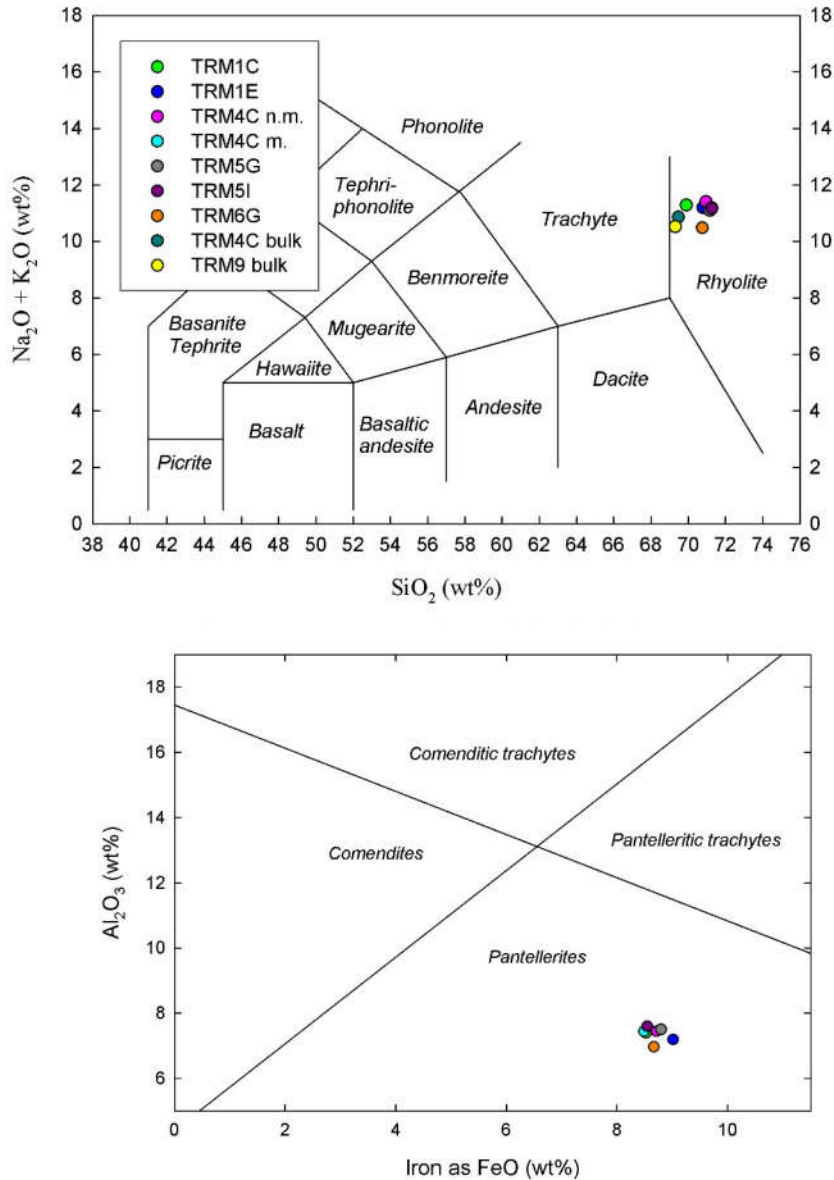


Figure 3.10 Groundmass glass and bulk compositions for all samples. Top diagram, total alkali and silica (TAS) diagram (Le Bas et al., 1986) and bottom diagram, classification of peralkaline rhyolites (MacDonald, 1974).

Thin section observations of boundaries between glassy ribbons/fiamme and microlite-poor glass show that the microlites are in great part flow-oriented (Figure 3.12b), which means that the melt was still viscous as they grew. Samples TRM1, obtained from the base of the deposit and relatively close to the coast, contain a large proportion (>30%) of fiamme in comparison to the other samples analyzed higher up in the stratigraphy and further away from the coast.

Table 3.2 Pantellerites from the Tramontana spatter-fed rheomorphic deposit: Major and trace element chemical compositions for whole rock (B) using XRF and groundmass glass (g) using EMPA. Sample TRM4C-M was heated in the DSC, TRM9 was remelted, and all other samples were not heated before the XRF or EMPA measurement. n.m. stands for not measured, and rem., for remelted. Rare earth elements are included in the total for samples 4C (B) and 9 rem.

| Samples | 4C (B, XRF) | 9 rem. (B, XRF) | 1C (g) | 1E (g) | 4C (g) | 4C-M (g) | 5G (g) | 5I (g) | 6G (g) |
|--------------------------------|----------------|--------------------|--------|--------|--------|----------|--------|--------|--------|
| n analyses | 1 | 1 | 75 | 20 | 14 | 28 | 10 | 18 | 4 |
| SiO ₂ (wt%) | 69.48 | 69.31 | 69.89 | 70.76 | 70.96 | 71.27 | 71.17 | 71.29 | 70.76 |
| Al ₂ O ₃ | 8.55 | 8.45 | 7.39 | 7.19 | 7.44 | 7.44 | 7.50 | 7.60 | 6.97 |
| FeO total | 7.86 | 7.78 | 8.52 | 9.02 | 8.71 | 8.49 | 8.80 | 8.55 | 8.67 |
| MnO | 0.28 | 0.28 | 0.34 | 0.37 | 0.36 | 0.35 | 0.33 | 0.33 | 0.31 |
| CaO | 0.38 | 0.38 | 0.33 | 0.32 | 0.36 | 0.34 | 0.40 | 0.40 | 0.31 |
| K ₂ O | 4.33 | 4.16 | 4.39 | 4.36 | 4.34 | 4.35 | 4.23 | 4.32 | 4.55 |
| Na ₂ O | 6.53 | 6.36 | 6.89 | 6.83 | 7.06 | 6.82 | 6.85 | 6.85 | 5.93 |
| TiO ₂ | 0.41 | 0.37 | 0.33 | 0.36 | 0.33 | 0.33 | 0.34 | 0.35 | 0.37 |
| P ₂ O ₅ | - | - | 0.03 | 0.02 | 0.02 | 0.03 | 0.04 | 0.03 | 0.03 |
| MgO | - | - | 0.04 | 0.03 | 0.04 | 0.04 | 0.03 | 0.04 | 0.04 |
| Cr ₂ O ₃ | n.m. | n.m. | 0.02 | 0.02 | 0.04 | 0.03 | 0.01 | 0.02 | n.m. |
| Cl | n.m. | n.m. | 0.86 | 0.89 | 0.87 | 0.86 | 0.86 | 0.74 | 0.78 |
| SO ₂ | n.m. | n.m. | 0.03 | 0.03 | 0.03 | 0.04 | 0.02 | 0.03 | n.m. |
| LOI | n.m. | n.m. | - | - | - | - | - | - | - |
| Total | 97.82 | 97.09 | 99.05 | 100.19 | 100.57 | 100.39 | 100.59 | 100.48 | 98.71 |
| H ₂ O | <0.05 | | | | | | | | |
| A.I. | 1.80 | 1.77 | 2.18 | 2.22 | 2.19 | 2.14 | 2.11 | 2.10 | 2.11 |

Rare Earth Elements (ppm)

| Samples | Ba | Co | Cr | Pb | Sr | Th | Zr | V | La | Ce | Nd | Ni | Zn | Ga | Rb | Y | Nb | U |
|------------|----|----|----|----|----|-----|------|---|-----|-----|-----|----|-----|----|-----|---|-----|----|
| 4C (B) | 54 | 7 | 12 | 26 | 16 | 125 | 1818 | 2 | 265 | 499 | 198 | 4 | 427 | 35 | 180 | - | 383 | 61 |
| 9 rem. (B) | 54 | 9 | 72 | 26 | 13 | 150 | 1842 | 4 | 277 | 519 | 209 | 26 | 428 | 33 | 181 | - | 388 | 72 |

In this study, we refer to the term phenocryst for all crystals $>100\ \mu\text{m}$ long and to the term microphenocryst for crystals between 40 and $100\ \mu\text{m}$ length. Microlites and nanolites are either acicular and $\leq 40\ \mu\text{m}$ in length, or stubby and $<10\ \mu\text{m}$ in length. Stubby crystals $>10\ \mu\text{m}$ are classified as microphenocrysts. The phenocryst content is estimated to ca. $10\ \text{vol}\%$ of the bulk volume and inhomogeneously distributed, and the microphenocryst content, between 1 and $3\ \text{vol}\%$ for the light areas and between 1 and $7\ \text{vol}\%$ for the darker areas. The darker areas are characterized by a high microlite/nanolite content difficult to estimate, but certainly $>50\ \text{vol}\%$. The light areas are poor in microlites/nanolites.

The lavas are porphyritic to glomeroporphyritic. Porosity is mostly very low with less than $1\ \text{vol}\%$, but reaches ca. $10\ \text{vol}\%$ slightly-deformed porosity in TRM5I where the pores are rounded and stretched and ca. $20\ \text{vol}\%$ highly-deformed porosity in TRM6G where the pores are very irregular in shape. This could be explained by either revesiculation, vesicle relaxation or differences in overburden pressure.

For each mineral phase identified, several phenocrysts are measured with the EMPA and several points are analyzed on each phenocryst. The absence of major-element compositional zoning suggests that the magma composition during crystal growth varied little. Anorthoclase (sodium-rich alkali feldspar), aenigmatite and Na-augite or aegirine-augite (clinopyroxene) are the three main mineral phases in order of abundance (Figure 3.11, Table 3.3), which is consistent with Neave et al. (2012) and White et al. (2009; 2005). During the preparation of the EMPA measurements, it is not always possible to dissociate crystals if two or three anorthoclase crystals are agglomerated. For this reason, we can say that at least 7 feldspar, 2 clinopyroxene and 3 Fe-oxide type-phenocrysts are measured. Disequilibrium textures such as embayed and resorbed crystals (Figure 3.11e, f) suggest that the phenocrysts are either xenocrysts that were mixed to the magma, that the phenocrysts experienced rapid magmatic decompression (Nelson and Montana, 1992) and/or reheating. Magma mixing is improbable because of the absence of reaction rims and significant geochemical variations in the magma. With the present data, we can conclude that the phenocrysts experienced a complex disequilibrium pressure-temperature-time path.

The microlite-poor and Fe -rich areas comprise the same microphenocryst assemblage: feldspar laths up to $80\ \mu\text{m}$ long and stubby quartz phenocrysts up to $20\ \mu\text{m}$ long present as single crystals or often as agglomerations of feldspar and quartz crystals. Fe-oxides and minor apatite and sulfide crystals are also found. Some feldspar laths have a swallow-tail texture, an indication of rapid growth. BSE images show the presence of porous glomerocrysts of microphenocrysts that contain a larger amount of feldspar and quartz microphenocrysts than the surrounding groundmass glass, as well as numerous disseminated Fe-oxides at the nm scale (Figure 3.12c). It remains to resolve the composition and origin of these glomerocrysts, which could be microporous hypidiomorphic enclaves. Enclaves have been reported in pantellerites from Pantelleria (Perugini et al., 2002). Some microlites and nanolites are not oriented with the

Table 3.3 Average chemical compositions of anorthoclase, aenigmatite and clinopyroxene phenocrysts based on a total of n major element analyses performed with the EMPA on several phenocrysts, with several points measured on any given phenocryst.

| | Alkali feldspar | Aenigmatite | Clinopyroxene |
|--------------------------------|-----------------|-------------|---------------|
| n analyses | 24 | 13 | 10 |
| SiO ₂ (wt%) | 67.93 | 41.01 | 48.87 |
| Al ₂ O ₃ | 18.13 | 0.47 | 0.11 |
| FeO total | 1.12 | 41.68 | 28.92 |
| MnO | 0.01 | 1.19 | 1.34 |
| CaO | 0.01 | 0.43 | 16.52 |
| K ₂ O | 6.18 | 0.00 | 0.01 |
| Na ₂ O | 7.45 | 7.05 | 2.57 |
| TiO ₂ | 0.01 | 8.87 | 0.30 |
| P ₂ O ₅ | 0.02 | 0.01 | 0.02 |
| MgO | 0.01 | 0.43 | 0.93 |
| Cr ₂ O ₃ | 0.03 | 0.03 | 0.03 |
| Cl | 0.00 | 0.00 | 0.01 |
| SO ₂ | 0.01 | 0.01 | 0.01 |
| Total | 100.91 | 101.18 | 99.63 |

flow direction nor with the trachytic texture of the microlite-rich areas. They consist of aenigmatite, feldspar, clinopyroxene and/or amphibole.

Sample TRM1C has a complex texture with many dark-brown undulating bands or ribbons, resorbed anorthoclase phenocrysts and large, in part elongated, black Fe-oxide blobs or bands along flow bands and the presence of green clinopyroxene or amphibole on the edges of aenigmatite crystals (Figure 3.12e). TRM1 is the sample with most disequilibrium textures. Based on 7 samples analyzed under the optical microscope and/or with the EMPA, the ratio of microlite-poor glass to fiamme most likely varies throughout the deposit.

Based on the textural analysis, the phenocrysts crystallized first, then the microphenocrysts, which show no sign of disequilibrium, and at last, the microlites/nanolites due to rapid cooling close to or at the surface.

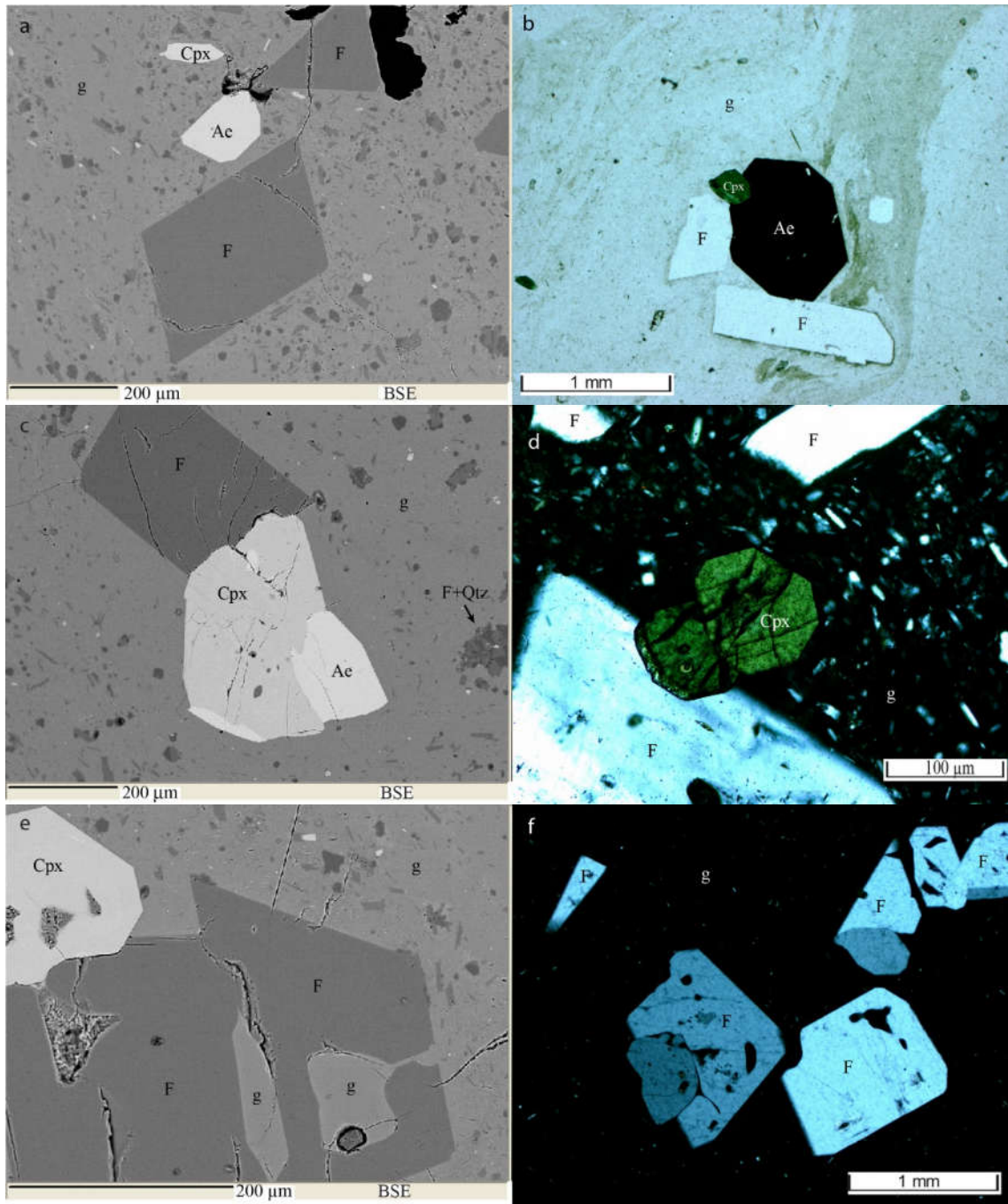
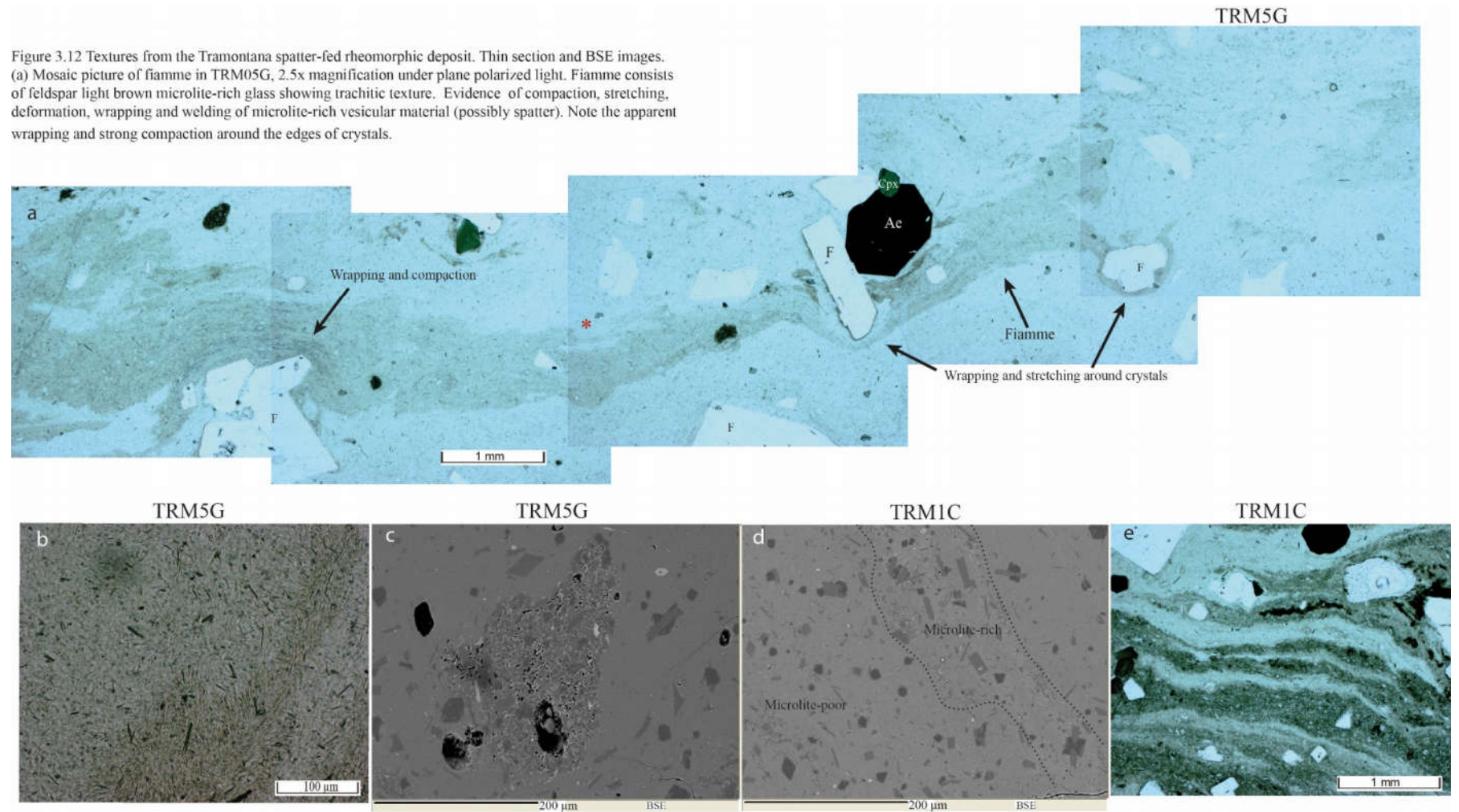


Figure 3.11 BSE images (a, c and e) and thin section images (b, d and f) of phenocrysts. (a) anorthoclase, aenigmatite and clinopyroxene phenocrysts (TRM1C), (b) cluster consisting of the 3 main mineral phases (TRM5G, xpl) (c) cluster of clinopyroxene, anorthoclase and aenigmatite (TRM4C-M) plus F+Qtz clot, (d) 2 euhedral clinopyroxene crystals, note the microphenocrysts in the groundmass (TRM1C, xpl) (e) anorthoclase phenocryst(s) with glass inclusions with some of the highest Cl concentrations measured in the Tramontana spatter-fed rheomorphic deposit (TRM1C), (f) partly resorbed anorthoclase phenocrysts (TRM5G, xpl). xpl is crossed polarized light, ppl is plane polarized light.



3.6.3 Sample Appearance and Composition before and after DSC

Measurements

To the naked eye, the measured glass discs do not change in appearance following measurements in the DSC. Partial bubbling of the surface occurs only in the instances where the sample is heated over 100 °C passed the glass transition. The mass change of glass samples after a series of heating and cooling treatments is within the error of the measurement, which points to a very small amount of magmatic molecular H₂O, estimated to be <0.05 wt%.

Scanning electron microscope (SEM) imaging of a TRM1E disc measured in the DSC reveals the crystallization of spherulites at the surface of the disc, indicating devitrification during the heating treatment (Figure 3.13). The linear elongated darker areas support the statement that the devitrification is only a surface process. Because devitrification is limited to the surface, the measurements are not significantly affected, except for possibly the last heat treatment of 5 or 7 K min⁻¹ where the sample stays longer in the glass transition and supercooled liquid fields. The resulting heat flux signal deviates slightly from the other measurements. Groundmass glass composition of a TRM4C sample before and after a geospeedometry procedure did not significantly change (Table 3.2).

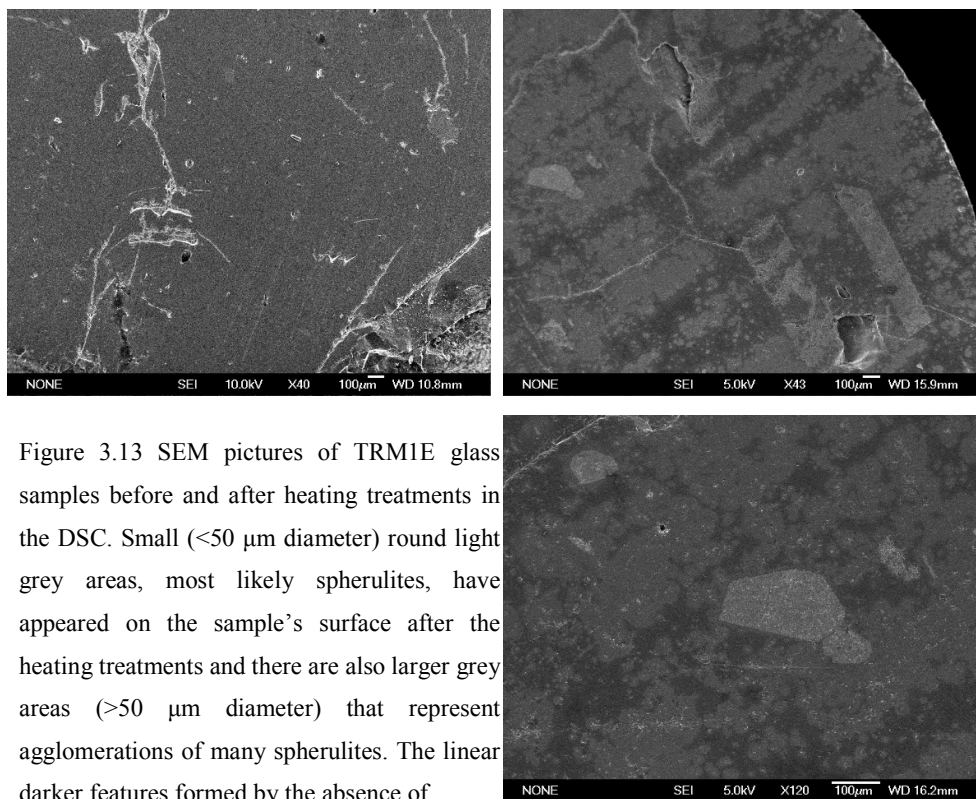


Figure 3.13 SEM pictures of TRM1E glass samples before and after heating treatments in the DSC. Small (<50 µm diameter) round light grey areas, most likely spherulites, have appeared on the sample's surface after the heating treatments and there are also larger grey areas (>50 µm diameter) that represent agglomerations of many spherulites. The linear darker features formed by the absence of spherulites in (b) coincide roughly with the striations formed by the polishing of the sample as seen in (a). The formation of spherulites occurs most likely at the sample's surface only and not further in the sample, affecting the DSC measurements in a minimal manner.

3.6.4 Accuracy of Cooling Rate Estimates

We use the TNM modeling approach on preconditioned DGG glasses and determine that the cooling rate estimates are systematically between 0.2 and 0.4 log unit lower than the actual experimental cooling rates (Figure 3.14). We note a decrease in this discrepancy with decreasing cooling rate. We test the idea of a possible thermal lag induced during heat flux measurements with the DSC. Hodge and Heslin (2010) suggested a correction, or deconvolution, of the C_p data once a thermal time constant has been measured. For this purpose, we program the DSC to heat a DGG glass sample at the fixed rate of 10 K min^{-1} , and heat the sample into the supercooled liquid field, which is a temperature window of stable C_p . Then we let the rate increase automatically to reach 20 K min^{-1} and the sample is further heated until the heat flux in the sample is stabilized. A time delay is observed in the response of the sample to the increase in heating rate from 10 to 20 K min^{-1} . This time delay may vary for different instrumental setups and is therefore possibly only applicable to our setup.

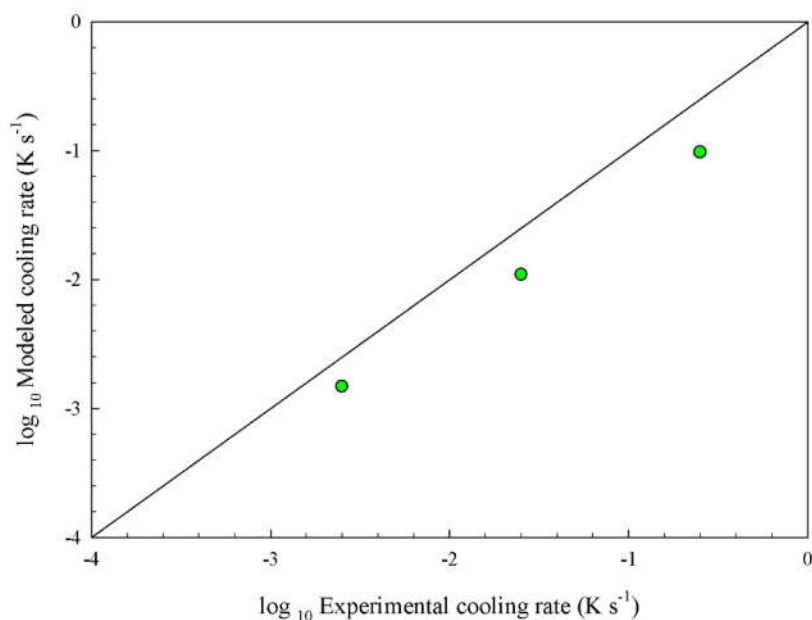


Figure 3.14 Accuracy testing of enthalpy relaxation geospeedometry on DGG glasses experimentally cooled at 0.15, 1.5 and 15 K min^{-1} . Calculated rate estimates are systematically between 0.2 and 0.4 log unit lower than the experimentally imposed rates. This discrepancy seems to decrease toward lower cooling rates. We could deduce that the accuracy of the cooling rate estimates improves for slowly-cooled glasses.

In order to measure the time delay, we plot heating rate and heat flux against time on the same graph and adjust the two vertical scales in order to align the two curves. The thermal lag

constant (τ_{ih}) is ~ 10 s (Figure 3.15). Accordingly, we correct T for the lag-induced temperature shift ΔT using equation (8) and C_p using equation (5) from Hodge and Heslin (2010)

$$T(t) = T_{lag}(t) - \tau_{ih} \cdot Q_h \quad (3)$$

$$C_p(t) = C_{p,lag}(t) + \tau_{ih} \cdot Q_h \left(\frac{dC_{p,lag}}{dT} \right) + \text{baseline shift} \quad (4)$$

Q_h represents the heating rate. The corrected, or deconvoluted, T and C_p data are used to model the DGG C_p data again. ΔH and A are obtained from plotting the deconvoluted data as described above. Unfortunately, deconvolution results in cooling rate estimates even further away from the experimental values. Moreover, the ΔH and A values become unrealistic. We suspect that the deconvolution of our data is in fact unnecessary. This could be due to the fact that the glasses used in this study have significantly different thermal properties than the polycarbonate polymer used in Hodge and Heslin (2010) in that the glass transition is up to ca. 75 °C wide instead of 10 °C wide, and above 500 °C instead of below 200 °C. In our study, the DSC, equipped with a Sample Temperature Controller (S.T.C.), is most likely capable of compensating for the delay before the glass transition is reached. There are still other probable causes for the discrepancy of the calculated cooling rates: (1) the cooling rate experienced by the sample is not equal to the programmed cooling rate or (2) the model is not fully representative of the processes involved in enthalpy relaxation of peralkaline silicate glasses. Nevertheless, the modeled cooling rates are close to the experimental cooling rates and we can apply an average correction factor of +0.3 log unit to the calculated cooling rates.

3.6.5 Influence of Thermal Annealing on Cooling Rate Estimates

Thermal annealing for a period of 24 hours at 450 and 500 °C results in a significant reduction of the estimated cooling rate (Figure 3.16). The cooling rate estimates are reduced by at least 1 to 3 orders of magnitude. The uncertainty in the magnitude of the rate reduction stems from modeling difficulties due to noise and irregularities in the C_p curves and reflects the difficulty of working with remelted natural glasses. The shape of the glass chips may have also influenced the homogeneity of the annealing effect in the glasses due to variability in the sample's contact with the crucible. A second experiment performed at 450 °C with 24-hour thermal annealing was unsuccessful due to strongly irregular C_p curves. The effect of thermal annealing is not observed when thermal annealing is restricted to one hour. Figure 3.16 provides an additional estimate of the accuracy of the TNM modeling approach with the results from the “no annealing” experiments. These two modeled cooling rates are ca. 0.2 log unit and ca. 0.7 log unit away from the experimental value of 10 K min⁻¹ (0.17 K s⁻¹).

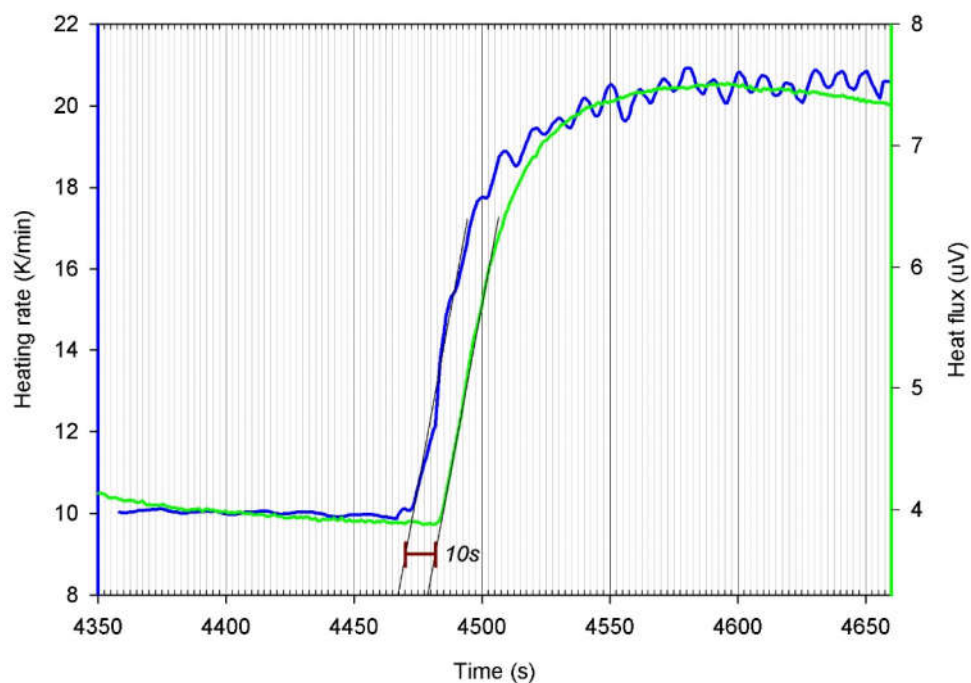


Figure 3.15 Thermal lag constant for measurements performed with the DSC 404C Pegasus from Netzsch at the LMU Munich. The heating rate is calculated from the temperature and time data file. The thermal lag constant is measured to be ~ 10 s. The magnitude of this constant may vary due to sample mass and shape. The shape of the sample influences its contact with the crucible bottom surface.

The thermal annealing experiments at 450 and 500 °C where the sample remains at the given temperatures for one hour only show no significant reduction of the estimated cooling rates. However, where the samples remained at these same temperatures for 1 day, the estimated cooling rates are reduced by up to 3 orders of magnitude.

3.6.6 Calorimetry of Pantellerites

Figure 3.17 attests to the reproducibility of the DSC measurements. Sample TRM6G was heated a first time at 10 K min^{-1} and resulted in a high overshoot, meaning that the previous cooling rate was significantly lower than 10 K min^{-1} . The 4 subsequent cooling and heating treatments at 10 K min^{-1} showed very little variation in the C_p traces, indicating that spherulite crystallization is not significant. A compilation of all natural C_p curves measured for the Tramontana volcanoclastic deposit is shown on Figure 3.18.

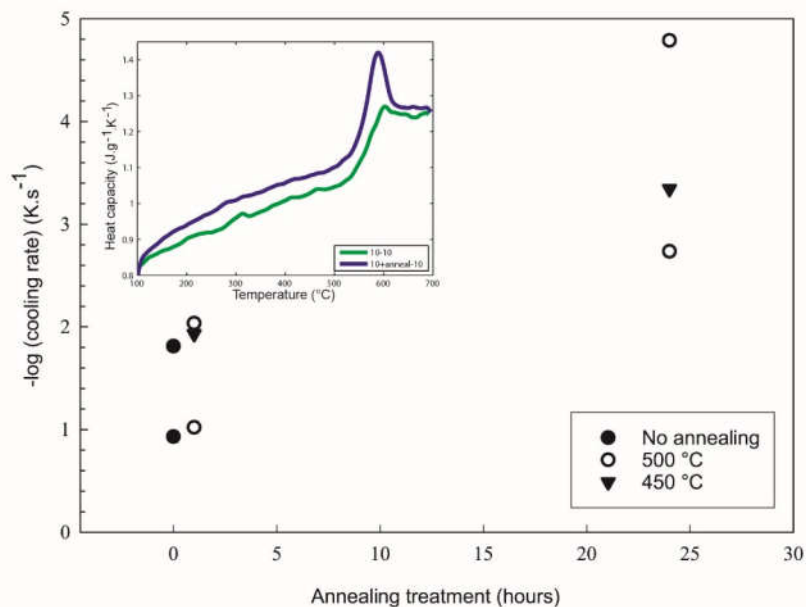


Figure 3.16 Comparison of estimated cooling rates for remelted and homogenized pantelleritic glasses cooled at 10 K min^{-1} without thermal annealing and with thermal annealing at 450 and 500 °C for 1 hour or 1 day.

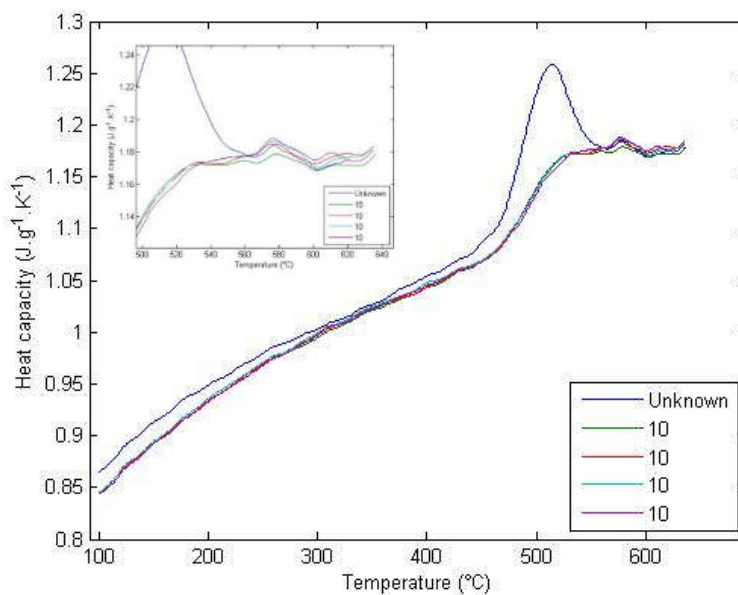


Figure 3.17 Heat capacity curves for 5 repeated heating treatments of TRM6G following cooling treatment at 10 K min^{-1} . The curve with the large overshoot is obtained from the first heating and the preceding cooling rate is unknown. The C_p curves lie within $\sim 0.01 \text{ J g}^{-1} \text{ K}^{-1}$ and show the effective reproducibility of the measurements. The C_p of the second peak increases slightly with each further heating from the 2nd heating to the 5th heating. A $\sim 0.01 \text{ J g}^{-1} \text{ K}^{-1}$ increase represents $\sim 1\%$ increase, which is actually within the uncertainty of the measurement.

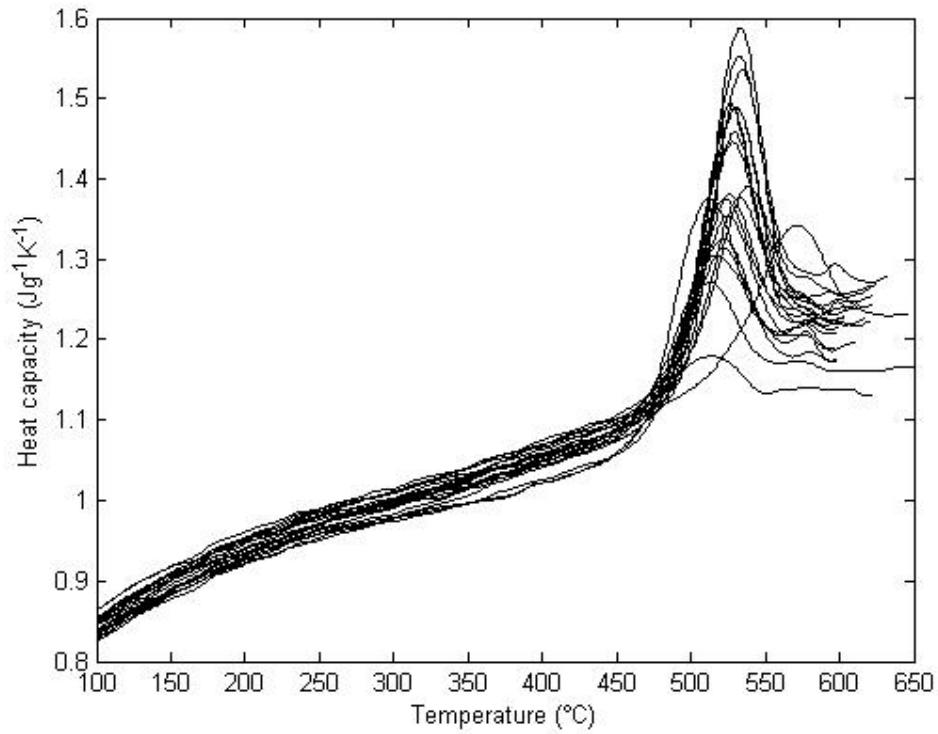


Figure 3.18 Compilation of heat capacity traces for all 21 Tramontana glass samples measured upon a first reheating at 10 K min^{-1} . The previous cooling rate is unknown. The Tramontana material consists of natural glass measured without any heat treatments above $100 \text{ }^\circ\text{C}$ prior to the DSC measurements.

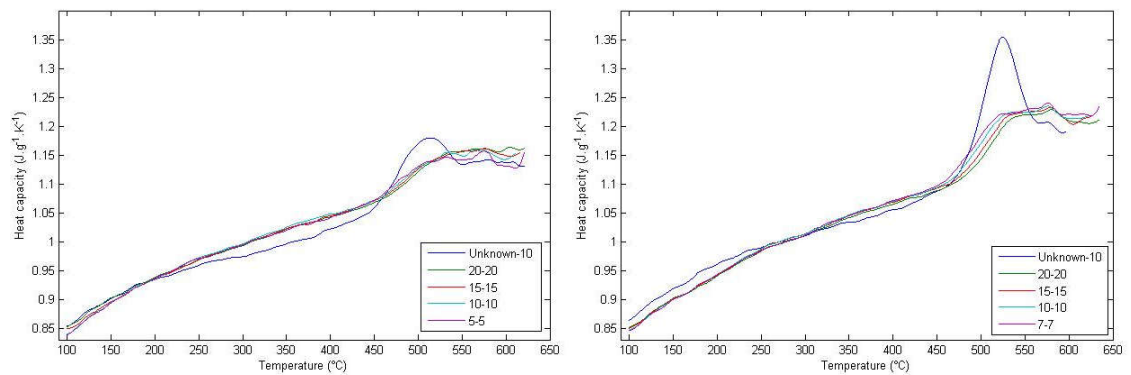


Figure 3.19 Small depression in natural C_p curves (a) TRM6D and (b) TRM3B in comparison to the calibration curves. Based on annealing experiments of hyperquenched basaltic glass and subsequent reheating (Ya et al., 2008; Yue et al., 2002b), the large trough characteristic of hyperquenched glasses is eliminated up to the reheating temperature. Because the depressions in the Tramontana curves are small but over a large T interval, the idea of partial annealing of a rapidly cooled glass is discarded.

$T_{g_{peak}}$ values range from 512 to 571 °C and limiting T_f , from 306 to 452 °C. All natural C_p curves but 2 show a high overshoot in the glass transition, usually corresponding to slowly-cooled glasses. The glass transition peak for TRM5I is especially high in temperature but with a smaller overshoot, relative to the other samples. TRM6D has the glass transition peak associated with the lowest heat capacity, smallest overshoot and lowest heat capacity in the supercooled liquid field. TRM6D has a C_p depression below the glass transition interval in comparison to the calibration curves. Several other samples have very small depressions (Figure 3.18).

All heat capacity curves have upon initial heating a second peak with a lesser height than the first peak (Figures 3.17, 3.20). This second peak is located 41 to 64 °C after $T_{g_{peak}}$ and is further observed during all subsequent heat treatments, but stays interestingly between 572 and 581 °C for the calibration curves. For some samples, it is not possible to identify the second peak due to very irregular and noisy curves at $T > T_{g_{peak}}$. In the case of TRM5A and 5I, the T range of $T_{g_{peak}}$ is located in the temperature range of the second peak observed in the other samples and the determination of $T_{g_{peak}}$ 2nd peak is ambiguous. The second peak is most likely associated with the endothermic phase transformation of α -quartz to β -quartz, which is known to occur at ca. 573 °C (e.g., Heaney, 1994; Wahl, 1961) and was also mentioned in a study of melt inclusions in pantellerites from Pantelleria (Lowenstern, 1994).

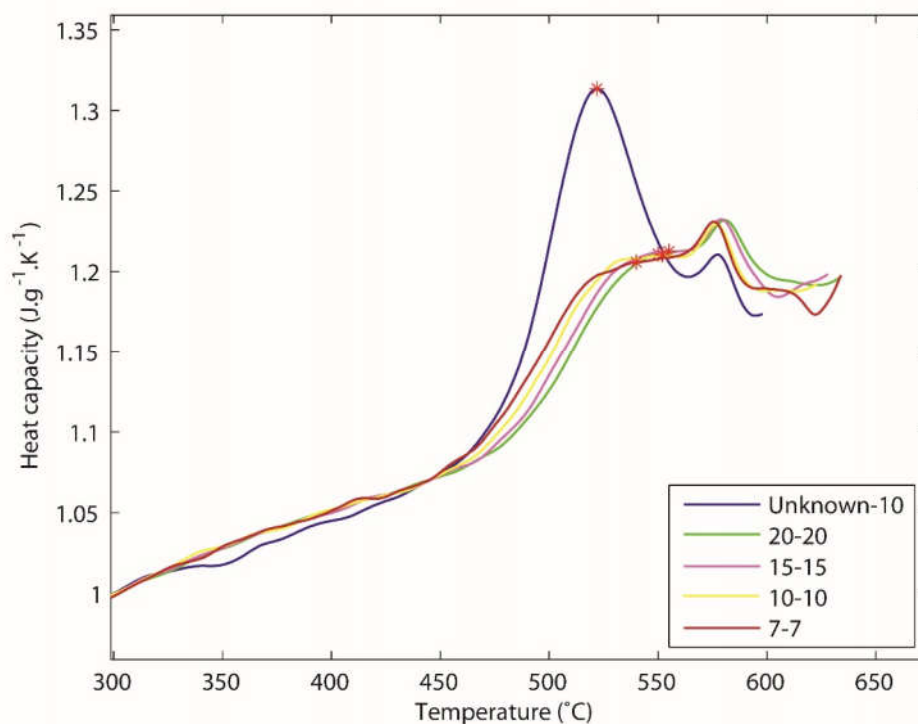


Figure 3.20 Heat capacity curves for TRM5E demonstrating the presence of a second peak, after the peak associated with the glass transition (red stars). This second peak occurs between 572 °C and 581 °C on all curves. TRM5E is a very clear example. The legend refers to cooling and heating rates in $K\ min^{-1}$.

We have indeed identified quartz microphenocrysts in all analyzed samples. This transformation is usually not easily detected because it occurs below the peak glass transition temperature for most igneous rocks containing various amounts of glass and because most studies prone aphyric glasses. However, because pantellerites contain crystals, in part quartz crystals, and have such low peak glass transition temperatures, the second peak due to α - to β -quartz transformation could be easily detected in or close to the supercooled liquid field where the C_p curve is stable (slope ~ 0).

Although the α - to β -quartz transformation most likely is the main cause, variations in iron oxidation states of the melt phase in the pantellerites studied here may be partly responsible for the presence of second or even multiple C_p peaks (Bouhifd et al., 2004; Kremers et al., 2012; Liebske et al., 2003a). The iron oxidation state of compositionally homogeneous magma may vary depending on the extent of magma exposure to air during an eruption. The mingling of both more reduced versus more oxidized magma may occur due to variable residence times at shallow levels in the conduit (Kremers et al., 2012; Lautze and Houghton, 2005).

The peak areas of the calibration curves from sample TRM5E were strongly affected by this second peak and rendered the modeling very challenging. The heat capacity associated with the peaks is much lower than the heat capacity associated with the second peaks. The only sample for which the modeling is little affected by the second C_p peak is TRM5I because the main C_p peak occurs around the same temperature at which the second C_p peak occurs.

3.6.7 Modeling Parameters and Cooling Rates

The modeled cooling rates range from 10^{-7} to 10^{-3} K s⁻¹, which correspond respectively to 3 K year⁻¹ and 3.6 K hour⁻¹ (Table 3.4). A rate of 10^{-7} K s⁻¹ is suspicious, especially for a deposit as small as the Tramontana volcaniclastic deposit. Cooling rates for the TRM4 24 cm-thick glassy layer span 4 orders of magnitude, which raises questions that will be discussed in section 7 (Figure 3.23). There is a clear correlation between limiting T_f and cooling rate. The slowest cooling rate corresponds to the lowest limiting T_f and the fastest cooling rates correspond to some of the highest limiting T_f . TRM5I, with one of the highest observed porosities with ca. 10%, is the most prominent outlier with a limiting T_f of 452 °C. The modeled cooling rate for TRM5I has a significant uncertainty due to the unsatisfactory fit with a sum of squared errors (SSE) of 110 K² min⁻². The fit of the peak height is correct, but the modeled width is too narrow.

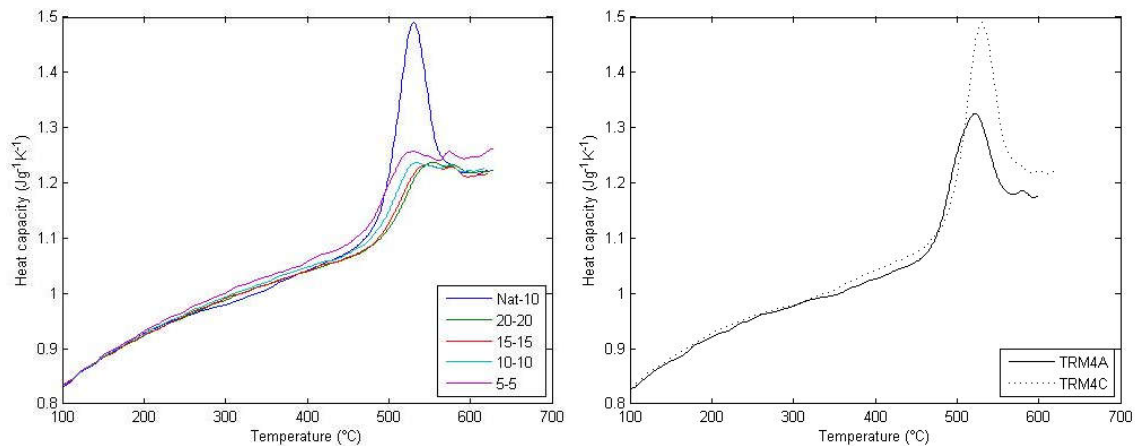


Figure 3.21 (a) TRM4C heat capacity curves for all 5 consecutive heating treatments. Note the large overshoot of the natural curve in comparison to the calibration curves. (b) Heat capacity curves produced during the first heating of samples TRM4A and TRM4C associated with relatively rapid (10^{-1} K min^{-1} , solid line) and slow (10^{-5} K min^{-1} , dotted line) cooling rate estimates.

The presence of a second peak due to the phase transformation of α - to β -quartz complicates the modeling for most samples. A minimum supercooled liquid temperature must be determined for each curve in order to constrain the glass transition interval to be modeled. The second peak obscures the supercooled liquid field in that a temperature above the minimum T_{sl} has to be selected, resulting in wider peaks for the normalized C_p calibration curves. For TRM6, all three samples were heated up to the second peak, but not beyond, meaning that T_{sl} is not known. T_{sl} selected in this case is the T corresponding to a minimum C_p between the first peak and the second peak. The calculated cooling rate estimates have a greater error. All other samples were heated past the 2nd peak and we were able to obtain a reasonably good fit by putting only half of the weight on the SSE for the region where the 2nd peak appeared (Figure 3.22).

Modeling parameters are compared to the parameters found in the literature for a similar modeling method to estimate cooling rates of pantellerites, calc-alkaline rhyolites, phonolites and basalts (Figure 3.24). Different compositions and thermal annealing influence the modeling parameters. The average ΔH is consistent with the ΔH obtained in previous studies from pantelleritic spatter-fed flows collected on Mayor Island (Gottsmann and Dingwell, 2002) and in the Tramontana spatter-fed rheomorphic deposit (311 kJ mol^{-1} , Stevenson et al., (1997)).

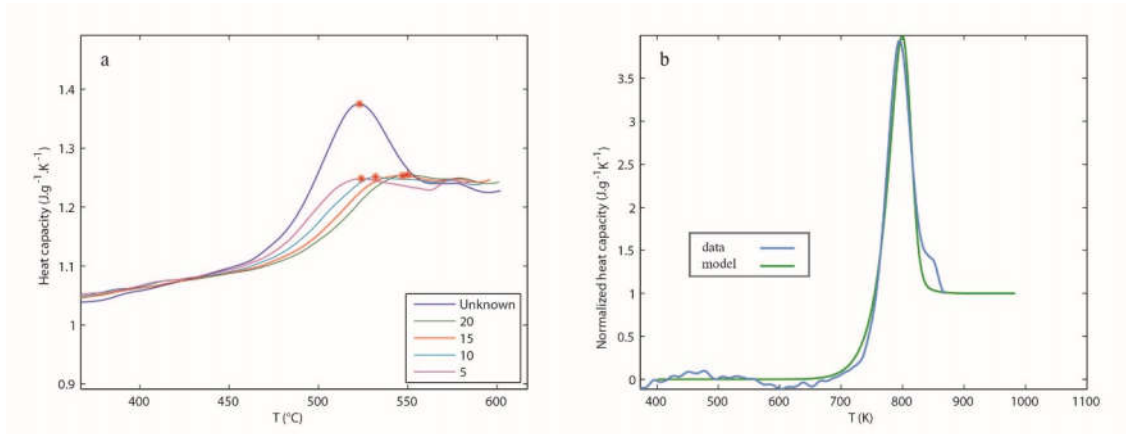


Figure 3.22 Modeling of TRM5G C_p curves (a) Smoothed C_p curves for the first heating and 4 subsequent heating treatments for the 4 calibration curves at 10, 20, 15, 10 and 5 K min^{-1} . The red star identifies $T_{g_{peak}}$. (b) Modeling best-fit for the natural C_p curve (blue) after the first heating at 10 K min^{-1} . The C_p was normalized to 1 for comparison with the evolution of $\Delta T_f/\Delta T$. The best-fit parameters are $\Delta H = 268 \text{ kJ mol}^{-1}$, $A = 1.3\text{e-}16 \text{ s}$, $x = 0.89$, $\beta = 0.73$ and weighted SSE = $5.5 \text{ K}^2 \text{ min}^{-2}$.

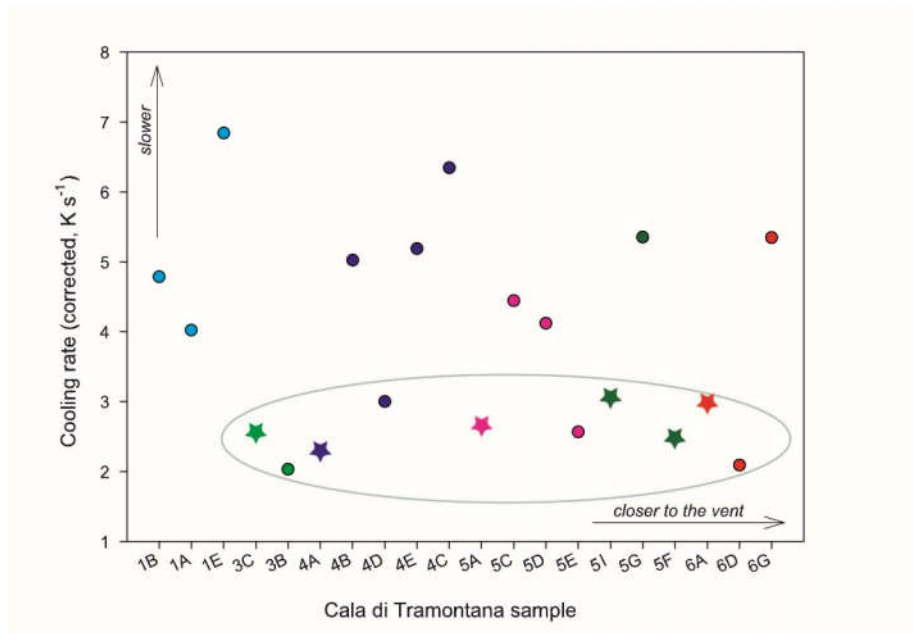


Figure 3.23 Modeled cooling rates for glass samples collected within Unit 4 of the Tramontana volcaniclastic deposit. The rates have been corrected (+ 0.3 log unit), based on the accuracy testing on preconditioned DGG glasses. Each sampled glassy layer is identified with a different colour. The circled rates are the fastest cooling rates obtained for this deposit. The stars represent glass that was sampled at apparent bounding surfaces.

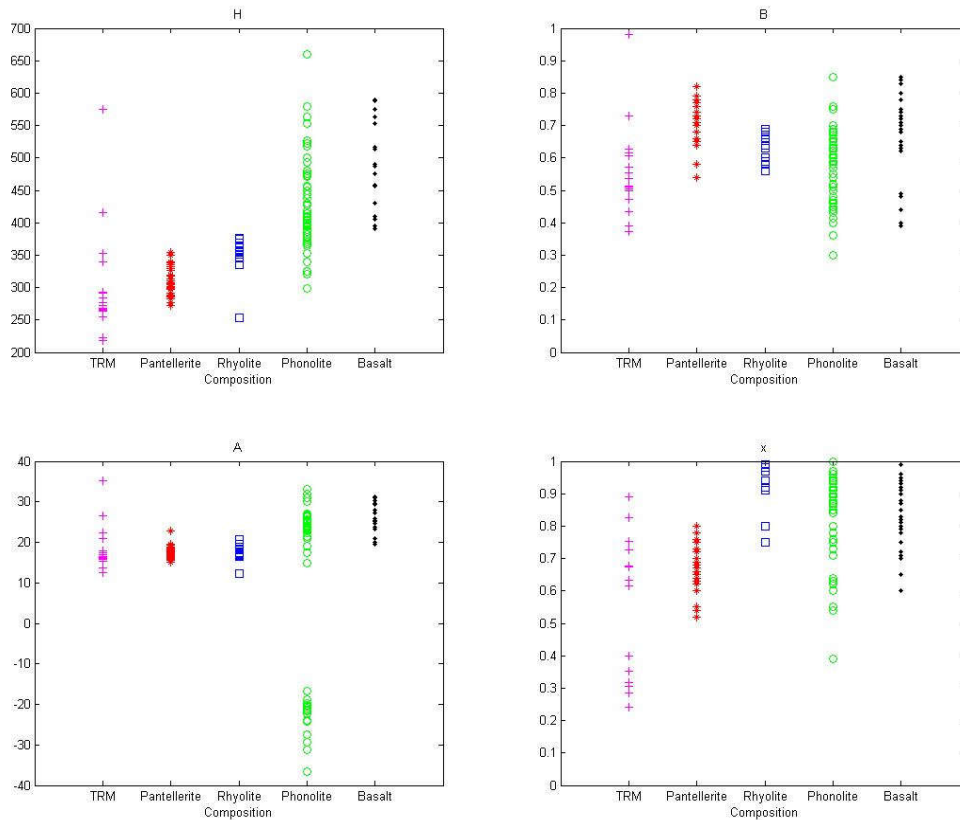


Figure 3.24 Comparison of modeling parameters x , β , A and ΔH for Tramontana pantellerites, pantellerites from Mayor Island, calc-alkaline rhyolites from Lipari, phonolites from Tenerife and basalts from Hawaii.

3.7 Discussion

3.7.1 Range of Peak Glass Transition Temperatures

There are a number of possibilities to explain the 59 °C range in peak glass transition temperatures observed in the TRM samples. (1) Inter-sample variations in cooling rates at which the glass was formed where glasses with a higher cooling rate will have higher values of $T_{g_{peak}}$. (2) Variations in the oxidation state of the melt as it undergoes the glass transition may produce a recorded $T_{g_{peak}}$ range of up to, or even greater than, 60 °C (Kremers et al., 2012). (3) The variability in Cl content seems relatively small in the samples analyzed here (ca. 0.83 ± 0.3 wt%), but in fact small variations in Cl content could have an effect on the viscosity of a melt, and therefore, on the peak glass transition temperatures. The effect is still uncertain because studies have not yet experimented with melts of pantelleritic composition (e.g., Baasner et al., 2013; Dingwell and Hess, 1998).

Table 3.4 Uncorrected cooling rates, peak glass transition temperatures, fictive temperatures and modeling parameters.

| Sample | Cooling rate (K s ⁻¹) | T _{g onset} (°C) | T _{g peak} (°C) | T _{sl} (°C) | T _f (°C) | ΔH (kJ mol ⁻¹) | x | β | A |
|----------|--------------------------------------|---------------------------|--------------------------|----------------------|---------------------|-------------------------------|------|------|----------|
| TRM01B | 8.18e-06 | 483 | 532 | 602 | 339 | 292637 | 0.61 | 0.51 | 1.01E-18 |
| TRM01E | 7.23e-08 | 487 | 534 | 604 | 306 | 283566 | 0.83 | 0.61 | 1.23E-17 |
| TRM01A | 4.737e-05 | 483 | 527 | 588 | 349 | 254955 | 0.68 | 0.62 | 4.70E-16 |
| TRM05G | 2.22e-06 | 475 | 523 | 595 | 336 | 268172 | 0.89 | 0.73 | 1.30E-16 |
| TRM05C | 1.80e-05 | 480 | 528 | 593 | 353 | 272785 | 0.75 | 0.63 | 4.54E-17 |
| TRM05D | 3.79e-05 | 485 | 533 | 592 | 349 | 265055 | 0.63 | 0.56 | 1.08E-16 |
| TRM05i | 0.000433 | 507 | 571 | 632 | 452 | 574569 | 0.32 | 0.37 | 5.42E-36 |
| TRM05E | 0.000134 | 474 | 522 | 595 | 362 | 266164 | 0.35 | 0.50 | 2.64E-17 |
| TRM05A | 0.00109 | 486 | 538 | 596 | 402 | 340157 | 0.40 | 0.47 | 1.04E-21 |
| TRM05F | 0.00166 | 478 | 526 | 593 | 388 | 352745 | 0.29 | 0.44 | 4.10E-23 |
| TRM04A | 0.00254 | 469 | 522 | 594 | 345 | 223242 | 0.30 | 0.50 | 1.97E-14 |
| TRM04B | 4.759e-06 | 467 | 512 | 595 | 313 | 276895 | 0.61 | 0.51 | 3.39E-18 |
| TRM04C | 2.26e-07 | 488 | 530 | 611 | 309 | 291103 | 0.73 | 0.50 | 1.66E-18 |
| TRM04D | 0.000499 | 480 | 530 | 577 | 385 | 217897 | 0.83 | 0.98 | 3.81E-13 |
| TRM04E | 3.22e-06 | 490 | 533 | 620 | 322 | 267445 | 0.67 | 0.54 | 6.46E-17 |
| TRM03B | 0.00462 | 477 | 525 | 568 | 393 | 264308 | 0.40 | 0.57 | 7.44E-17 |
| TRM03C | 0.00138 | 483 | 529 | 594 | 396 | 415617 | 0.24 | 0.39 | 2.56E-27 |
| TRM06G | 2.26e-06 | 458 | 513 | 561 | 409 | 536999 | 1 | 0.46 | 7.18E-35 |
| TRM06A_2 | 0.000521 | 465 | 517 | 558 | 404 | 255686 | 1 | 0.90 | 9.33E-16 |
| TRM6D | 0.00404 | 440 | 514 | 550 | 404 | 196369 | 1 | 0.90 | 5.92E-12 |

3.7.2 Interpreting the Cooling Rate Profiles

The deposit is macroscopically inhomogeneous such that glassy and scoriaceous layers are interfingered, and these layers are additionally folded and fractured, revealing an apparent complex emplacement history. The distribution of cooling rates calculated here using samples from within single layers or among the sampled sites does not produce any systematic cooling profiles with simple interpretations. Part of the challenge results from the fact that layer boundaries cannot reliably be identified because of folding, fracturing and welding of layers (Williams et al., 2014). It is interesting that, even at the scale of ≤ 25 cm, glasses were submitted to different conditions, leading to a wide range of apparent cooling rates. The lowest modeled cooling rate at 10^{-7} K s⁻¹ equates to an unprecedentedly low cooling rate of ca. 0.009 K day⁻¹. We therefore propose that (1) the glassy layers throughout the deposit experienced thermal annealing to various degrees and the intensity of the annealing possibly varied greatly even within a single layer, and (2) cooling inside layers and throughout the deposit was highly heterogeneous. It remains to elucidate the conditions in which thermal annealing and cooling occurred. These results do generally reveal that the cooling rate of glasses from the bounding surfaces of the glassy layers or ribbons was faster than in the bulk of the same layers with a minimum of almost 10^{-2} K s⁻¹, or equivalently, ca. 36 K hour⁻¹. The highest cooling rate estimate represents a lower limit on the highest cooling rate of the deposit. The glasses with the highest cooling rates have most likely also experienced a certain amount of thermal annealing.

3.7.3 Emplacement of the Tramontana Spatter-Fed Rheomorphic

Flow

A vigorous lava-fountaining eruption most likely produced the Tramontana volcanoclastic deposit, as proposed by Stevenson and Wilson (1997). In similar basaltic eruptions (Head and Wilson, 1989; Sanchez et al., 2012; Sanchez et al., 2014; Sumner, 1998), the lava fountain has a zoned structure such that the outer part of the fountain often produces more-rapidly cooled clasts. A scoria cone around the vent forms with a lava pond inside. The interior produces very hot clastic spatter, which may form a lava pond as it lands inside the cone and flows back toward the vent. The hot spatter may also accumulate on the rim or outer part of the scoria cone and form rootless lava flows.

The Tramontana agglutinates may have formed by similar mechanisms of hot deposition, viscous agglutination and density-driven rheomorphic down-slope flow. Degassing of the magma prior to eruption in addition to a low exsolved gas fraction driving fountaining promotes high accumulation rates on a relatively small area (Head and Wilson, 1989) and thereby, heat

retention. A lava fountain inclined toward Tramontana Bay concentrates the accumulation of the material in a more restricted area and lava flows down to the coast (as suggested by Stevenson and Wilson, (1997)). We propose a mode of emplacement that considers both heterogeneous cooling and thermal annealing in order to explain the range and distribution of modeled cooling rates.

Fountain-style eruption of low viscosity magma with a high melt fraction with a possibly highly variable mass flux is suggested. In periods of high mass flux, the deposition and accumulation rate close to the vent is sufficiently high to promote agglutination, coalescence and subsequent rheomorphic flow of coherent melt-rich lavas. Surfaces exposed to air or adjacent to a cooler surface cool more rapidly than the inner part of the layers. In periods of low relative mass flux, or simply due to more rapid cooling in the outer part of a high mass flux lava fountain, pyroclasts reach their glass transition temperature more quickly, leading to layers of scoriaceous material. Upon rejuvenation of high mass flux rates, the third hot coalesced spatter layer forms. Layers of scoria rafted between layers of still viscous melt-rich material flow down slope. Assimilation and homogenization of scoria both after accumulation and during rheomorphic flow, which localizes along melt-rich layers, result in the thickening of hot coalesced spatter layers. The formation of small thin hot melt-rich layers interfingering with scoria repeats numerous times. Progressive aggradation, similarly to the emplacement of ignimbrites (Branney and Kokelaar, 1992), by which hot-melt and scoria layers flow rapidly over still-flowing or already-emplaced melt-rich and scoria layers, creates conducive conditions to thermal annealing of glass. Such a process impedes cooling of the underlying layers, maintaining their temperature in or above the glass transition and providing sufficient heat and time to anneal the glass in the underlying layers. The thermal history recorded in the glass is then obscured. Eventually, the ca. 7 m thick and ca. 300 m long spatter-fed rheomorphic lava flow is produced. Flow ramps at the front of the deposit and closer to the vent at the top of the deposit support this mode of emplacement (e.g., Gottsmann and Dingwell, 2001b).

Syn-rheomorphism folding and fracturing of layers represents differential relaxation time scales between scoria and viscous layers such that the deformation imposed by gravity-driven flow, differential rheology and cooling of the individual layers is sufficient to induce glassy behavior locally. The thickness, width and length of the glassy layers, which represent the homogeneous coalesced melt layers during flow, are mostly acquired during emplacement. Additional densification or welding may occur after deposition if temperatures remain within the glass transition range. The minimum welding temperature can be scaled to $T_{g\text{onset}}$ (Giordano et al., 2005).

The dark microlite-rich regions of the glass are relatively more oxidized scoria pyroclasts that have been incorporated in the viscous melt-rich layers, flattened, in part boudinaged, and welded, but have retained part of their textures to various degrees depending on the temperature at the time of incorporation in the viscous layers. This is akin to the interpretation that fiamme

are incorporated, flattened and welded pumice clasts preserved in welded ignimbrites (Branney et al., 1992). Therefore, textural homogenization did not occur ubiquitously. TRM1 may be a sample that preserved a higher volume content of scoria clasts that were hot enough to deform but not hot enough to weld. Viscous welding may occur as long as the melt is allowed to restructure itself to a certain degree (Giordano et al., 2005). The viscous welding process stops as soon as the structure in the melt is frozen in. Fractured and folded ribbons are formed during flow as either (1) the melt in these ribbons cooled to glass and was continually stressed until elastic fracture or (2) cooling to conditions where the strain time scale exceeded the relaxation time scale, induced the glass transition directly and fracture proceeded (Webb and Dingwell, 1990). Based on microscopic observations of thin sections, it seems that the welding process proceeded more slowly around phenocrysts. The scoria textures reveal stretching and thinning out to the point where only a thin layer around phenocrysts remains.

The eruptive temperature of magma is a very important factor in the rheology of the rheomorphic spatter-fed flow deposit here studied. It is a principle parameter in determining the time window during which spatter can accumulate, coalesce, flow, aggrade and remain above $T_{g_{onset}}$. White et al. (2009; 2005) found that their most peralkaline lava (A.I. = 1.97) plots in the “no-oxide” field due to the presence of aenigmatite without ilmenite, and suggest relatively low log oxygen fugacity of -16.9 and very low crystallization temperatures of ca. 700 °C, based on geothermometry of feldspar and clinopyroxene. We have not observed ilmenite in the glass from the Tramontana rheomorphic spatter-fed flow. Although there is a possibility that we could find ilmenite crystals if we looked at an even greater selection of samples, we suggest that this flow had low crystallization temperatures and set a conservative minimum eruptive temperature between ca. 700 - 900 °C and a temperature window of ca. 250 to 450 °C for the conditions conducive to welding or annealing, if we take 450 °C, our lowest experimental temperature, as the minimum temperature where the melt can still relax.

The annealing experiments show that if the temperature of a molten layer is kept at 450 °C or above for at least a day after entering the glass transition, significant annealing occurs. This annealing temperature-time window implies the possibility of (1) shear strain inside the deposit down to ca. 450 °C, (2) the incipient to thorough welding of incorporated pyroclasts and (3) the incorporation and welding of additional pyroclasts, and (4) revesiculation. The time spent in this temperature-time window may be partly influenced by shear inside the individual viscous layers. Shearing can be localized along planes defined by differential rheologies imparted by components such as fiamme, phenocrysts or bubbles inside the still-viscous layers. Microscopic evidence points to the shearing of fiamme (Figure 3.12a). Direct frictional heating of scoriaceous clastic layers (Lavallée et al., 2015) or viscous heating in the melt layers (Hess et al., 2008) provides an additional heat production mechanism to maintain the residence time above or in the glass transition interval, promoting viscous processes described and annealing. Any heat production in the flow is an additional cause for the very slow cooling rates and unsystematic distribution of cooling rates. Moreover, we can speculate that the shear planes are

ephemeral features that form and heal (Cordonnier et al. 2012b) and that shear planes migrate to other locations within layers. It is possible that the phenocrysts and glomerocrysts get broken up and produce numerous single microphenocrysts. The inhomogeneity of the SiO₂ and Cl content potentially controls the location of the shearing planes because certain areas are less viscous than others within individual layers. Chemical heterogeneity provides yet another mechanism for differential rheological properties between or within layers.

Our two higher-porosity samples are from sampling sites closest to the vent and the holocrystalline lava-like part of the deposit is farthest from the vent, at the coastline. The presence of lava-like pantellerite may mean that the lava stays above the glass transition longer. The fire fountaining may be more intensive at the beginning of the eruption and more heat is retained. The lava is more fluid and advances faster than the remaining of the deposit that contains scoria. The hot clastic spatter is quickly assimilated to the flow. The eruption wanes so that less heat can be preserved in the agglutinate pile, thus reducing the capacity to assimilate the pyroclasts. The temperature of the hot-melt layers and lava-like part of the deposit reaches the 450 - 600 °C temperature window quickly enough to avoid crystallization due to increased viscosity and low diffusion rates. It is debatable whether the holocrystalline pantellerite crystallized above, or below the glass transition as a devitrification process. Taking the fastest modeled cooling rate and an eruptive temperature of 800 °C (an average temperature based on published suggested temperatures), the glass cooled at $\sim 36 \text{ K hour}^{-1}$ (10^{-2} K s^{-1}) through the glass transition and reached 450 °C within a maximum of 10 hours (assuming a linear cooling trajectory from eruptive temperature), defining a crude welding time window. Calculated cooling rates are considered constant close to $T_{g_{peak}}$, but we are aware that the cooling rate actually decays exponentially with temperature. External heat input will lengthen that time window and promote further welding and thermal annealing.

With their experiments at $T > 1050 \text{ °C}$ on basaltic glass, D’Orsano et al. (2013) show that welding occurs for low fO₂ conditions (sealed environment not opened to air). This would suggest that the scoria clasts were exposed to air, and that the glassy layers resulted from molten pyroclasts that were not or barely exposed to air and retained enough heat to remain in the temperature window required for agglutination and coalescence after eruption.

Few studies discuss the emplacement processes of glassy spatter-fed rheomorphic lava flows (e.g., Gottsmann and Dingwell, 2001a, b, 2002; Sumner et al., 2005), or the emplacement of non-glassy spatter-fed flows (e.g., Head and Wilson, 1989; Palladino and Simej, 2005; Sumner, 1998). The presence or absence of glass in the context of spatter-fed lava flows mostly depends on the composition of the magma. Spatter-fed lavas containing glass are of peralkaline composition and lavas that are crystalline have often basaltic to andesitic compositions. Emplacement mechanisms of agglutination and coalescence, as well as the flow architecture of glassy and non-glassy spatter-fed flow deposits are in some respects comparable. However, because crystallization is hindered, peralkaline lavas may have a longer time window in the

viscous flow regime within the glass transition and in the supercooled liquid before final deposition, which favors coalescence. The presence of crystals in a melt increases both mechanically its bulk apparent viscosity and chemically the groundmass melt viscosity due to increased silica content (e.g., Goto, 1999). Because of these viscosity-increasing effects, a cooling and crystallizing basaltic flow could enter the brittle response regime more quickly than a peralkaline flow.

The determination of cooling histories is challenged by thermal annealing effects and enthalpy relaxation geospeedometry should be used with caution in the case of lava flows, rheomorphic lava flows and pyroclastic flows. Nevertheless, it is clear that the range and distribution of cooling rates represent the inhomogeneous cooling and formation of the deposit.



The Nature and Emplacement of a Phonolitic Glassy Volcaniclastic Deposit Within the Guajara Formation, Tenerife

4.1 Introduction

The formation of volcanic glass is dominantly controlled by the cooling history, the temperature-dependence of viscosity, dissolved volatile content and composition of the melt (Dingwell, 1996; Dingwell et al., 1998; e.g., Uhlmann and Yinnon, 1983). Fragments of magma, or pyroclasts, produced during explosive eruptions, undergo the glass transition at a time between formation and final deposition, whether during flight or after emplacement. Once the glassy state has been reached, pyroclasts behave in a brittle manner unless (1) another heat source acts to raise the temperature of the pyroclasts above the glass transition interval again,

or (2) the deforming stress is released while the temperature is sufficiently high to allow subsequent structural relaxation. Therefore, only when the temperature of the erupted magma is above or within the glass transition range can the magma relax viscously. The glass transition range is a critical temperature interval that represents a kinetic boundary between the brittle and ductile states of magma (Dingwell, 1990).

The formation of welded deposits from initially pyroclastic deposits is well documented (e.g. Smith, 1960) and experimentally investigated (e.g. Wadsworth et al., 2014; Sumner et al., 2005). It is thought to progress by viscous densification of pyroclasts, which is dominantly dependent on the melt viscosity. Regardless of melt composition, deposition of relatively low viscosity spatter, produced by lava fountains, can result in its agglutination and coalescence, and form spatter-fed lavas (see Chapter 3, Grunder and Russell, 2005; Sumner et al., 2005; Wolff and Sumner, 2000), whereas pyroclasts from a pyroclastic density current that are relatively highly viscous at deposition, can weld together, but may produce more viscous slow moving rheomorphic welded ignimbrites (e.g., Lavallée et al., 2015), in comparison to the spatter-fed flows.

Volcaniclastic deposits may show various degrees of welding, from non-welded to glassy (or lava-like) and it remains a challenge to elucidate which eruptive scenario and processes produced the deposits that we observe, often long after the actual eruption. (1) Fresh deposits are more difficult to study because of the hazard they pose, but also because there are rarely accessible vertical profiles through fresh deposits. However, many exposed older volcaniclastic sequences of variable welding intensity are accessible and have been described. Soriano et al. (2002) described in detail sequences where the welding intensity increases gradually upwards from non-welded to lava-like. Other studies have reported the occurrence of vitrophyric units within ignimbrites with decreasing welding intensity in the facies above and/or below (e.g., Ekren et al., 1984; Gimeno et al., 2003; Lavallée et al., 2015; Robert et al., 2013; Sumner and Branney, 2002; Willcock and Cas, 2014; Williams et al., 2014). (2) Distinguishing between flow and rheomorphic fallout deposits can be ambiguous because they can share common features such as a lack of clastic textures, or the presence of flow banding and homogeneous glassy or crystalline units. There are a number of deposits for which the interpretation has changed over the years (e.g., The Green Tuff, Orsi and Sheridan, 1984).

Shedding light on the cooling history of a deposit can help deciphering its emplacement process. One tool to probe glasses for their cooling history is calorimetry. Thermal analyses of peralkaline glasses have been performed to estimate their cooling rates for a better understanding of the genesis of volcaniclastic deposits and individual volcanic bombs (e.g., Gottsmann and Dingwell, 2001a, 2002; Wilding et al., 1996a). These thermal analyses focused on the modeling of heat capacity (C_p) curves obtained upon repeated heating of glasses. These C_p curves show typically one pronounced peak for which the peak height, width and

temperature range are directly related to the pressure-temperature-time path of the glass formation in nature.

Here we focus on a volcanoclastic glassy deposit from the Guajara Formation on the island of Tenerife. The deposit does not show a typical gradual vertical increase or decrease of welding intensity, but rather the presence of a densely welded phase dispersed in lava-like obsidian. The proportion of the densely-welded phase relative to obsidian increases gradually upward. Thermal analyses of both phases have shown a high-amplitude and pronounced first Cp peak for all samples analyzed, but have also revealed additional Cp peaks. Through the interpretation of geological field relationships combined with textural, geochemical and thermal analyses, we propose an explanation for the nature and emplacement of the deposit.

4.2 Terminology

A few terms are clarified to avoid any confusion. We define **primary juvenile clasts** as material derived from the eruptive event being studied that provides heat to transport and/or fragmentation processes. We define **lithic clasts**, as rock fragments of any origin formed previous to the eruption studied (White and Houghton, 2006). **Sintering** refers to the formation of a neck between two viscous pyroclasts. **Welding** is the flattening of juvenile pyroclasts (Smith, 1960). This process produces aligned fiamme and flattened shards that form a **eutaxitic** texture (Ross and Smith, 1961). **Fiamme** is a lens or flame-shaped feature such as a flattened pumice lapilli or magma bleb (Bull and McPhie, 2007). Welding may occur due to load compaction or agglutination of spatter (Wolff and Sumner, 2000). **Agglutination** represents the accumulation, flattening and immediate welding of hot and fluidal pyroclasts erupted from lava fountains upon landing (Branney and Kokelaar, 1992; Mahood, 1984; Sumner et al., 2005; Wolff and Sumner, 2000), which may be followed by the coalescence of the pyroclasts. **Coalescence** refers to the obliteration of pyroclast outlines and leads to the formation of lava-like deposits (Branney et al., 1992; Duffield, 1990; Ekren et al., 1984; Freundt and Schmicke, 1995). **Grade** represents the degree of welding of a deposit (Walker, 1983). **Trachytic** texture refers to the alignment of lath-shaped feldspar microlites in the groundmass of a volcanic rock.

4.3 Geological Setting

The Guajara Formation is located on the intraplate oceanic island of Tenerife, and is part of the Canary Islands, Spain, in the eastern central Atlantic Ocean off the northwestern coast of Africa (Figure 4.1). The island of Tenerife results from the formation of a first subaqueous and later subaerial mafic shield volcano structure with subsequent post-shield volcanism of mafic but mainly more evolved, phonolitic magmas (Ridley, 1970). The geological landscape (Figure 4.1) consists of (a) the phonolitic Pico-Teide and Pico-Viejo volcanic complex (PT-PV) formed by

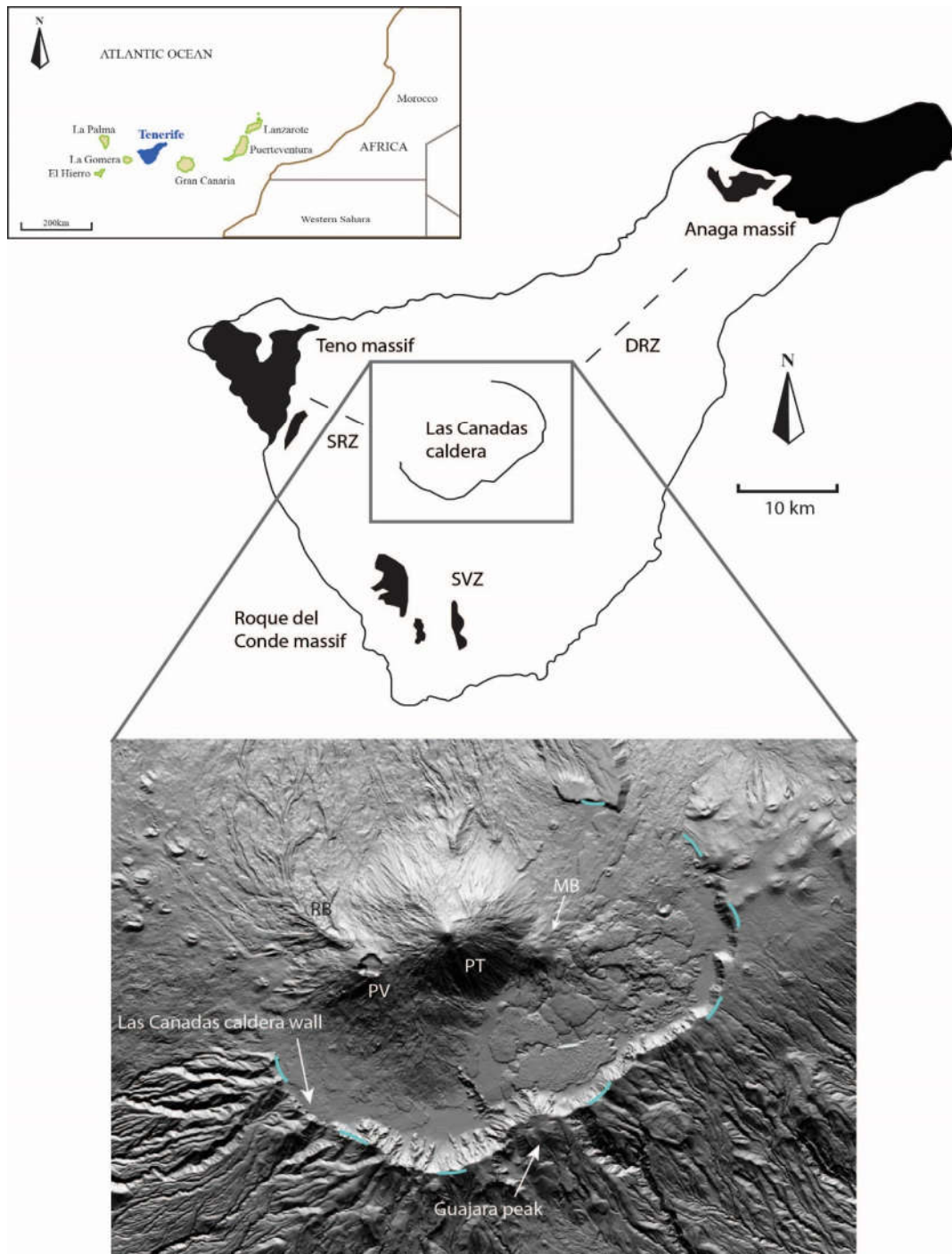


Figure 4.1 Geological setting of study area. Inset at the top locates Tenerife, in the Canary Islands, relative to Africa and the other Canary islands. The central map shows the island of Tenerife with its three basaltic shield massifs, the Santiago Rift Zone (SRZ), the Dorsal Rift Zone (DRZ) and the Southern Volcanic Zone (SVZ). In close-up is a DEM image of the nested caldera (dashed blue line). Pico Teide (PT) and Pico Viejo (PV) form the youngest stratovolcano complex. To the east of PT-PV is Montana Blanca (MB) and on the northern flank of PV, Roques Blancos (RB). The deposit studied is located at Guajara peak, within the Guajara Formation, along the south eastern part of the Las Canadas caldera wall.

two stratovolcanoes and deposits from flank-vent systems (Ablay and Marti, 2000), (b) three volcanic zones, two of which are rift zones, where volcanism of mafic to intermediate composition predominates (Ridley, 1970), (c) the Las Canadas edifice (LCE) that consists of overlapping volcanic centers (Ancochea et al., 1990; Ancochea et al., 1999; Arana, 1971; Marti et al., 1994) and (d) three eroded shield massifs that are remnants of the shield volcanoes (Ancochea, 1990, Abdel-Monem, 1972). Volcanism in the PT-PV system seems to follow the previous volcanic cycles, which consisted of several phonolitic explosive eruptions and caldera collapse events (Arana, 1971; Brown et al., 2003; Marti et al., 1997; Marti et al., 1994). The LCE is transected by a prominent structure, the Las Canadas Caldera (LCC). The LCC is a composite nested structure that possibly formed by multiple vertical and lateral collapse events during the Upper Group explosive volcanic activity (Arana, 1971; Brown et al., 2003; Marti et al., 1994). The northern and western walls are absent. The LCE is divided into a mostly mafic Lower Group and a felsic Upper Group (Marti et al., 1994). The latter comprises three volcanic formations: Ucanca (1.59-1.18 ka), Guajara (850-570 ka) and Diego Hernandez (370-179 ka). These formations are thick deposits of phonolitic lava and pyroclastic material produced by nearby vents. Deposits present on the outskirts of the island, within the Bandas del Sur Group on the southern slopes of the island, have been interpreted to represent the distal equivalent of the thick deposits found along the caldera walls (Brown et al., 2003; Bryan et al., 1998). The present study focuses on the glassy bottom section of a proximal volcanoclastic deposit below Guajara Peak, within the Guajara Formation, located along the Guajara caldera wall southeast of the PT-PV complex.

4.4 Sampling Site and Material

The chosen sampling site for this study is the easily-accessible well-preserved glassy base of a formerly volcanoclastic deposit within the Guajara Formation. It is located at ca. 1500 m elevation at UTM grid coordinates 28 R 0342417/3122485. Bryan (1998) has performed a detailed study of the Guajara Formation at Guajara Peak, which encompasses the glassy unit studied here, identified as Facies 1. We also refer to this deposit as Facies 1, which is interpreted as a spatter agglutinate within the Guajara Welded Unit (GWU), a pyroclastic sequence. His study offers an exceptional opportunity to better understand the emplacement of Facies 1 by providing a detailed geological context, as well as a detailed description of Facies 1 itself.

Figure 4.2 (next page) The Guajara Welded Unit (GWU) at the top of the Guajara Formation. (a) and (b) show the vertical extent of the GWU and well-defined deposit beds toward the base. (c) Facies 1, the glassy base of GWU, and overlying pumice fall deposit. (d) Brecciated obsidian at the contact (arrow) with the underlying pumice-rich deposit. (e) Facies 1: green phase dispersed within obsidian. The proportion of the green phase increases upward. (f) Close-up on Facies 1, the green phase has very irregular outlines. A pink star is to the left of a clast surrounded by a thin layer of glass, in the green phase. P stands for pumice.





Figure 4.3 (a) Sampling profile ~1 m high at the base of Facies 1 in the Guajara Welding Unit. (b) GUA3, a hand sample of obsidian in contact with the green phase, both containing pumice and lithic lapilli, sampled at the Guajara Formation, Tenerife. The white rectangle indicates the location of the GUA3-1 cylinder. 1 Euro piece for scale. (c) Example of a sample cylinder. Note the sharp contact (arrow) between the obsidian and the green phase. The light brown lines perpendicular to the length of the cylinder are a result of the drilling.

Facies 1 is characterized by four components at the scale of the outcrop: (a) a crystal-poor obsidian in which (b) a light-to-dark-green phase, which we simply call the green phase, is dispersed; (c) light brown poorly vesiculated angular to subangular pumice lapilli; and (d) light to dark grey dense to poorly vesiculated subangular to subrounded lithic lapilli.

At the macroscopic scale, the contact between the obsidian and the green phase is sharp but sometimes very irregular (Figures 4.2f and 4.3c). The deposit is not visible everywhere and its exposure is not as fresh and planar everywhere, where exposed, as it is at the chosen sampling site. At the sampling site, about 30 cm of the base of the deposit consist of obsidian only, after which the proportion of the green phase increases upward rapidly. Based on our observations along the same exposed wall within a few tens of meters, this glassy base varies in thickness throughout the deposit, from less than a cm to >30 cm (Figure 4.2d, e). Where the glassy base is very thin, obsidian angular clasts are present in Facies 1 directly above the contact and also at the top of the underlying unit (Figure 4.2d). The clasts contained in the lower unit could actually be clasts that were at the contact with Facies 1 but were exposed due to the erosion of the Facies 1 bed. At the sampling site, the lower 20 cm are heavily fractured and friable.

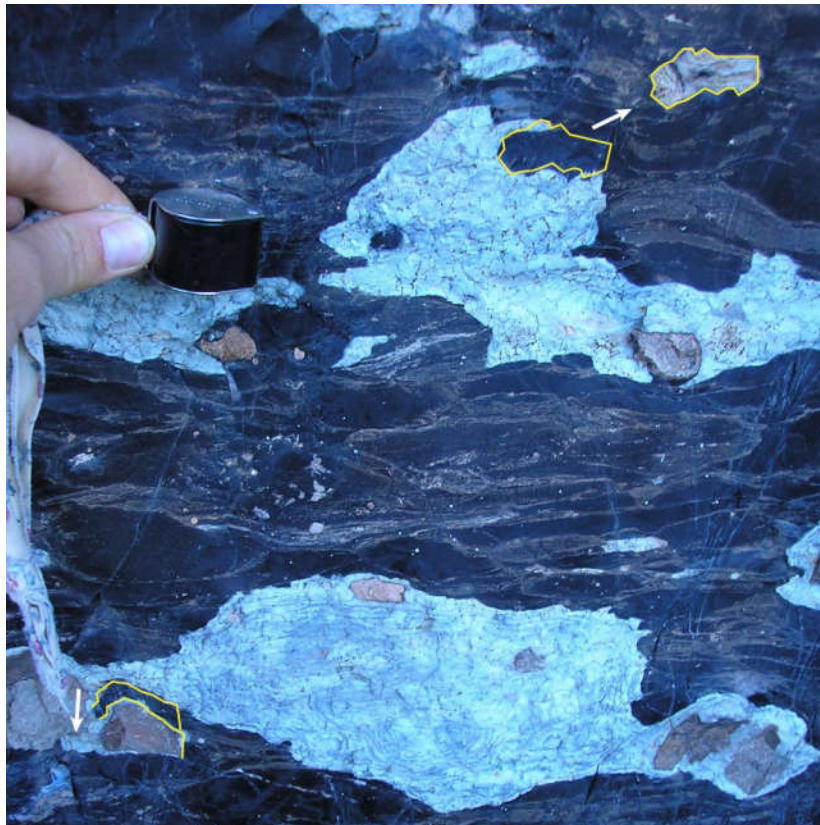


Figure 4.4 Puzzle of the green phase (top and bottom). The green phase and the obsidian are viscous during emplacement and green phase fragments detach and move only a short distance away. Drawn contours outline the fragments that have moved. Also shown is their probable location before detachment. Note the light-brown bands and patches in the obsidian and the small-scale fault where there is ca. 1 mm nearly vertical displacement in the top image.

Obsidian is readily visible for ca. 125 cm from the bottom contact of the deposit after which it becomes scarce. Weathering of the deposit surface obscures observations higher up in the unit. Thin light brown bands are found in the obsidian, possibly representing the remaining outline of compacted oval-shaped pyroclasts (Figure 4.2f-h). The obsidian contains also light brown wavy and folded elongated vesicular bands and patches of up to a few cm in length that may represent stretched pumice clasts, possibly incorporated fragments of the green phase, or re-vesiculated glass along small local shear planes (Figure 4.4).

The green phase consists of more or less elongated flattened blobby clasts that have an irregular curvy undulating, in part, cauliform or with flaming endings, or angular outline. A surface of Facies 1 approximately perpendicular to the drilled outcrop face shows that the green phase clasts have an elongated flattened profile in both horizontal perpendicular directions (Figure 4.2e). The degree of flattening is however highly variable and is greatest near the upper part of the mostly glassy base of the deposit where elongated stretched clasts of the green phase align (Figure 4.2e). Oddly, low aspect ratio clasts of the green phase occur right below this thinned horizon. Dark green lines often parallel the outline of lithic clasts. Subangular to subrounded low porosity lithic lapilli are found throughout the deposit and are sometimes wrapped in a thin obsidian layer when found inside the green phase (Figure 4.2f). We observe small fragments of the green phase that have detached from larger blocks, flowed away but only for a short distance, allowing us to put the pieces back together, as in a puzzle (Figure 4.4). Interestingly, some of the small fragments that have detached have arcuate shapes similar to the arcuate shape of the crenulations around lithic clasts contained in the green phase. The small fragments detached most likely along these weaker planes.

We collected a block from the sampling site and drilled cylinders with 2.5 cm diameter along a 1 m long more or less vertical profile from the base of the deposit up to a section where glass is scarce (Figure 4.3). Cylinders are ca. 10 cm apart. We aimed predominantly at sampling obsidian and one cylinder was drilled in the green phase.

Following is a summary of the observations and interpretations of Bryan (1998) on the GWU. The Guajara Formation at Guajara Peak has an approximate thickness of 250 m, is composed mostly of 3 lava-like welded pyroclastic units and of the GWU, and is underlain by deposits of the Ucanca Formation. The GWU has been divided into 8 volcanoclastic units termed Facies 1 to 8. Within the eight facies of the GWU, the welding intensity varies rapidly and alternates from high to low to high again. Facies 1, the obsidian-rich unit from this study, is the up-to-3m-thick lowermost deposit of the GWU and is in sharp contact with underlying sintered pumice fall deposits. An up to 75 cm-thick partly to non-welded fallout layer occurs in the top part of Facies 1 and comprises nonwelded pumice, lithic clasts and spatter. Facies 2 overlies Facies 1 and consists of a 1 m-thick bed mostly of blocky low-porosity nonwelded pumice. Facies 1 is interpreted as a fallout pyroclastic deposit, namely a spatter agglutinate, produced by a phonolitic explosive eruption and emplaced close to the vent. Welding due to load compaction

of the deposit is excluded and welding textures are rather explained as the result of agglutination during Strombolian eruptions, favoring high accumulation rates, high temperatures and low fountain heights (Houghton et al., 1985; Sparks and Wright, 1979). Bryan (1998)'s suggested interpretation for the presence of both obsidian and "white obsidian" (described as the green phase in the present study) is the hydration and devitrification of the glass due to the emplacement of Facies 4, a water-rich fine-grained deposit produced by a later phreatomagmatic eruption. Water would have seeped down through the underlying deposits, causing patchy devitrification of Facies 1. The obsidian and white obsidian represent ~90% of the deposit.

4.5 Methodology

This study focuses on results from the modeling of C_p curves of near-aphyric phonolitic obsidian from a volcanoclastic deposit within the Guajara Formation in order to estimate cooling rates and better understand its emplacement. To adequately describe the phases present in the deposit, thin sections and geochemical analyses of the thermally analyzed glasses and the green phase are performed.

4.5.1 Sample Characterization

All measurements are performed at the Ludwig-Maximilians-Universität München (LMU), Germany. Obsidian, a light-to-dark-green phase, to which we simply refer to as the green phase, and fine-grained brown lithics from sample GUA-3 are observed under the optical microscope for textural analysis and phenocryst identification. We utilize the electron microprobe (EMPA), using a 15 keV accelerating voltage and 5 nA beam current, to measure the chemical composition of the groundmass glass in the obsidian and the green phase. A defocused electron beam of 10 μm and a counting time of 10 s are used to perform the measurements in order to prevent volatilization of the mobile Na and K elements contained in the groundmass glass. Standards are albite (Na, Si), periclase (Mg), orthoclase (Al, K), apatite (P), vanadinite (Cl), wollastonite (Ca), Cr_2O_3 (Cr), Fe_2O_3 (Fe), anhydrite (S), and ilmenite (Ti, Mn). The water content is estimated by measuring mass loss during the heating of samples up to 1300 $^\circ\text{C}$, using a Netzsch $\text{\textcircled{R}}$ STA 449C instrument that combines differential scanning calorimetry with thermogravimetry.

4.5.2 Geospeedometry

Cooling rates of glassy components of Facies 1 are calculated using enthalpy relaxation geospeedometry, also called the Tool-Narayanaswamy-Moynihan (TNM) method. We refer to Chapter 3 of this dissertation for a detailed description of the TNM method. The heating and cooling cycles are performed at 7, 10, 15 and 20 K min⁻¹ on polished glassy discs of ~6 mm diameter with a mass of ca. 28 or ca. 62 mg.

4.6 Results

4.6.1 Microscopic Textures

In the obsidian, we observe elongated narrow areas of long and fine black lines overprinted by brown to translucent rounded features of higher relief than the glass (Figure 4.5a-b). Radiating fibers contained in these rounded features are visible under cross-polarized light and interpreted as spherulites that crystallized after emplacement of the deposit. The black lines could be remains of pyroclast cooling surfaces or flow bands.

The spherulites have up to ca. 100 μm diameter, and have a dark brown center and a light brown to translucent periphery, often with Fe-oxide nanolites in the middle (Figure 4.5b). Several spherulites are as small as 20-30 μm . The rare phenocrysts present in the glass are quartz, ca. 0.5 mm long (Figure 4.5d). The glass is clear with <1 vol% microlites and <1 vol% porosity. Elongated areas between the glass and the green phase have microlite content of >50 vol%. Interestingly, the contact is sometimes very sharp and does not portray any transitional microlite-rich zone. The green phase in contact with the glass usually shows more pervasive, irregular at the microscopic scale, orange-dark brown devitrification (Figure 4.5h) and original textures are greatly obscured. Obscured textures are also observed, but to a lesser extent, at the contact between lithic clast and green phase, forming a ca. 150 μm wide band around the lithic clast (Figure 4.5k).

The green phase consists of three ash-size components: (1) pumice fragments, (2) very fine pumiceous ash and (3) lithic clasts/Fe-Ti oxide blobs. The ash-size pumice fragments, which are easily recognizable under the microscope and flattened to various degrees (Figure 4.5c, e, f), are surrounded by a finely crystallized groundmass possibly of former very fine pumiceous ash. Given the high grade of the green phase, the size of the pumice clasts or fragments is an approximation. Based on the presence of rinds and bubbles of various orientations observed under the microscope with plane and polarized light, we identify pumice fragments up to ca. 500 μm long. The pumice fragments and pumiceous ash form a foliated material that is crenulated in numerous areas (Figure 4.5c, g) with devitrified brown bubble walls. The

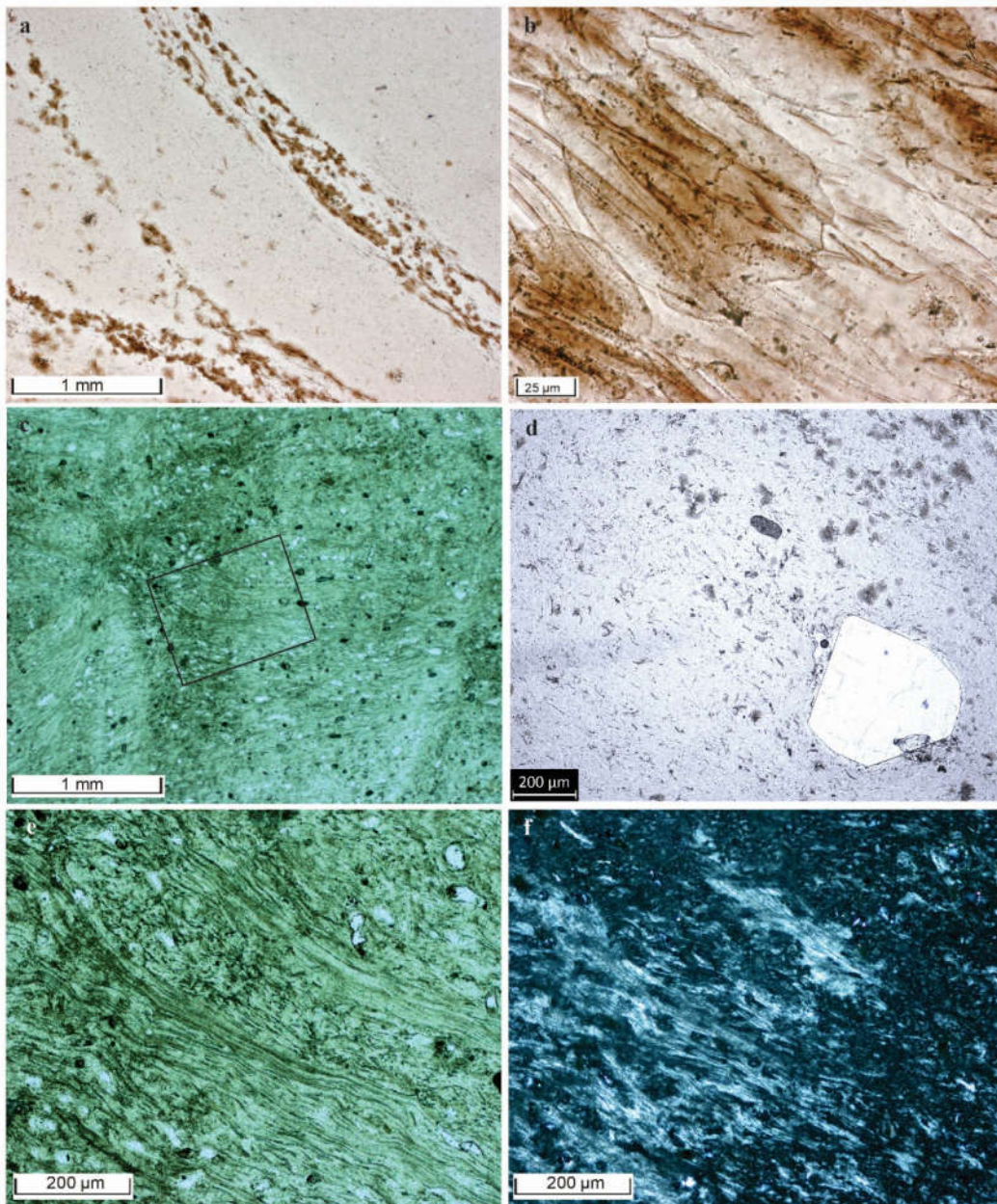


Figure 4.5 Microscopic textures **a** spherulitic bands in obsidian (ppl), **b** spherulites (ppl), **c** shards and pumice fragments in the green phase (ppl), **d** quartz phenocryst (ppl), **e** inset in **c** of the outline of a pumice clast (ppl), **f** same as **e** but under xpl. We observe bubbles in the pumice clasts and broken bubble walls.

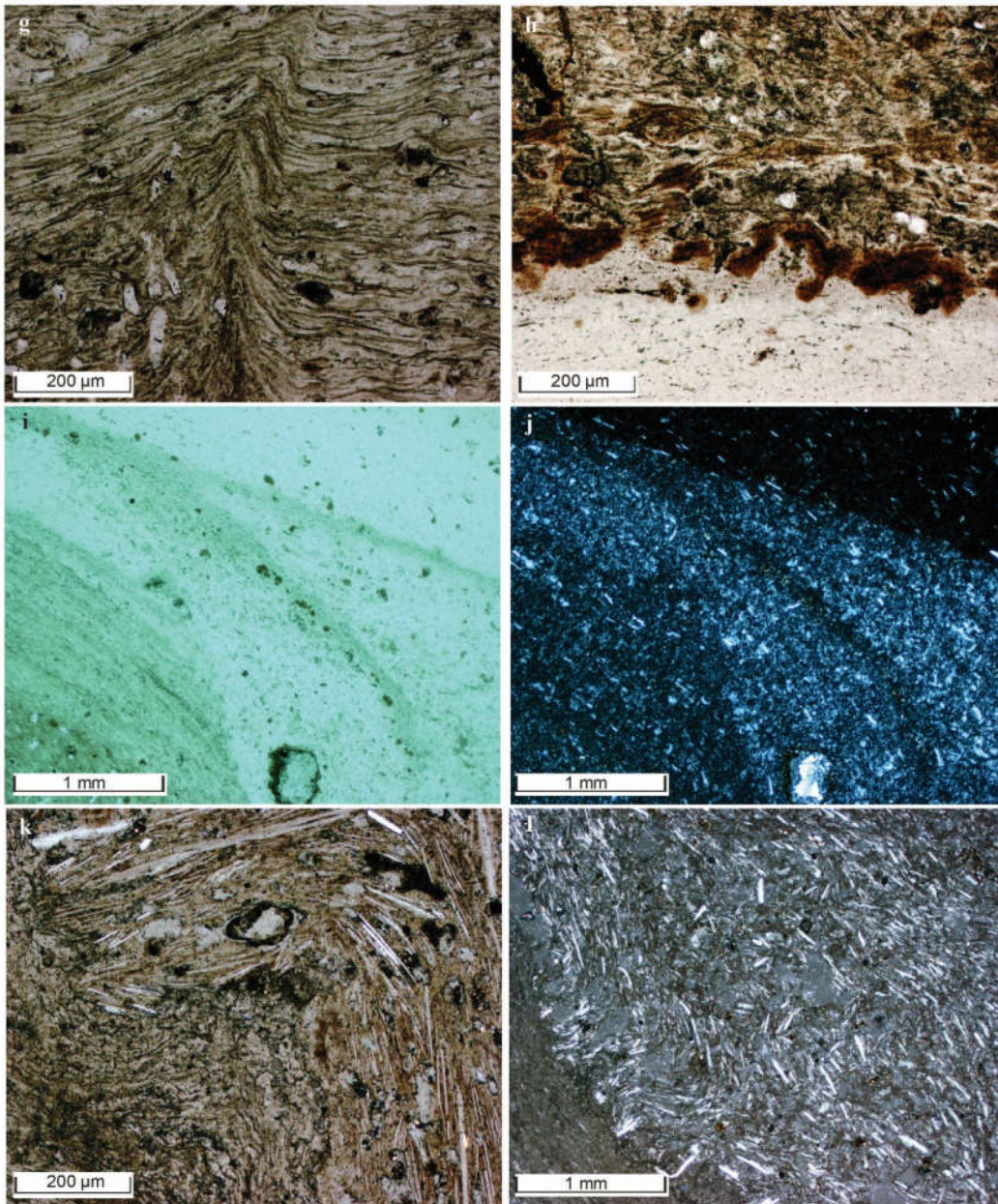


Figure 4.5 (continued) Microscopic textures observed in the obsidian, green phase and lithics (ppl). **g** crenulations in the green phase, **h** devitrified contact between obsidian and green phase (ppl), **i** zone of microlites between obsidian and green phase (ppl), **j** same as **i**, but under xpl. **k** contact between lithic (right) and green phase (left) (ppl), **l** porosity seen as light grey in lithic clast (xpl, angle $< 90^\circ$). ppl refers to plane polarized light, xpl, to cross-polarized light.

crenulation patterns are complex and correspond to the dark green lines observed at the macroscopic scale. There are also ca. 2 vol% subrounded dark brown to black blobs (possibly lithics) in the green phase. The eutaxitic texture formed by the flattened pumice and shards is disturbed by these blobs and wraps around them. Some of these blobs have been removed, possibly during the preparation of the thin sections, leaving holes that could be interpreted as vesicles. However, the black blobs and holes could indeed represent the original porosity of the pyroclastic material. The vesicles were deformed during viscous flow and at least in part later filled with Fe-Ti oxides. An alternative is that the porosity results from revesiculation.

Lithic clasts have a fine-grained groundmass and are light brown to light grey. One dark grey lithic clast observed under the microscope has ca. 30 vol% porosity, ca. 15 vol% feldspar microlites, ca. 2 vol% subrounded dark brown (Fe-Ti oxide) blobs and ca. 2 vol% irregularly shaped vesicles. The microlites are in part parallel, in part perpendicular to the contact with the green phase. The light to dark green color of this phase attests to the pervasive devitrification of the pyroclastic material.

4.6.2 Composition

The main composition of the glass is within error identical to the composition of the green phase (Figure 4.6, Table 4.1). It is in fact impossible to detect the transition between the glass and the green phase when looking at major element compositions obtained from EMPA measurements. However, the glass does show variations in its K₂O (by ca. 6.5 wt%) and Na₂O (by ca. 4 wt%) content with a constant 3.6 wt% of FeO.

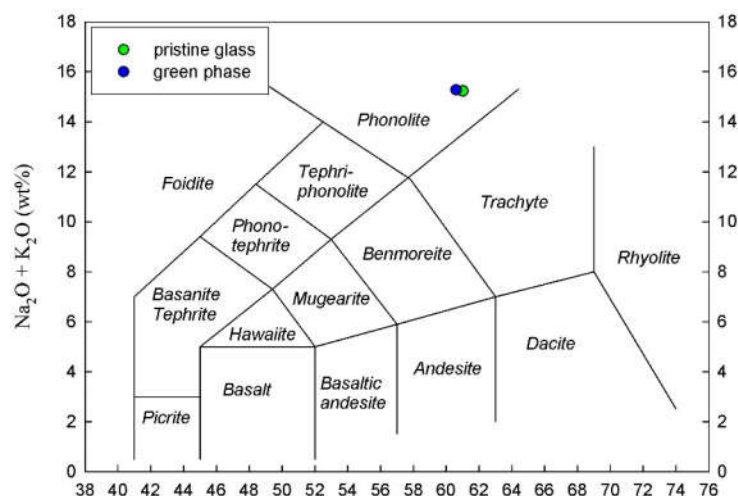


Figure 4.6 Total Alkali-vs-Silica diagram (TAS) for the pristine glass and the green phase of the Guajara groundmass glass.

When the K₂O content is high (8.5 wt% instead of 5.4 wt%), the Na₂O content is lower (6.9 instead of 9.9 wt%). When the K₂O content is lower (2.1 wt% instead of 5.4 wt%), the Na₂O content is high (11.0 instead of 9.9 wt%). These variations arise most likely due to the crystallization of spherulites, in addition to the crystallization of feldspar microlites, which are

Table 4.1 Major element chemical compositions measured with EMPA for groundmass glass and green phase in sample GUA 3 from Facies 1 of the Guajara Welded Unit.

| Major oxides | Green phase | Glass | Glass (lower K ₂ O content) | Glass (higher K ₂ O content) |
|--------------------------------|-------------|-------|--|---|
| n analyses | 19 | 82 | 12 | 12 |
| SiO ₂ (wt%) | 60.61 | 61.02 | 62.70 | 60.27 |
| Al ₂ O ₃ | 17.24 | 16.82 | 17.24 | 17.07 |
| FeO | 3.58 | 3.63 | 3.63 | 3.57 |
| MnO | 0.30 | 0.30 | 0.30 | 0.35 |
| CaO | 0.55 | 0.52 | 0.70 | 0.50 |
| K ₂ O | 5.64 | 5.35 | 2.08 | 8.55 |
| Na ₂ O | 9.63 | 9.88 | 10.95 | 6.91 |
| TiO ₂ | 0.81 | 0.79 | 0.78 | 0.80 |
| P ₂ O ₅ | 0.05 | 0.05 | 0.02 | 0.06 |
| MgO | 0.41 | 0.38 | 0.38 | 0.38 |
| Cr ₂ O ₃ | n.m. | n.m. | n.m. | n.m. |
| Cl | 0.33 | 0.32 | 0.36 | 0.33 |
| SO ₂ | n.m. | n.m. | n.m. | n.m. |
| Total | 99.15 | 99.04 | 99.15 | 98.78 |
| A.I. | 1.27 | 1.52 | 1.18 | 1.21 |

Note: n.m. stands for not measured, n for number of analyses and A.I. for Apatitic Index calculated as the molar ratio (Na₂O+K₂O/Al₂O₃).

richer in Na. Spherulites are typically Na-rich and K-poor (e.g., Castro et al., 2008; Gardner et al., 2012). Thus, the crystallization of spherulites could produce K-rich haloes around spherulites. K₂O-rich zones are absent in the green phase, but more measurements would be required to confirm this observation. The mapping of 100 x 100 µm areas in the glass allowed us to observe these same variations in the K₂O and Na₂O content (Figure 4.7). Given the rounded shape of the element distributions, we can conclude that the variations correspond mostly to the presence of spherulites in the glass. TG analyses up to 1300 °C indicate that there is no significant mass loss, which means that the volatile content is very low (<0.05 wt%). The green phase loses ca. 0.1 wt% between 400 and 600 °C (Figure 4.9c).

4.6.3 Heat Capacity Curves

For more clarity, the smoothed *C_p* curves are plotted on 2 separate graphs in order to better distinguish the position and height of the peaks (Figure 4.9a, b). For both GUA1 and GUA3, we observe multiple peaks separated by up to ca. 140 °C, which is a rather large temperature difference. It is worth noting that the *C_p* peak area within the glass transition of several calibration curves contains hidden peaks and/or peaks of lesser amplitude. These peaks are best

observed on the calibration curves because the main overshoot has smaller amplitude. Looking at the $T_{g_{peak}}$ obtained upon the first heating (Figure 4.9a), GUA1 shows a variation of 20 °C, for $T_{g_{peak}}$ of 637 to 657 °C and GUA3, a similar variation of 21 °C, for $T_{g_{peak}}$ of 630 to 651 °C. The amplitude of the $T_{g_{peak}}$ varies and hints at a difference in cooling rates, and/or

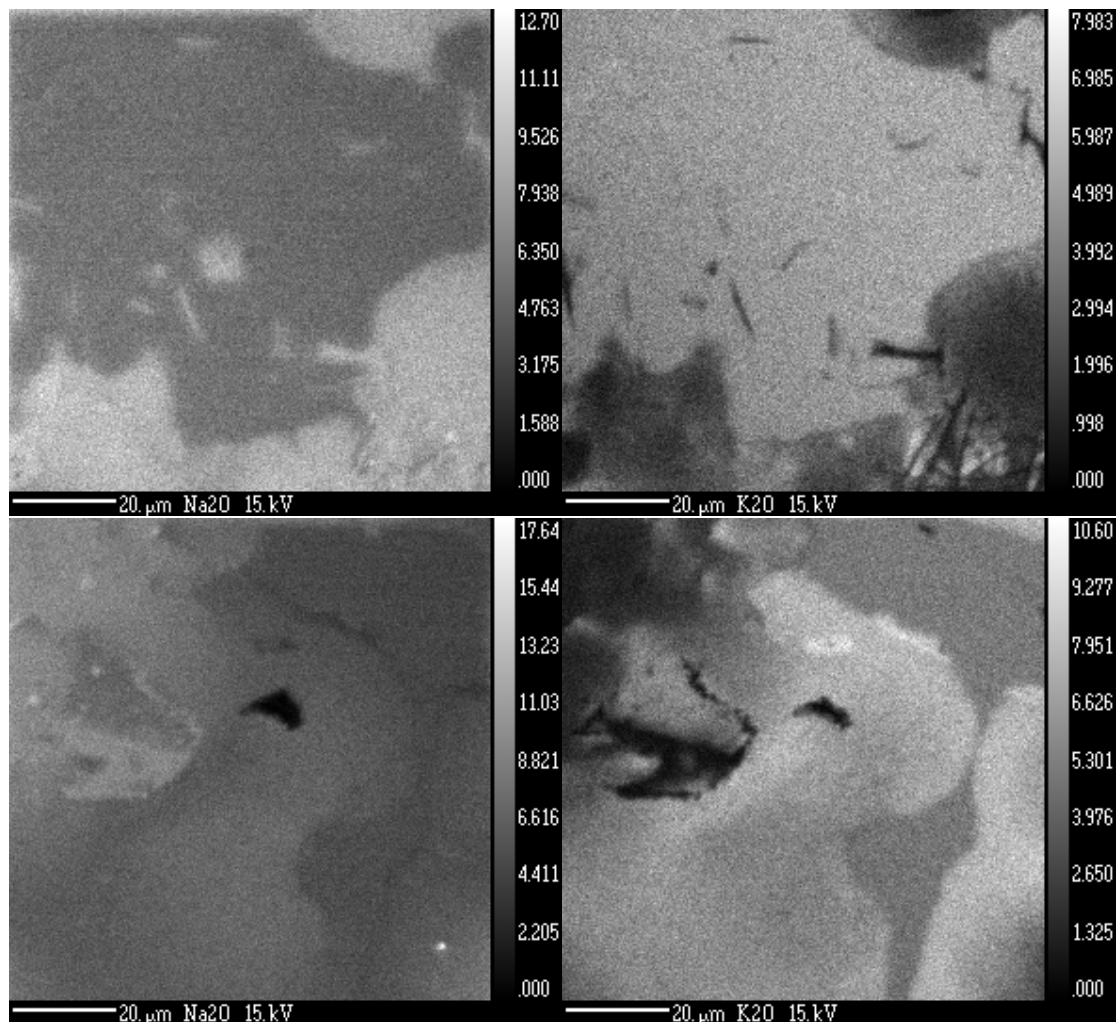


Figure 4.7 Distribution of potassium and sodium oxides in the glass, spherulites and microlites of the Guajara obsidian sample GUA3-1b. The center of the spherulites is potassium poor and its concentration increases radially outwards. The center of the spherulites contains about twice as much sodium as the groundmass glass.

perhaps thermal annealing. If additional relaxation of the glass structure occurs during near-isothermal conditions, higher C_p overshoots result. Looking at the 10-10 K min⁻¹ C_p curves, we obtain two different $T_{g_{peak}}$ values, ca. 635 °C for GUA1-b, g, h and GUA3-1c, and ca. 647 °C for GUA1-a, f and k. GUA3-1a has a $T_{g_{peak}}$ of 626 °C and GUA3-1b, 609 °C. $T_{g_{peak}}$ for the 10-10 K min⁻¹ calibration curves is within a range of 40 °C.

Passed the upper limit of the glass transition, a second pronounced C_p increase occurs less than 50 °C after having reached the supercooled liquid (Figures 4.9a-b, 4.10a). We observe partly

bulged sample surfaces following heating in the DSC up to 840 °C (Figure 4.8). The scale of areas that do not deform, as seen on SEM images (ca. 20 to >100 μm), coincides partly with the scale of spherulites or spherulite agglomerations identified under the microscope. For samples GUA1f-g and GUA3-1a-c, the 2nd peak is sharp, wide and of high-magnitude, with additional small peaks on the flanks of the peaks. Interestingly, GUA1f-g are in the middle and upper middle part of the investigated profile respectively. For the three samples located at the lower end of the unit (GUA1-a, b, k) and the one sample at the upper end of the unit (GUA1-h), the C_p increase occurs over a wider temperature range with several small peaks instead of one pronounced sharp C_p peak and a few small peaks on the flanks of the pronounced peak. A second heat treatment up to temperatures passed the sharp 2nd peaks is performed for GUA3-1b and 1c and results in a C_p increase shifted to higher temperatures.

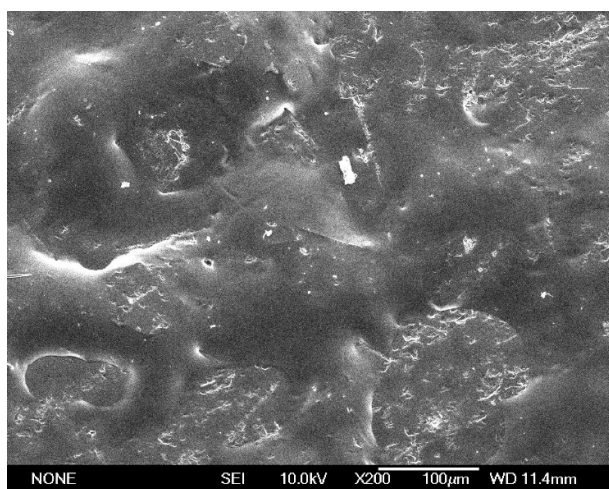


Figure 4.8 SEM image showing the uneven surface of a GUA3 sample after heat treatment up to 840 °C. The spherical features could partly be spherulites.

The TNM procedure is not influenced by those later peaks and is performed without increasing the temperature to more than ca. 10-20 °C into the supercooled liquid. The green phase does not have a glass transition C_p peak, but shows rather a C_p peak around 1020

°C with an additional peak on the flank of lesser temperature at 900 °C. No significant volatile loss has been measured in this temperature range (Figure 4.9c). The C_p peak is caused most likely by the melting of crystalline phases.

4.6.4 Modeling Parameters and Cooling Rates of Phonolites

The model cooling rates span 2 orders of magnitude, 10^{-2} to 10^{-4} K min⁻¹ (Figure 4.10b, Table 4.2). The base of Facies 1 is associated with a higher cooling rate, and modeled cooling rates decrease upwards. The proportion of the green phase increases upward and the glass becomes scarce. The lowest $T_{g_{peak}}$ corresponds to the lowest cooling rate. The glassy part of the hand sample is up to 4 cm thick on either side of the green phase, which allows us to infer that the sample came from the middle of the unit where the green phase is present but the proportion of glass is still high relative to the green phase. Cooling rates obtained from the hand sample, ca. 10^{-2} K min⁻¹, correspond to the rates of the lower half of the measured profile and the 2nd peak is pronounced as for the samples from the center of the unit.

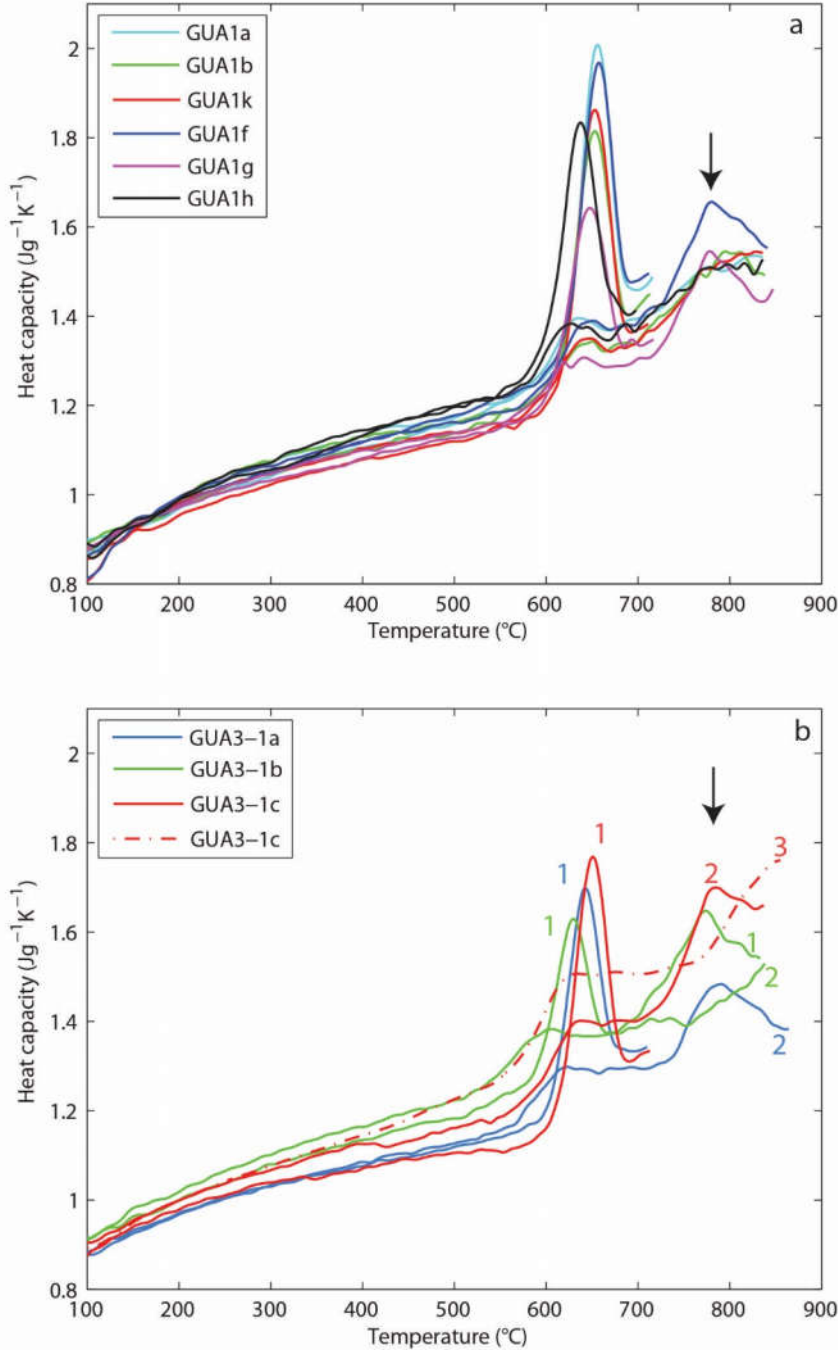


Figure 4.9 Heat capacity curves from the first heating and additional heat treatments with 10 K min^{-1} of the glasses from Facies 1. (a) Vertical profile (b) Hand sample, GUA3-1c was heated three times. 1st time into the supercooled liquid, 2nd time passed the 2nd Cp peak, and 3rd time up to the shifted 2nd Cp peak. GUA3-1b was heated twice, 1st time passed the 2nd peak, and 2nd time passed the shifted 2nd peak. GUA3-1a was heated a 1st time up to the supercooled liquid, and a 2nd time passed the 2nd Cp peak. Note the higher amplitude sharp Cp peaks for GUA1-f -g, and GUA3-1a-c (see arrows in a and b). The chronology of the heatings is identified on the curves.

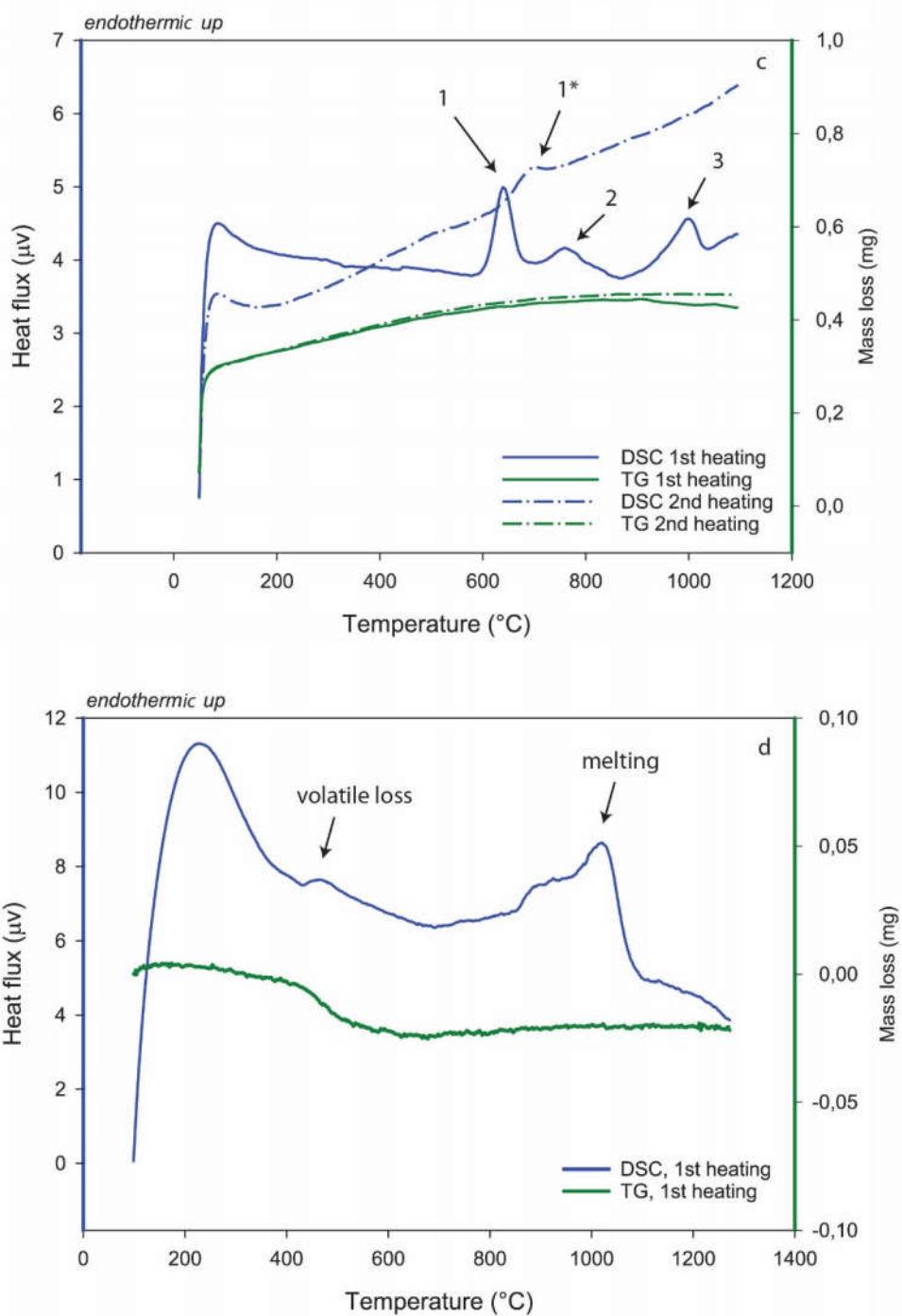


Figure 4.9 (continued) Calorimetry (DSC) and thermogravimetry (TG). Baseline has been subtracted from measurements. (c) Heat flux and mass loss for the obsidian in sample GUA3. Upon 1st heating, we observe 3 peaks. Peaks 1 and 2 are the same peaks observed in all Cp curves from Fig. 4.9a, b. 2nd heating shows only one peak (1*). Mass loss <0.05 wt%. (d) Heat flux and mass loss during first heating of the green phase in sample GUA3. Peak 1 relates to volatile loss and amounts to ca. 0.1 wt%, as evidenced by mass loss on green curve at ca. 400 $^{\circ}\text{C}$. The heat flux peak at ca. 1000 $^{\circ}\text{C}$ is due to melting of crystalline phases.

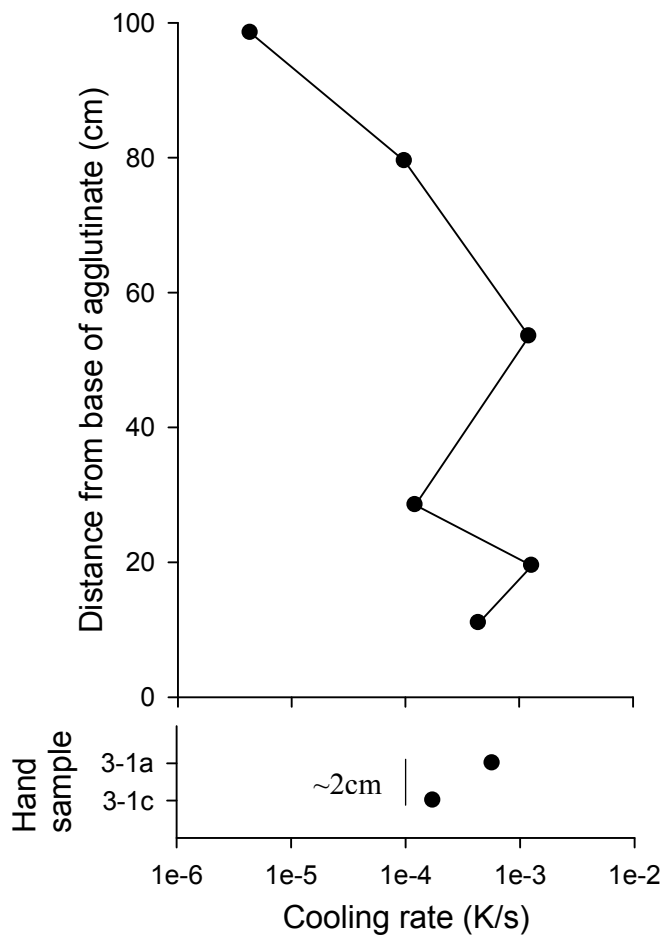
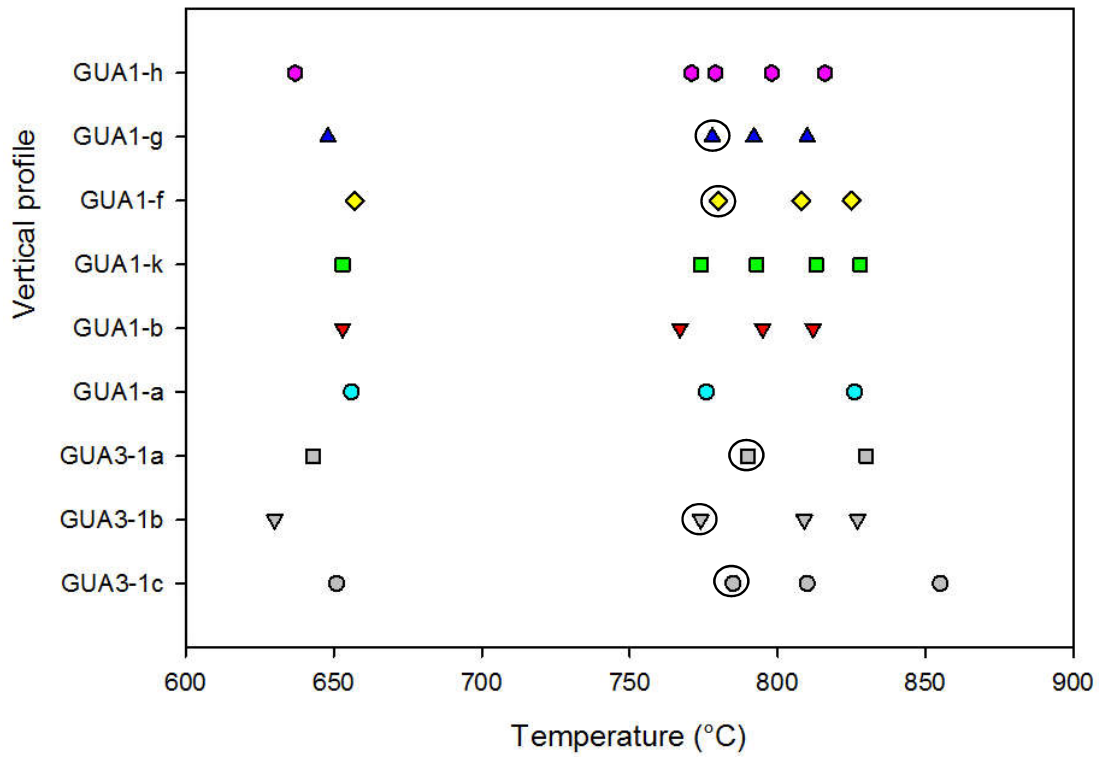


Figure 4.10 (a) Peak glass transition temperatures for the first C_p peak and following C_p peaks for the natural C_p curves obtained upon heating of glasses from the vertical profile and hand sample within the glassy lower part of Facies 1 at Guajara Peak. Circles denote sharp high amplitude C_p peaks as opposed to smaller low amplitude C_p peaks. (b) Cooling rates along the vertical profile and within hand sample. Cooling rates decrease by up to almost three orders of magnitude toward the top of the profile.

4.7 Discussion

4.7.1 Significance of Multiple Heat Capacity Peaks

The presence of additional endothermal C_p peaks at temperatures higher than the first endothermal C_p peak in the glass transition interval for the glass contained in Facies 1 may allow us to set tighter constraints on the melt properties and shed light on the eruptive and emplacement processes.

We used Giordano's model (Giordano et al., 2008) to calculate glass transition temperatures of phonolites with various Na_2O , K_2O and H_2O content while keeping all other oxides constant (Table 4.3). Because the water content estimated for Facies 1 is <0.05 wt%, we set the water content to 0.05 wt%. The calculated $T_{g_{onset}}$ of 596 °C is 29 °C below to 7 °C above the experimental $T_{g_{onset}}$, and GUA3-1b lies 68 °C below the calculated $T_{g_{onset}}$. The average experimental $T_{g_{onset}}$, is 571 °C, which is 25 °C below the calculated $T_{g_{onset}}$. If we set the water content to 0 wt%, the calculated $T_{g_{onset}}$ of 613 °C is 24 to 46 °C above the experimental $T_{g_{onset}}$. The average experimental $T_{g_{onset}}$ is 576 °C (excluding GUA3-1b), which is 37 °C below the calculated $T_{g_{onset}}$. Based on these $T_{g_{onset}}$ comparisons, we can conclude that there is a significant difference between the calculated $T_{g_{onset}}$ for 0.05 wt% water, the obsidian's measured water content, and the experimental $T_{g_{onset}}$. However, for the purpose of testing whether the additional C_p peaks can be caused due to compositional variations in the glass, the relative accuracy of the model for predicting viscosity of the Guajara glass is sufficient.

The range of compositions measured for the Facies 1 phonolitic obsidian could not entirely explain the additional C_p peaks, which are over 114 °C above the experimental $T_{g_{peak}}$. An enrichment or depletion in K, Na and/or H_2O could only explain a maximum $T_{g_{onset}}$ difference of ca. 80 °C (Table 4.3), that is, for a water content difference of 0.2 wt%. If the water content remains 0 wt% for a varying composition, the difference in $T_{g_{onset}}$ is ca. 30 °C. The crystallization of spherulites during or after emplacement of the deposit could locally change the composition of the glass, but not enough to change C_p to the extent of creating over 114 °C glass transition temperature differences.

Moreover, T_g differences could not be attributed to the presence of pyroclastic material of similar geochemical composition that has cooled rapidly and not been thermally annealed. A first heating of the glass above glass transition would erase the memory of the glass, such that the eruptive glassy structural properties of the glass would completely relax, and a subsequent heating would produce C_p curves with only one glass transition C_p peak, representative of one uniform major-element composition of the glass, as is the case here. Crystallization is an exothermal process, which cannot explain the second C_p peak. However, we suggest that

Table 4.2 Modeling parameters for the estimation of cooling rates following the TNM modeling approach. Additional C_p peaks in bold correspond to sharp, higher amplitude and wider peaks compared to the additional C_p peaks of the other samples.

| Sample | Corrected rate (K s ⁻¹) | T _{g onset} (°C) nat.curve | T _{g onset} (°C) 10-10 | T _g 1st pk (°C) nat.curve | Add. Peaks (°C) | T _{sl} (°C) | T _f (°C) | ΔH | x | β | A |
|---------|-------------------------------------|-------------------------------------|---------------------------------|--------------------------------------|----------------------|----------------------|---------------------|--------|------|------|----------|
| GUA1a | 4.4x10 ⁻⁴ | 617 | 589 | 656 | 776, 826 | 699 | 494 | 311185 | 0.77 | 0.88 | 1.28E-16 |
| GUA1b | 1.3x10 ⁻³ | 612 | 577 | 653 | 767, 795, 812 | 690 | 504 | 302938 | 0.74 | 0.85 | 3.37E-16 |
| GUA1k | 1.2x10 ⁻⁴ | 613 | 581 | 653 | 774, 793, 813, 828 | 693 | 478 | 307990 | 0.84 | 0.93 | 2.22E-16 |
| GUA1f | 1.2x10 ⁻³ | 620 | 574 | 657 | 780, 808, 825 | 693 | 505 | 305664 | 0.71 | 0.86 | 2.50E-16 |
| GUA1g | 9.9x10 ⁻⁵ | 600 | 573 | 648 | 778, 792, 810 | 685 | 492 | 389430 | 0.77 | 0.66 | 2.38E-21 |
| GUA1h | 4.35x10 ⁻⁶ | 591 | 576 | 637 | 771, 779, 798, 816 | 690 | 423 | 365786 | 0.66 | 0.53 | 1.12E-20 |
| GUA3-1a | 5.75x10 ⁻⁴ | 602 | 567 | 643 | 790, 830 | 695 | 501 | 328337 | 0.82 | 0.95 | 8.93E-18 |
| GUA3-1b | - | 588 | 528 | 630 | 774, 809, 827 | 668 | 462 | - | - | - | - |
| GUA3-1c | 1.73x10 ⁻⁴ | 611 | 574 | 651 | 785, 810, 855 | 691 | 500 | 357238 | 0.84 | 0.85 | 2.90E-19 |

Table 4.3 Onset glass transition temperatures ($T_{g onset}$) calculated for ca. 10 K.min⁻¹ cooling rate with the Giordano et al. (2008) model for the compositions representative of the range found in the Facies 1 glass. The estimated H₂O content is 0.05 wt% but we tested the effect of having no H₂O at all, 0.05 and 0.2 wt% H₂O. It has been shown that the greatest effect of H₂O on lowering the viscosity occurs for 0.1 wt% H₂O and that a higher H₂O content lowers viscosity, but to a lower extent. The lowest $T_{g onset}$ calculated is 558 °C and the highest $T_{g onset}$ is 641 °C, with a difference of 83 °C.

| | Guajara glass | | | High-Na Low-K | | | Low Na High-K | | |
|---------------------------|---------------|------|------|---------------|-------|-------|---------------|------|------|
| Na ₂ O (wt%) | 9.88 | 9.88 | 9.88 | 10.95 | 10.95 | 10.95 | 6.91 | 6.91 | 6.91 |
| K ₂ O (wt%) | 5.35 | 5.35 | 5.35 | 2.08 | 2.08 | 2.08 | 8.55 | 8.55 | 8.55 |
| H ₂ O (wt%) | 0 | 0.05 | 0.2 | 0 | 0.05 | 0.2 | 0 | 0.05 | 0.2 |
| T _{g onset} (°C) | 613 | 596 | 558 | 625 | 608 | 570 | 641 | 624 | 585 |

crystallization does occur at T between the 2nd and 3rd Cp peak (Figure 4.9c) and we attribute the 3rd Cp peak at ca. 1000 °C to the melting of spherulites, that were already present in the glass before measurements were performed, and/or new crystalline phases, the obsidian being originally near aphyric.

We also consider phase transformations. However, because the crystal content of the glasses is very low, a crystal phase transformation would hardly be noticeable on the Cp trace. In addition, temperatures at which the 2nd Cp peak occurs change to higher temperatures with successive heat treatments (Figure 4.9b) whereas phase transformations occur at fixed temperatures. This explanation for the 2nd Cp peaks is thus also excluded. As for the release of volatiles or vesiculation, thermogravimetry analyses of two samples reveal a volatile loss of <0.05 wt%. We can conclude that the release of volatiles is not responsible for the presence of the 2nd Cp peak.

Variations in the iron oxidation state of the obsidian is the most likely explanation for the existence of a 2nd Cp peak (Bouhifd et al., 2004; Kremers et al., 2012; Liebske et al., 2003b). It has been suggested, as discussed briefly in Chapter 3, Section 6.6, that variable oxidation states within single pyroclasts of uniform composition are produced during Strombolian eruptions, and possibly during other types of eruptions. The spread in oxidation states can be due to the mingling of (a) freshly erupted material that falls back into the eruptive vent, (b) partly crystallized magma that resides in a shallow reservoir long enough to oxidize the material, (c) new magma batch rising up in the volcanic conduit into the shallow reservoir, (d) assimilation of xenoliths in the magma chamber or volcanic conduit, or (e) the viscous densification of hot pyroclasts originating from different eruptive conditions. Therefore, we propose that variations in the iron oxidation state of the obsidian explain the 2nd Cp peak. The 1st Cp peak is associated with a reduced magma and the 2nd Cp peak, with a more oxidized magma.

4.7.2 Main Components of the Deposit

Pumice fragments and shards in the green phase underwent viscous deformation, leading to flattening, welding, and the formation of eutaxitic texture. We observe fiamme and flattened shards in the green phase. The foliation formed by the aligned fiamme and flattened shards is folded and is observed in the form of crenulations possibly due to the difference in competence between the rigid lithic clasts and the surrounding still hot pyroclastic material during compaction and welding (Branney et al., 1992). The lithics cannot accommodate shear strain as readily and therefore the material around them deforms viscously to accommodate the strain. We do not observe evidence of sag structures that would be due to the impact of ballistics. The folding occurred most likely in the pressure shadows of the lithic clasts. The presence of subrounded to rounded vesicles in the green phase points to the exsolution of still- or re-dissolved volatiles and re-vesiculation of the glass during devitrification (Branney and Kokelaar, 1992; Mahood, 1984; Schmincke, 1974; Smith, 1960).

Textural field observations, such as light-brown bands defining elliptical shapes in the obsidian, could be agglutinated and partly coalesced former melt droplets and spatter. The size of the spatter is not clear where spatter clast outlines are obliterated. It is however not excluded that these textures are the product of viscous melt rheomorphism. The suggestion that the iron oxidation state of the obsidian is variable, has implications for the rheology of the melt (now obsidian). Reduced melt has a lower viscosity than more oxidized melt, which could produce shear strain in the melt. We can speculate that the more oxidized glass is the result of pumice or green phase assimilation, or alternatively that the differences stem from processes that occurred before or during the eruption.

Our interpretation is different from that suggested by Bryan (1998), who attributed the presence of the green phase to the partial hydration and devitrification of an otherwise homogeneous spatter agglutinate. We do not exclude that the green phase was affected by the deposition of a water-rich deposit above, but the effect was rather limited given its relatively low water content (ca. 0.1 wt%). We propose an emplacement history that includes these four different phases: pumiceous ash, pumice lapilli, lithic clasts and possibly spatter.

4.7.3 Emplacement

Facies 1 has been interpreted to be the result of a pyroclastic fallout deposit composed mostly of spatter. However, in the light of the current evidence, we favor emplacement as a pyroclastic density current. It is unlikely that a pyroclastic fall could retain sufficient heat and produce the observed textures. We realize that the apparent limited lateral extent of the deposit challenges this idea, but the suggestion of a flow deposit should be considered. We propose a chronology of processes that occurred during emplacement as follows:

- (1) Pumiceous ash, pumice clasts, lithic clasts and possibly spatter were transported and deposited in a hot and viscous state.
- (2) The juvenile clasts welded through viscous densification and load compaction, and micro-folding occurred, which formed crenulations, possibly due to the presence of lithic clasts. The cooling rate decay can be approximated to be linear as the melt approaches the upper limit of the glass transition.
- (3) The welded and crenulated pumiceous ash started to devitrify above the glass transition and the devitrified material was sheared simultaneously. This suggests that the surrounding hot material behaved viscously, was sheared, and likely partly coalesced, as devitrification took place. Fragments of welded material eventually detached. The shape of the detached fragments suggests that the brittle deformation occurred mostly along crenulation surfaces. Brecciated obsidian at the base of Facies 1 represents evidence of brittle behavior in response to shear strain. Shearing could have been due to rheomorphism after deposition, or simply due to the slowing of the flow before it stopped. As mentioned above, it remains a possibility that the deposit consisted almost

entirely of pumiceous ash that viscously densified to form a homogeneous melt. It has been shown that for particles of similar composition and viscosity, particles of smaller grain size will weld more quickly (Wadsworth et al., 2014). Similar observations have been made in high-grade ignimbrites from the Yellowstone-Snake River Plane, in which horizons of spherulites in vitrophyre occur in many deposits. The proportion decreases downward within the vitrophyre (Andrews et al., 2008).

- (4) The devitrified welded ash and the melt cooled and crossed the glass transition. The melt cooled at a sufficiently high rate to inhibit crystallization. The welded ash possibly continued to devitrify below the glass transition. Cooling rate estimates are higher at the base of Facies 1 (10^{-3} K s^{-1}) and decrease toward the middle of Facies 1 (10^{-6} K s^{-1}), which would explain the upward increase in devitrification and support the chronology of processes suggested. A small-scale fault observed in the obsidian did not disturb the welded ash. The faulting of the obsidian and resulting deformation without any subsequent viscous flow evidence indicates that the fracturing occurred likely below or at the boundary of the glass transition. There is no sign of deformation in the welded ash, possibly because the fracturing event was followed by further devitrification. Numerical simulations of spherulite nucleation and growth, which is a process of devitrification, combined with geochemical data and geospeedometry, show that nucleation can start within the glass transition range and that growth can progress at temperatures below the glass transition (Befus et al., 2015).

This new interpretation opens the door to a correlation between the proximal GWU deposits and the distal Bandas del Sur deposits, which are non-welded pyroclastic deposits that have been emplaced closer to the coast.

Thermal annealing possibly lowered the calculated cooling rates, but the effect is not as remarkable as for the pantellerites of Chapter 3. The emplacement of Facies 2, a non-welded pumice bed, relatively quickly after the emplacement of Facies 1 may have insulated the deposit and may have slowed down the cooling process (Bagdassarov and Dingwell, 1994).

5

Outlook

The studies discussed in the previous chapters helped to shed light on some aspects of the complex processes and interplay of various parameters during volcanic eruptions, or to be more specific during magma fragmentation and the eruption and emplacement of volcanoclastic deposits. However these investigations also posed new or follow-up questions and demonstrated the need of refinement of measuring methods, which should be mentioned here.

Chapter 2 focused on testing the influence of outgassing on the magma fragmentation speed. A number of additional studies could contribute greatly to the understanding of all the processes that are involved. The interpretations that were proposed in this chapter are based on a rather qualitative analysis of the fluid dynamics associated with outgassing that occurs during magma fragmentation and a few points would be worth exploring in more detail:

- *Forchheimer number*: The determination of the Forchheimer number for each of our sample sets as was performed by Rust and Cashman (2004) could confirm our interpretations regarding gas flow rates inside sample cylinders at high pressures.

- *3-D bubble network characterization*: Although the two basic types of textures presented in this study are sufficient to explain the differences in fragmentation speeds observed, a detailed description and quantification of the bubble network of each sample set could shed light on the complexity of gas flow paths and on the main factors responsible for differences in gas flow rates. This would allow to refine interpretations, but would require a high resolution 3-D characterization in order to detect the possibly very narrow apertures between bubbles.
- *Numerical simulations of suction force reduction*: The suggestions that outgassing reduces the suction force between the sample cylinder and the fragmented layer at the fragmentation front and that the gas flow may reach supersonic speeds should be tested numerically.
- *Fragmentation layer thickness*: Grain size distribution analyses of the pyroclasts resulting from fragmentation speed experiments with high-permeability dome/conduit wall rocks and high-permeability pumice could help to constrain the thickness of the fragmentation layer as well as the steepness of the pressure gradient at the scale of the fragmentation layer.

Chapters 3 and 4 focused on characterizing volcanoclastic deposits and setting some constraints on their emplacement by using cooling rate data combined with field geological relationships, and textural and geochemical data. However, a complete understanding of these complex deposits requires further studies. Key aspects that should be studied comprise:

- *Interpretation of heat capacity peaks, especially with regards to the iron oxidation state of melt*: Several peaks and troughs are observed on heat capacity curves, which contain precious information. Including the iron oxidation state in models that calculate viscosity and glass transition temperatures is critical, especially to the understanding of peralkaline melts. For a fixed temperature and melt composition, oxygen fugacity conditions, which depend on the intrusive and eruptive history, dictate the iron oxidation state of a melt. It is only in the last decade that scientists started to evaluate the effect of the iron oxidation state on the viscosity and glass transition temperature of natural magmatic liquids. Whether a melt is reduced or more oxidized has great implications for melt rheology and emplacement processes of deposits.
- *Accuracy of the method*: This dissertation showed that enthalpy relaxation geospeedometry provides useful insights into the cooling process of glassy deposits. However, there is a need to refine the DSC data processing method to increase the accuracy of the measurements and cooling rate estimates in order to eliminate the extra correction of 0.3 log unit. The magnitude of thermal gradients in samples and the response of the instrument's furnace during heating and cooling should be evaluated. More importantly, it may be necessary to review the TNM model and attempt to reproduce the C_p calibration and natural curves with even more accuracy. In any case, a Matlab code could enable the estimation of cooling rates efficiently.

- *Thermal annealing*: The cooling history of glasses is sometimes obscured by thermal annealing. Calculated cooling rates may be underestimated by as much as 3 orders of magnitude. There is a need to develop a guide that would help scientists differentiate in the field and in the laboratory, using a series of test measurements, between glasses that have been affected by thermal annealing, and which have not. However, this is not a trivial task and whether it can be done is questionable.
- *Dimensions and lateral extent of deposit*: Facies 1 of the Guajara Welded Unit was likely emplaced as a flow, which welded and flowed rheomorphically for a short distance. A detailed mapping along the whole thickness of Facies 1 as well as geochemical analyses and microscopic textural analyses are necessary to test the suggested interpretation. The presence of devitrified welded ash dispersed in the obsidian is intriguing and it would be necessary to return to the Guajara Formation with a fresh eye. Lithological contacts with Facies 1 should be re-evaluated and Facies 1 should be traced around Guajara Peak to reassess the extent and thickness variations of Facies 1, as well as kinematic indicators, just in case there are clues that have gone unnoticed. A key point to the interpretation of the deposit is the lateral evolution of the deposit. It would be interesting to look for a lithology similar to the green phase, composed mainly of welded ash, in the proximity of the deposit. A relationship could be established between the two deposits.
- *Eruptive temperature*: The eruptive temperature of pantellerites and phonolites is poorly constrained and has been estimated using geothermometers. Experimental studies that would establish the *P-T* stability fields of the mineral phases found in these magmas, as well as rheology experiments simulating the fragmentation and/or flow (possibly even reproducing viscous heating) of these exceptional magmas would provide constraints on the possible emplacement processes given the specific conditions of an eruption.
- *Geochemical composition*: Vertical and lateral geochemical profiles of major and trace elements, as well as of halogens could confirm the origin of the main components of Facies 1 and its mode of emplacement. Similar analyses for the Tramontana rheomorphic spatter-fed deposit could provide details on the aggradation of the hot-melt layers.

Bibliography

- Ablay, G. J., and Marti, J., 2000, Stratigraphy, structure, and volcanic evolution of the Pico teide-Pico Viejo formation, Tenerife, Canary Islands: *Journal of volcanology and geothermal research*, v. 103, p. 175-208.
- Adams, L. H., and Williamson, E. D., 1920, Annealing of glass: *J. Franklin Inst.*, v. 190, p. 597-631 and 835-870.
- Alatorre-Ibargüengoitia, M. A., Scheu, B., and Dingwell, D. B., 2011, Influence of the fragmentation process on the dynamics of Vulcanian eruptions: An experimental approach: *Earth and Planetary Science Letters*, v. 302, p. 51-59.
- Alatorre-Ibargüengoitia, M. A., Scheu, B., Dingwell, D. B., Delgado-Granados, H., and Taddeucci, J., 2010, Energy consumption by magmatic fragmentation and pyroclast ejection during Vulcanian eruptions: *Earth and Planetary Science Letters*, v. 291, no. 1-4, p. 60-69.
- Alidibirov, M., and Dingwell, D. B., 1996a, An experimental facility for the investigation of magma fragmentation by rapid decompression: *Bulletin of Volcanology*, v. 58, no. 5, p. 411-416.
- , 1996b, Magma fragmentation by rapid decompression: *Nature*, v. 380, no. 6570, p. 146-148.
- Alidibirov, M., and Dingwell, D. B., 2000, Three fragmentation mechanisms for highly viscous magma under rapid decompression: *Journal of volcanology and geothermal research*, v. 100, no. 1-4, p. 413-421.
- Alidibirov, M. A., 1994, A model for viscous magma fragmentation during volcanic blasts: *Bulletin of Volcanology*, v. 56, no. 6-7, p. 459-465.
- Ancochea, E., Fuster, J. M. a., Ibarrola, E., Cendrero, A., Coello, J., Hernan, F., Cantagrel, J. M., and Jamond, C., 1990, Volcanic evolution of the island of Tenerife (Canary Islands) in the light of new K-Ar data: *Journal of Volcanology and Geothermal Research*, v. 44, no. 3-4, p. 231-249.
- Ancochea, E., Huertas, M. J., Cantagrel, J. M., Coello, J., FÃster, J. M., Arnaud, N., and Ibarrola, E., 1999, Evolution of the Canadas edifice and its implications for the origin of the Canadas Caldera (Tenerife, Canary Islands): *Journal of Volcanology and Geothermal Research*, v. 88, no. 3, p. 177-199.
- Andrews, G. D. M., Branney, M. J., Bonnicksen, B., and McCurry, M., 2008, Rhyolitic ignimbrites in the rogerson graben, southern snake river plain volcanic province: Volcanic stratigraphy, eruption history and basin evolution.: *Bulletin of Volcanology*, v. 70, no. 3, p. 269-291.
- Angell, C. A., 1985, Strong and fragile liquids, *in* Ngai, K. L., Wright, G.B., ed., *Relaxations in complex systems*: Springfield, National Technical Information Service, U.S. Department of Commerce, p. 345.
- Arana, V., 1971, *Litolgia y estructura del Edificio Canadas*, Tenerife: *Estudios Geologicos*, v. 27, p. 95-135.
- Baasner, A., Schmidt, B. C., and Webb, S. L., 2013, Compositional dependence of the rheology of halogen (F, Cl) bearing aluminosilicate melts: *Chemical Geology*, v. 346, no. 0, p. 172-183.
- Bagdassarov, N., and Dingwell, D., 1994, Thermal-Properties Of Vesicular Rhyolite: *Journal of Volcanology and Geothermal Research*, v. 60, no. 2, p. 179-191.

- Bear, J., 1972, Dynamics of fluids in porous media, New York, Dover Publications Inc., 764 p.:
- Befus, K. S., Watkins, J., Gardner, J. E., Richard, D., Befus, K. M., Miller, N. R., and Dingwell, D. B., 2015, Spherulites as in-situ recorders of thermal history in lava flows.: *Geology*.
- Bouhifd, M. A., Richet, P., Besson, P., Roskosz, M., and Ingrin, J., 2004, Redox state, microstructure and viscosity of a partially crystallized basalt melt: *Earth and Planetary Science Letters*, v. 218, no. 1-2, p. 31-44.
- Branney, M. J., and Kokelaar, B. P., 1992, A reappraisal of ignimbrite emplacement: progressive aggradation and changes from particulate to non-particulate flow during emplacement of high-grade ignimbrite.: *Bulletin of Volcanology*, v. 54, p. 504-520.
- Branney, M. J., Kokelaar, B. P., and McConnell, B. J., 1992, The Bad Step Tuff: a lava-like rheomorphic ignimbrite in a calc-alkaline piecemeal caldera, English Lake District: *Bulletin of Volcanology*, v. 54, p. 187-199.
- Brown, R. J., Barry, T. L., Branney, M. J., Pringle, M. S., and Bryan, S. E., 2003, The Quaternary pyroclastic succession of southeast Tenerife, Canary Islands: explosive eruptions, related caldera subsidence, and sector collapse: *Geological Magazine*, v. 140, no. 3, p. 265-288.
- Bryan, S., E., 1998, Volcanology and Petrology of the Granadilla Member, Tenerife, (Canary Islands): Constraints on the eruption dynamics, ignimbrite emplacement and caldera evolution.: Australia, University of Queensland, unpublished thesis.
- Bryan, S. E., Marti, J., and Cas, R. A. F., 1998, Stratigraphy of the Bandas del Sur Formation: an extracaldera record of Quaternary phonolite explosive eruptions from the Las Canadas edifice, Tenerife (Canary Islands). *Geological Magazine*, v. 135, p. 605-636.
- Burgisser, A., and Gardner, J. E., 2004, Experimental constraints on degassing and permeability in volcanic conduit flow: *Bulletin of Volcanology*, v. 67, no. 1, p. 42-56.
- Butler, R. W. H., Grasso, M., and Lamanna, F., 1992, Origin And Deformation Of The Neogene Recent Maghrebien Foredeep At The Gela Nappe, Se Sicily: *Journal of the Geological Society*, v. 149, p. 547-556.
- Carman, P. C., 1956, Flow of gases through porous media, New York, Academic Press, 182 p.:
- Carmichael, I. S. E., 1967, The iron-titanium oxides of salic volcanic rocks and their associated ferromagnesian silicates: *Contributions to Mineralogy and Petrology*, v. 14, p. 36-64.
- Castro, J. M., Beck, P., Tuffen, H., Nichols, A. R. L., Dingwell, D. B., and Martin, M. C., 2008, Timescales of spherulite crystallization in obsidian inferred from water concentration profiles: *American Mineralogist*, v. 93, no. 11-12, p. 1816-1822.
- Catalano, S., De Guidi, G., Lanzafame, G., Monaco, C., and Tortorici, L., 2009, Late Quaternary deformation on the island on Pantelleria: New constraints for the recent tectonic evolution of the Sicily Channel Rift (southern Italy): *Journal of Geodynamics*, v. 48, no. 2, p. 75-82.
- Civetta, L., Cornette, Y., Gillot, P. Y., and Orsi, G., 1988, The eruptive history of Pantelleria (Sicily Channel) in the last 50 Ka: *Bulletin of Volcanology*, v. 50, no. 1, p. 47-57.
- Cornette, Y., Crisci, G. M., Gillot, P. Y., and Orsi, G., 1983, Recent Volcanic History Of Pantelleria - A New Interpretation: *Journal of Volcanology and Geothermal Research*, v. 17, no. 1-4, p. 361-373.
- D'Oriano, C., Poggianti, E., Bertagnini, A., Cioni, R., Landi, P., Polacci, M., and Rosi, M., 2005, Changes in eruptive style during the AD 1538 Monte Nuovo eruption (Phlegrean Fields, Italy): the role of syn-eruptive crystallization: *Bulletin of Volcanology*, v. 67, no. 7, p. 601-621.

- D'Oriano, C., Pompilio, M., Bertagnini, A., Cioni, R., and Pichavant, M., 2013, Effects of experimental reheating of natural basaltic ash at different temperatures and redox conditions: *Contributions to Mineralogy and Petrology*, v. 165, no. 5, p. 863-883.
- Debolt, M. A., Easteal, A. J., Macedo, P. B., and Moynihan, C. T., 1976, Analysis of Structural Relaxation in Glass Using Rate Heating Data: *Journal of the American Ceramic Society*, v. 59, no. 1-2, p. 16-21.
- Degruyter, W., Bachmann, O., Burgisser, A., and Manga, M., 2012, The effects of outgassing on the transition between effusive and explosive silicic eruptions: *Earth and Planetary Science Letters*, v. 349-350, no. 0, p. 161-170.
- Di Genova, D., Romano, C., Giordano, D., and Alletti, M., 2014, Heat capacity, configurational heat capacity and fragility of hydrous magmas: *Geochimica et Cosmochimica Acta*, v. 142, p. 314-333.
- Dingwell, D. B., 1996, Volcanic dilemma: Flow or blow?: *Science*, v. 273, no. 5278, p. 1054-1055.
- Dingwell, D. B., and Hess, K. U., 1998, Melt viscosities in the system Na-Fe-Si-O-F-Cl: Contrasting effects of F and Cl in alkaline melts: *American Mineralogist*, v. 83, no. 9-10, p. 1016-1021.
- Dingwell, D. B., Hess, K. U., and Romano, C., 1998, Extremely fluid behavior of hydrous peralkaline rhyolites: *Earth and Planetary Science Letters*, v. 158, no. 1-2, p. 31-38.
- Dingwell, D. B., Webb, S. L., 1990, Relaxation in silicate melts: *European Journal of Mineralogy*, v. 2, p. 427-449.
- Duffield, W. A., 1990, Eruptive fountains of silicic magma and their possible effects on the tin content of fountain-fed lavas, Taylor Creek Rhyolite, New Mexico, *in* Stein, H. J., and Hannah, J. L., eds., *Ore-bearing granite systems: petrogenesis and mineralizing processes*, Volume 246, Geological Society of America Special Paper, p. 251-261.
- Dullien, F. A. L., 1992, *Porous Media- Fluid Transport and Pore Structure*, San Diego, Academic Press, 574 p.:
- Ekren, E. B., McIntyre, D. H., and Bennett, E. H., 1984, High-temperature, large-volume, lavalike ash-flow tuffs without calderas in southwestern Idaho United States *Geological Survey professional paper*, v. 1272, p. 82.
- Forchheimer, P., 1901, Water movement through the ground: *Zeitschrift Des Vereines Deutscher Ingenieure*, v. 45, p. 1781-1788.
- Förstner, H., 1881, Nota preliminare sulla geologia dell'Isola di Pantelleria secondo gli studii fatti negli anni 1874 e 1881.: *Boll. R. Com. Geol. Italia*, v. 12, p. 523.
- , 1884, Über die Feldspäthe von Pantelleria.: *Zeits. Kryst. Min.*, v. 8, p. 125.
- Fowler, A. C., Scheu, B., Lee, W. T., and McGuinness, M. J., 2010, A theoretical model of the explosive fragmentation of vesicular magma: *Proceedings of the Royal Society A: Mathematical, Physical and Engineering Sciences*, v. 466, no. 2115, p. 731-752.
- Freundt, A., and Schmicke, H.-U., 1995, Lithic-enriched segregation bodies in pyroclastic flow deposits of Laacher See Volcano (East Eifel, Germany): *Journal of Volcanology and Geothermal Research*, v. 25, p. 193-224.
- Gardner, J. E., Befus, K. S., Watkins, J., Hesse, M., and Miller, N., 2012, Compositional gradients surrounding spherulites in obsidian and their relationship to spherulite growth and lava cooling: *Bulletin of Volcanology*, v. 74, p. 1865-1879.
- Gimeno, D., Diaz, N., Garcia-Valles, M., and Martinez-Manent, S., 2003, Genesis of bottom vitrophyre facies in rhyolitic pyroclastic flows: a case study of syneruptive glass welding (Nuraxi unit, Sulcis, SW Sardinia, Italy): *Journal of Non-Crystalline Solids*, v. 323, no. 1-3, p. 91-96.
- Giordano, D., Nichols, A. R. L., and Dingwell, D. B., 2005, Glass transition temperatures of natural hydrous melts: a relationship with shear viscosity and implications for the

- welding process: *Journal of Volcanology and Geothermal Research*, v. 142, no. 1-2, p. 105-118.
- Giordano, D., Russell, J. K., and Dingwell, D. B., 2008, Viscosity of magmatic liquids: A model: *Earth and planetary science letters*, v. 271, no. 1-4, p. 123-134.
- Goldstein, M., 1964, Phenomenological aspects of the glass transition, *in* Mackenzie, J. D., ed., *Modern aspects of the vitreous state*, Volume 3: London, Butterworths Scientific Publications Ltd.
- Goto, A., 1999, A new model for volcanic earthquake at Unzen Volcano: Melt rupture model: *Geophysical Research Letters*, v. 26, no. 16, p. 2541-2544.
- Gottsmann, J., and Dingwell, D. B., 2001a, Cooling dynamics of spatter-fed phonolite obsidian flows on Tenerife, Canary Islands: *Journal of Volcanology and Geothermal Research*, v. 105, no. 4, p. 323-342.
- , 2001b, The cooling of frontal flow ramps: a calorimetric study on the Rocche Rosse rhyolite flow, Lipari, Aeolian Islands, Italy: *Terra Nova*, v. 13, no. 3, p. 157-164.
- , 2002, The thermal history of a spatter-fed lava flow: the 8-ka pantellerite flow of Mayor Island, New Zealand: *Bulletin of Volcanology*, v. 64, no. 6, p. 410-422.
- Gottsmann, J., Harris, A. J. L., and Dingwell, D. B., 2004, Thermal history of Hawaiian pahoehoe lava crusts at the glass transition: implications for flow rheology and emplacement: *Earth and Planetary Science Letters*, v. 228, no. 3-4, p. 343-353.
- Grunder, A., and Russell, J. K., 2005, Welding processes in volcanology: insights from field, experimental, and modeling studies: *Journal of Volcanology and Geothermal Research*, v. 142, p. 1-9.
- Head, J. W., and Wilson, L., 1989, Basaltic Pyroclastic Eruptions - Influence of Gas-Release Patterns and Volume Fluxes on Fountain Structure, and the Formation of Cinder Cones, Spatter Cones, Rootless Flows, Lava Ponds and Lava Flows: *Journal of Volcanology and Geothermal Research*, v. 37, no. 3-4, p. 261-271.
- Heaney, P. J., 1994, Structure and Chemistry of the Low-Pressure Silica Polymorphs: Silica: Physical Behavior, Geochemistry and Materials Applications, v. 29, p. 1-40.
- Hess, K.-U., Cordonnier, B., Lavallée, Y., and Dingwell, D. B., 2008, Viscous heating in rhyolite: An in situ experimental determination: *Earth and Planetary Science Letters*, v. 275, no. 1-2, p. 121-126.
- Hess, K. U., Dingwell, D. B., and Webb, S. L., 1995, The Influence of Excess Alkalis on the Viscosity of a Haplogranitic Melt: *American Mineralogist*, v. 80, no. 3-4, p. 297-304.
- Hodge, I. M., Heslin, Robert, 2010, Effects of thermal history on enthalpy relaxation in glasses 7. Thermal time constants: *Journal of Non-Crystalline Solids*, v. 356, p. 1479-1487.
- Höhne, G. W. H., Hemminger, W.F., Flammersheim, H.-J., 2003, *Differential Scanning Calorimetry*, Berlin Heidelberg, Springer.
- Houghton, B. F., Wilson, C. J. N., and Weaver, S. D., 1985, The Ruru pass tephra, a peralkaline welded airfall tuff from Mayor Island: *N. Z. Geol. Surv. Rec.*, v. 8, p. 30-36.
- Ichihara, M., and Rubin, M. B., 2010, Brittleness of fracture in flowing magma: *Journal of Geophysical Research-Solid Earth*, v. 115, no. B12.
- Jaupart, C., and Allègre, C. J., 1991, Gas Content, Eruption Rate and Instabilities of Eruption Regime in Silicic Volcanos: *Earth and Planetary Science Letters*, v. 102, no. 3-4, p. 413-429.
- Kennedy, B., Spieler, O., Scheu, B., Kueppers, U., Taddeucci, J., and Dingwell, D. B., 2005, Conduit implosion during Vulcanian eruptions: *Geology*, v. 33, no. 7, p. 581-584.
- Klug, C., and Cashman, K. V., 1996, Permeability development in vesiculating magmas: Implications for fragmentation: *Bulletin of Volcanology*, v. 58, no. 2-3, p. 87-100.

- Knoche, R., Dingwell, D. B., Seifert, F. A., and Webb, S. L., 1994, Nonlinear Properties Of Supercooled Liquids In The System Na₂O-SiO₂: *Chemical Geology*, v. 116, no. 1-2, p. 1-16.
- Koyaguchi, T., and Mitani, N. K., 2005a, A theoretical model for fragmentation of viscous bubbly magmas in shock tubes: *Journal of Geophysical Research-Solid Earth*, v. 110, no. B10.
- , 2005b, A theoretical model for fragmentation of viscous bubbly magmas in shock tubes: *Journal of Geophysical Research-Solid Earth*, v. 110, no. B10, p. 1978–2012.
- Koyaguchi, T., Scheu, B., Mitani, N. K., and Melnik, O., 2008, A fragmentation criterion for highly viscous bubbly magmas estimated from shock tube experiments: *Journal of volcanology and geothermal research*, v. 178, no. 1, p. 58-71.
- Kozeny, J., 1927, Über kapillare Leitung des Wassers im Boden. , *Wien, Sitzungsber. Akad. Wiss.* , v. 136.
- Kremers, S., Lavallee, Y., Hanson, J., Hess, K.-U., Chevrel, M. O., Wassermann, J., and Dingwell, D. B., 2012, Shallow magma-mingling-driven Strombolian eruptions at Mt. Yasur volcano, Vanuatu: *Geophysical Research Letters*, v. 39.
- Lamb, S., 1945, *Hydrodynamics*: New York, Dover, p. 738.
- Langlois, W., 1964, *Slow viscous flow*: New York, MacMillan, p. 229.
- Lautze, N. C., and Houghton, B. F., 2005, Physical mingling of magma and complex eruption dynamics in the shallow conduit at Stromboli volcano, Italy: *Geology*, v. 33, no. 5, p. 425.
- Lavallée, Y., Wadsworth, F. B., Vasseur, J., Russell, J. K., Andrews, G. D. M., Hess, K.-U., von Aulock, F. W., Kendrick, J. E., Tuffen, H., Biggin, A., and Dingwell, D. B., 2015, Eruption and emplacement timescales of ignimbrite super-eruptions from thermo-kinetics of glass shards: *Frontiers in Earth Science*, v. 3.
- Le Bas, M. J., Le Maitre, R. W., Streckeisen, A., and Zanettin, B., 1986, A chemical classification of volcanic rocks based on the total alkali-silica diagram: *Journal of Petrology*, v. 27, p. 745-750.
- Liebske, C., Behrens, H., Holtz, F., and Lange, R. A., 2003a, The influence of pressure and composition on the viscosity of andesitic melts: *Geochimica et Cosmochimica Acta*, v. 67, no. 3, p. 473-485.
- Liebske, C., Behrens, H., Holtz, F. o., and Lange, R. A., 2003b, The influence of pressure and composition on the viscosity of andesitic melts: *Geochimica et Cosmochimica Acta*, v. 67, no. 3, p. 473-485.
- Liepmann, H. W., and Roshko, A., 1957, *Elements of Gas Dynamics*, New York, John Wiley & Sons.
- Lowenstern, J. B., 1994, Chlorine, Fluid Immiscibility, and Degassing in Peralkaline Magmas from Pantelleria, Italy: *American Mineralogist*, v. 79, no. 3-4, p. 353-369.
- MacDonald, R., 1974, Nomenclature and petrochemistry of the peralkaline oversaturated extrusive rocks: *Bulletin Volcanologique*, v. 38, no. 2, p. 498-516.
- Mahood, G., and Hildreth, W., 1983, Nested Calderas and Trapdoor Uplift at Pantelleria, Strait of Sicily: *Geology*, v. 11, no. 12, p. 722-726.
- Mahood, G. A., 1984, Pyroclastic rocks and calderas associated with strongly peralkaline magmatism: *Journal of Geophysical Research: Solid Earth*, v. 89, no. B10, p. 8540-8552.
- Mahood, G. A., and Hildreth, W., 1986, Geology of the peralkaline volcano at Pantelleria, Strait of Sicily: *Bulletin of Volcanology*, v. 48, p. 143-172.
- Marti, J., Hürlimann, M., and Ablay, G. J., 1997, Vertical and lateral collapses on Tenerife (Canary Islands) and other volcanic ocean islands.: *Geology*, v. 25, p. 879-882.

- Marti, J., Mitjavila, J., and Arana, V., 1994, Stratigraphy, structure and geochronology of the "Las Canadas Caldera" (Tenerife, Canary Islands). *Geological Magazine*, v. 131, p. 715-727.
- Mauro, J. C., Loucks, R. J., and Gupta, P. K., 2009, Fictive Temperature and the Glassy State: *Journal of the American Ceramic Society*, v. 92, no. 1, p. 75-86.
- Maxwell, J. C., 1867, On the dynamical theory of gases: *Philosophical Transactions of the Royal Society of London*, v. 157, p. 49-88.
- McBirney, A. R., and Murase, T., 1970, Factors governing the formation of pyroclastic rocks: *Bulletin of Volcanology*, v. 34, p. 372-384.
- McGuinness, M. J., Scheu, B., and Fowler, A. C., 2012, Explosive fragmentation criteria and velocities for vesicular magma: *Journal of Volcanology and Geothermal Research*, v. 237-238, no. 0, p. 81-96.
- Melnik, O., Barmin, A. A., and Sparks, R. S. J., 2005, Dynamics of magma flow inside volcanic conduits with bubble overpressure buildup and gas loss through permeable magma: *Journal of volcanology and geothermal research*, v. 143, no. 1-3, p. 53-68.
- Melnik, O., and Sparks, R. S. J., 2005, Controls on conduit magma flow dynamics during lava dome building eruptions: *Journal of Geophysical Research-Solid Earth*, v. 110, no. B2.
- Moynihan, C. T., 1995, Structural relaxation and the glass transition: *Structure, Dynamics and Properties of Silicate Melts*, v. 32, p. 1-19.
- Moynihan, C. T., Easteal, A. J., De Bolt, M. A., and Tucker, J., 1976a, Dependence of the Fictive Temperature of Glass on Cooling Rate: *Journal of the American Ceramic Society*, v. 59, no. 1-2, p. 12-16.
- Moynihan, C. T., Easteal, A. J., Debolt, M. A., and Tucker, J., 1976b, Dependence of Fictive Temperature of Glass on Cooling Rate: *Journal of the American Ceramic Society*, v. 59, no. 1-2, p. 12-16.
- Moynihan, C. T., Easteal, A. J., Wilder, J., and Tucker, J., 1974, Dependence of Glass-Transition Temperature on Heating and Cooling Rate: *Journal of Physical Chemistry*, v. 78, no. 26, p. 2673-2677.
- Moynihan, C. T., Lee, S. K., Tatsumisago, M., and Minami, T., 1996, Estimation of activation energies for structural relaxation and viscous flow from DTA and DSC experiments: *Thermochimica Acta*, v. 280-281, no. 0, p. 153-162.
- Mueller, S., Melnik, O., Spieler, O., Scheu, B., and Dingwell, D. B., 2005, Permeability and degassing of dome lavas undergoing rapid decompression; an experimental determination: *Bulletin of Volcanology*, v. 67, no. 6, p. 526-538.
- Mueller, S., Scheu, B., Spieler, O., and Dingwell, D. B., 2008, Permeability control on magma fragmentation: *Geology*, v. 36, no. 5, p. 399-402.
- Mysen, B., and Richet, P., 2005, *Silicate glasses and melts*, Elsevier Science.
- Narayanaswamy, O. S., 1971, A Model of Structural Relaxation in Glass: *Journal of the American Ceramic Society*, v. 54, no. 10, p. 491-498.
- Neave, D. A., Fabbro, G., Herd, R. A., Petrone, C. M., and Edmonds, M., 2012, Melting, Differentiation and Degassing at the Pantelleria Volcano, Italy: *Journal of Petrology*, v. 53, no. 3, p. 637-663.
- Nelson, S. T., and Montana, A., 1992, *American Mineralogist*, v. 77, no. 11-12, p. 1242-1249.
- Nicholls, J., Carmichael, I.S.E., 1969, Peralkaline acid liquids: A petrological study: *Contributions to Mineralogy and Petrology*, v. 20, p. 268-294.
- Orsi, G., Ruvo, L., and Scarpati, C., 1991, The Recent Explosive Volcanism at Pantelleria: *Geologische Rundschau*, v. 80, no. 1, p. 187-200.
- Orsi, G., and Sheridan, M. F., 1984, The Green Tuff of Pantelleria: Rheoignimbrite or rheomorphic fall?: *Bulletin Volcanologique*, v. 47, no. 3, p. 611-626.

- Palladino, D. M., and Simei, S., 2005, Eruptive dynamics and caldera collapse during the Onano eruption, Vulcini, Italy: *Bulletin of Volcanology*, v. 67, no. 5, p. 423-440.
- Papale, P., 1999, Strain-induced magma fragmentation in explosive eruptions: *Nature*, v. 397, no. 6718, p. 425-428.
- Perugini, D., Poli, G., and Prosperini, N., 2002, Morphometric analysis of magmatic enclaves: a tool for understanding magma vesiculation and ascent: *Lithos*, v. 61, no. 3-4, p. 225-235.
- Potuzak, M., Nichols, A. R. L., Dingwell, D. B., and Clague, D. A., 2008, Hyperquenched volcanic glass from Loihi Seamount, Hawaii: *Earth and Planetary Science Letters*, v. 270, no. 1-2, p. 54-62.
- Ridley, W. I., 1970, Petrology of Las-Canadas-Volcanoes, Tenerife, Canary-Islands: *Contributions to Mineralogy and Petrology*, v. 26, no. 2, p. 124-&.
- Ritland, H. N., 1956, Limitations of the fictive temperature concept: *Journal of the American Ceramic Society*, v. 39, no. 12, p. 403-406.
- Robert, G., Andrews, G. D. M., Ye, J. Y., and Whittington, A. G., 2013, Rheological controls on the emplacement of extremely high-grade ignimbrites: *Geology*, v. 41, no. 9, p. 1031-1034.
- Rust, A. C., and Cashman, K. V., 2004, Permeability of vesicular silicic magma: inertial and hysteresis effects: *Earth and Planetary Science Letters*, v. 228, no. 1-2, p. 93-107.
- , 2011, Permeability controls on expansion and size distributions of pyroclasts: *Journal of Geophysical Research-Solid Earth*, v. 116, no. B11.
- Ruth, D., and Ma, H. P., 1992, On the Derivation of the Forchheimer Equation by Means of the Averaging Theorem: *Transport in Porous Media*, v. 7, no. 3, p. 255-264.
- Saar, M. O., and Manga, M., 1999, Permeability-porosity relationship in vesicular basalts: *Geophysical Research Letters*, v. 26, no. 1, p. 111-114.
- Sahimi, M., 1994, *Applications of percolation theory*: London, Taylor and Francis, p. 300.
- Sanchez, M. C., Sarrionandia, F., Arostegui, J., Eguiluz, L., and Ibarguchi, J. I. G., 2012, The transition of spatter to lava-like body in lava fountain deposits: features and examples from the Cabezo Segura volcano (Calatrava, Spain): *Journal of Volcanology and Geothermal Research*, v. 227, p. 1-14.
- Sanchez, M. C., Sarrionandia, F., and Ibarguchi, J. I. G., 2014, Post-depositional intrusion and extrusion through a scoria and spatter cone of fountain-fed nephelinite lavas (Las Herrerias volcano, Calatrava, Spain): *Bulletin of Volcanology*, v. 76, no. 9, p. 17.
- Scherer, G. W., 1991, Glass formation and relaxation, *in* Zarzycki, J., ed., *Materials Science and Technology: Glasses and amorphous materials, Volume 9*: Weinheim, Germany, VCH, p. 119-173.
- Scheu, B., 2005, *Understanding silicic volcanism: constraints from elasticity and failure of vesicular magma* [Ph.D.: Ph.D. thesis, University of Munich].
- Scheu, B., Kueppers, U., Mueller, S., Spieler, O., and Dingwell, D. B., 2008, Experimental volcanology on eruptive products of Unzen volcano: *Journal of Volcanology and Geothermal Research*, v. 175, no. 1-2, p. 110-119.
- Scheu, B., Spieler, O., and Dingwell, D. B., 2006, Dynamics of explosive volcanism at Unzen volcano: an experimental contribution: *Bulletin of Volcanology*, v. 69, p. 175-187.
- Schmincke, H.-U., 1974, Volcanological aspects of peralkaline silicic welded ash-flow tuffs: *Bulletin Volcanologique*, v. 38, no. 2, p. 594-636.
- Smith, R. L., 1960, Zones and zonal variations in welded ash flows, *in* Survey, G., ed., *Short contributions to general geology*: Washington, United States Government Printing Office, p. 149-159.

- Soriano, C., Zafrilla, S., Marti, J., Bryan, S., Cas, R., and Ablay, G., 2002, Welding and rheomorphism of phonolitic fallout deposits from the Las Canadas caldera, Tenerife, Canary Islands: *Geological Society of America Bulletin*, v. 114, no. 7, p. 883-895.
- Sparks, R. S. J., 1978, Dynamics of Bubble Formation and Growth in Magmas - Review and Analysis: *Journal of Volcanology and Geothermal Research*, v. 3, no. 1-2, p. 1-37.
- Sparks, R. S. J., and Wright, J. V., 1979, Welded air-fall tuffs: *Geol. Soc. Amer. Spec. Paper*, v. 180, p. 155-166.
- Spieler, O., Dingwell, D. B., and Alidibirov, M., 2004a, Magma fragmentation speed: an experimental determination: *Journal of Volcanology and Geothermal Research*, v. 129, no. 1-3, p. 109-123.
- Spieler, O., Kennedy, B., Kueppers, U., Dingwell, D. B., Scheu, B., and Taddeucci, J., 2004b, The fragmentation threshold of pyroclastic rocks: *Earth and Planetary Science Letters*, v. 226, no. 1-2, p. 139-148.
- Stevenson, R. J., and Wilson, L., 1997, Physical volcanology and eruption dynamics of peralkaline agglutinates from Pantelleria: *Journal of Volcanology and Geothermal Research*, v. 79, no. 1-2, p. 97-122.
- Sumner, J. M., 1998, Formation of clastogenic lava flows during fissure eruption and scoria cone collapse: the 1986 eruption of Izu-Oshima Volcano, eastern Japan: *Bulletin of Volcanology*, v. 60, no. 3, p. 195-212.
- Sumner, J. M., Blake, S., Matela, R. J., and Wolff, J. A., 2005, Spatter: *Journal of Volcanology and Geothermal Research*, v. 142, no. 1-2, p. 49-65.
- Sumner, J. M., and Branney, M. J., 2002, The emplacement history of a remarkable heterogeneous, chemically zoned, rheomorphic and locally lava-like ignimbrite: 'TL' on Gran Canaria: *Journal of Volcanology and Geothermal Research*, v. 115, no. 1-2, p. 109-138.
- Tarbuck, E. J., and Lutgens, F. K., 2011, *Earth: An Introduction to Physical Geology*, Pearson Prentice Hall.
- Tool, A. Q., 1946, Relation Between Inelastic Deformability and Thermal Expansion of Glass in its Annealing Range: *Journal of the American Ceramic Society*, v. 29, no. 9, p. 240-253.
- Uhlmann, D. R., and Yinnon, H., 1983, Glass-forming systems, *Glass: Science and Technology*, Volume 1: New York, Academic Press, p. 1-47.
- Wadsworth, F. B., Vasseur, J., von Aulock, F. W., Hess, K. U., Scheu, B., Lavallee, Y., and Dingwell, D. B., 2014, Nonisothermal viscous sintering of volcanic ash: *Journal of Geophysical Research-Solid Earth*, v. 119, no. 12, p. 8792-8804.
- Wahl, F. M., Grim, R.E., Graf, R.B., 1961, Phase transformations in silica as examined by continuous x-ray diffraction: *The American Mineralogist*, v. 46, no. January-February, p. 196-208.
- Walker, G. P. L., 1983, Ignimbrite Types and Ignimbrite Problems: *Journal of Volcanology and Geothermal Research*, v. 17, no. 1-4, p. 65-88.
- White, J. C., Parker, D. F., and Ren, M., 2009, The origin of trachyte and pantellerite from Pantelleria, Italy: Insights from major element, trace element, and thermodynamic modelling: *Journal of volcanology and geothermal research*, v. 179, no. 1-2, p. 33-55.
- White, J. C., Ren, M. H., and Parker, D. F., 2005, Variation in mineralogy, temperature, and oxygen fugacity in a suite of strongly peralkaline lavas and tuffs, Pantelleria, Italy: *Canadian Mineralogist*, v. 43, p. 1331-1347.
- White, J. D. L., and Houghton, B. F., 2006, Primary volcaniclastic rocks: *Geology*, v. 34, no. 8, p. 677-680.

- Wilding, M., Webb, S., Dingwell, D., Ablay, G., and Marti, J., 1996a, Cooling rate variation in natural volcanic glasses from Tenerife, Canary Islands: *Contributions to Mineralogy and Petrology*, v. 125, no. 2-3, p. 151-160.
- Wilding, M., Webb, S., and Dingwell, D. B., 1996b, Tektite cooling rates: Calorimetric relaxation geospeedometry applied to a natural glass: *Geochimica et Cosmochimica Acta*, v. 60, no. 6, p. 1099-1103.
- Willcock, M. A. W., and Cas, R. A. F., 2014, Primary welding and crystallisation textures preserved in the intra-caldera ignimbrites of the Permian Ora Formation, northern Italy: implications for deposit thermal state and cooling history: *Bulletin of Volcanology*, v. 76, no. 6.
- Williams, G., and Watts, D. C., 1970, Non-symmetrical dielectric relaxation behaviour arising from a simple empirical decay function: *Transactions of the Faraday Society*, v. 66, no. 0, p. 80-85.
- Williams, R., Branney, M. J., and Barry, T. L., 2014, Temporal and spatial evolution of a waxing then waning catastrophic density current revealed by chemical mapping: *Geology*, v. 42, no. 2, p. 107-110.
- Wolff, J. A., and Sumner, J. M., 2000, Lava fountains and their products, *in* Sigurdson, H., ed., *Encyclopedia of Volcanoes*, Academic Press, p. 321-329.
- Wolff, J. A., Wright, J.V., 1980, Formation of the Green Tuff, Pantelleria: *Bulletin of Volcanology*, v. 44-4.
- Woods, A. W., 1995, A model of vulcanian explosions: *Nuclear Engineering and Design*, v. 155, no. 1, p. 345-357.
- Woods, A. W., and Koyaguchi, T., 1994, Transitions between Explosive and Effusive Eruptions of Silicic Magmas: *Nature*, v. 370, no. 6491, p. 641-644.
- Wright, H. M. N., Cashman, K. V., Gottesfeld, E. H., and Roberts, J. J., 2009, Pore structure of volcanic clasts: Measurements of permeability and electrical conductivity: *Earth and Planetary Science Letters*, v. 280, no. 1-4, p. 93-104.
- Ya, M., Deubener, J., and Yue, Y., 2008, Enthalpy and Anisotropy Relaxation of Glass Fibers: *Journal of the American Ceramic Society*, v. 91, no. 3, p. 745-752.
- Yue, Y. Z., Christiansen, J. d., and Jensen, S. L., 2002a, Determination of the fictive temperature for a hyperquenched glass: *Chemical Physics Letters*, v. 357, no. 1-2, p. 20-24.
- Yue, Y. Z., Jensen, S. L., and Christiansen, J. D., 2002b, Physical aging in a hyperquenched glass: *Applied Physics Letters*, v. 81, no. 16, p. 2983-2985.
- Zhang, Y. X., 1999, A criterion for the fragmentation of bubbly magma based on brittle failure theory: *Nature*, v. 402, no. 6762, p. 648-650.

Acknowledgements

What an adventure it has been, but I am thrilled it is finally coming to an end! Dear family, friends, colleagues and supervisors, you have been there all along to encourage and support me, even when I was far away, and I am immensely grateful to all of you.

Thank you Don, this adventure started because you offered me the opportunity to follow my passion for volcanoes. I have discovered a new side to volcanology, the experimental side, where I was allowed to blow up and melt rocks. I have lived incredible experiences hiking up volcanoes. And even after all these years, you did not give up on me.

Kai and Betty, you have been my lighthouse, guiding me through this tortuous path of mine. Your knowledge, advice, discussions and moral support have been extremely appreciated.

I am grateful to Prof. Friedrich and Prof. Reichenbacher for including me in the Mentoring group and allowing me to take part to enlightening meetings about women and science.

Basti, Betty, Ulli and Oli, I have learned a whole lot from you in the basement! Alex and Marcel, you were my DSC mentors, thank you so much for taking the time to explain everything in detail! Special thanks to Fabian who reworded my often unclear English and helped me tremendously in figuring out what my “stories” were, and to Teresa and Danilo, for the insightful discussions. Cristina, you really helped me with my talk, that one time in San Francisco.

Thank you Saskia, Yaping, Dirk, Ulli and Michael for spending time at the microprobe measuring my sample, to Oryaëlle for your great help with the viscosity measurements, to Asher, Benoît and Maria for their help with Matlab, to Hilger, for preparing samples always so quickly with so short notice, to Nikita for the XRF measurements, to Erika Griesshaber for the SEM pictures, to Stefan and Soraya, whenever I had a question about petrology, and to Sandra, Margot, Greta, Rosa and Friederike for helping me with the scanner or answering my questions every time I popped in! Kirsten, Rosanne, Ludwig and Stefan, your assistance in the lab was greatly appreciated. Andre and Conrad, without you I could not have written my dissertation!

Warna, Benoît and Asher, miss you guys! Benoît, merci pour ton aide sur le terrain, pour avoir conduit l’auto, et d’avoir essayé de m’apprendre à conduire. On a eu chaud! Warna, you’re next, if you know what I mean! Tini, danke dass du für mich da warst, wo ich schwierige Momente hatte. Simon, vielen Dank für deine Hilfe in Indonesien. Was für eine schreckliche Nacht im Dschungel! Yan, je m’ennuie de ta musique bizarre et de nos placottes à la québécoise. Miguel, it was fun to work with you in the lab. You were always so productive and focused! And, without you realizing it, you gave me the idea that allowed me to write my first paper.

Andi, Maria, Oryaëlle, Teresa and Betty, thank you so much for giving me a place to stay every time I came to Munich!

Mami et Papi, merci de m'avoir autant aidée et de toujours avoir eu une oreille pour moi. Pascale, Jana, Göhkan, Josh, Brian and Lina and all my dear friends, you have done so much. I owe you one, or ten! Michael, ohne deine Unterstützung wäre das Ganze gar nicht möglich gewesen. Du bist mein Stein, mein Halt. Kilian, Mathilda et Béatrice, oui, Maman a enfin terminé son travail.

Let the new chapter begin!